Kimura, G., Silver, E.A., Blum, P., et al., 1997
Proceedings of the Ocean Drilling Program, Initial Reports, Vol. 170

3. SITE 1039[1]

Shipboard Scientific Party[2]

HOLE 1039A

Position: 9°38.397′N, 86°12.006′W

Start hole: 0930 hr, 1 November 1996

End hole: 0330 hr, 2 November 1996

Time on hole: 18.0 hr (0.75 days)

Seafloor depth (drill-pipe measurement from rig floor, mbrf): 4362.5

Water depth (drill-pipe measurement from sea level, m): 4351.7

Distance between rig floor and sea level (m): 10.8

Total depth (drill-pipe measurement from rig floor, mbrf): 4390.5

Penetration (mbsf): 28.0

Coring totals:

Type: APC; No: 3; Cored: 28.0 m; Recovered: 28.91 m (103.25%)

Formation:

Subunit U1A (0–5.55 mbsf): Grayish green diatomaceous ooze with ash and graded sand layers (<0.105 Ma)
Subunit U1B (5.55–28.0 mbsf): Olive green diatomaceous ooze with ash layers (early–late Pleistocene)

HOLE 1039B

Position: 9°38.405′N, 86°12.003′W

Start hole: 0330 hr, 2 November 1996

End hole: 0000 hr, 5 November 1996

Time on hole: 68.5 hr (2.85 days)

Seafloor (drill-pipe measurement from rig floor, mbrf): 4364.5

Water depth (drill-pipe measurement from sea level, m): 4353.5

Distance between rig floor and sea level (m): 11.0

Total depth (drill-pipe measurement from rig floor, mbrf): 4748.8

Penetration (mbsf): 384.3

Coring totals:

Type: APC; No: 11; Cored: 97.0 m; Recovered: 100.30 m (103.4%)
Type: XCB; No: 31; Cored: 287.3 m; Recovered: 282.20 m (98.2%)
Total: No: 42; Cored: 384.3 m; Recovered: 382.46 m (99.5%)

Formation:

Subunit U1A (0–5.55 mbsf): Grayish green diatomaceous ooze with ash and graded sand layers (<0.105 Ma)
Subunit U1B (5.55–84.43 mbsf): Olive green diatomaceous ooze with ash layers (early–late Pleistocene)
Subunit U2A (84.43–132.87 mbsf): Dark olive green silty clay with ash layers (early Pleistocene–late Pliocene)
Subunit U2B (132.87–152.49 mbsf): Dark to light olive green silty clay and calcareous clay with ash layers (early–late Pliocene)
Subunit U3A (152.49–180.38 mbsf): Ivory gray siliceous nannofossil ooze and calcareous clay (late Miocene–early Pliocene)
Subunit U3B (180.38–279.93 mbsf): Ivory to light green siliceous nannofossil ooze with minor ash layers (middle–late Miocene)
Subunit U3C (279.93–377.99 mbsf): Mottled ivory nannofossil ooze with diatomaceous ooze interbeds and matrix-supported breccia of same (middle Miocene)
Unit U4 (377.99–381.00 mbsf): Glassy pyroxene gabbro intrusions with plagioclase glomerocrysts (post-15.6 Ma)

HOLE 1039C

Position: 9°38.383′N, 86°12.002′W

Start hole: 1400 hr, 8 November 1996

End hole: 0115 hr, 11 November 1996

Time on hole: 59.25 hr (2.47 days)

Seafloor (drill-pipe measurement from rig floor, mbrf): 4362.5

Water depth (drill-pipe measurement from sea level, m): 4351.4

Distance between rig floor and sea level (m): 11.1

Total depth (drill-pipe measurement from rig floor, mbrf): 4811.2

Penetration (mbsf): 448.7

Drilled: 0–363.1 mbsf

Coring totals:

Type: RCB; No: 11; Cored: 85.6 m; Recovered: 37.65 m (44.0%)

Formation:

Subunit U3C (363.10–422.13 mbsf): Mottled ivory nannofossil ooze, diatomaceous ooze, and matrix-supported breccia of same (middle Miocene)
Unit U4 (422.11–445.14 mbsf): Glassy pyroxene gabbro intrusions with plagioclase glomerocrysts (post-16.49 Ma)

HOLE 1039D

Position: 9°38.374′N, 86°12.004′W

Start hole: 1200 hr, 18 November 1996

End hole: 0915 hr, 20 November 1996

Time on hole: 45.25 hr (1.89 days)

Seafloor (drill-pipe measurement from rig floor, mbrf): 4362.5

Water depth (drill-pipe measurement from sea floor, m): 4351.3

Distance between rig floor and sea level (m): 11.2

Total depth (drill-pipe measurement from rig floor, mbrf): 4769.5

Penetration (mbsf): 407.0

Logging while drilling

---

[1] Kimura, G., Silver, E.A., Blum, P., et al., 1997. *Proc. ODP, Init. Repts.,* 170: College Station, TX (Ocean Drilling Program).
[2] Shipboard Scientific Party is given in the list preceding the Table of Contents.

Previous Chapter
Table of Contents
Next Chapter

Principal results: We successfully attained our lithostratigraphic objective at Site 1039, obtaining a complete and undeformed stratigraphic reference section of the incoming sediments on the Cocos Plate, to be compared with sites on the Costa Rica Margin (Fig. 1). Three sedimentary units and one intrusive unit were recognized at Site 1039. Unit U1 consists of dark olive green diatomaceous ooze with ash layers. Subunit U1A (<0.105 Ma, 0−5.55 mbsf) is distinguished by abundant graded sand layers interpreted as turbidites and grades downward into Subunit U1B (early−late Pleistocene, 5.55−84.43 mbsf), in which graded sand layers are sparse to absent. Below a sharp contact, Unit U2 is distinguished by a sharp decrease in biogenic sediment. Subunit U2A (late Pliocene−early Pleistocene, 84.43−132.87 mbsf) consists of dark olive green silty clay and grades downward into Subunit U2B (early−late Pliocene, 132.87−152.49 mbsf). Subunit U2B is dark olive green silty clay interbedded with light olive green calcareous clay; ash layers are common throughout Unit U2.

Unit U3 exhibits a dramatic increase in biogenic sedimentation, changing sharply from the nearly barren clays of Unit U2 to calcareous and siliceous oozes. Subunit U3A (late Miocene−early Pliocene, 152.49−180.38 mbsf) is ivory-colored siliceous nannofossil ooze interbedded with calcareous clay; ash layers are sparse. Subunit U3B (middle−late Miocene, 180.38 to ~280 mbsf) consists of ivory to light green and mottled nannofossil ooze with minor ash layers. Subunit U3B grades downward into Subunit U3C (middle Miocene, ~280 to ~378 mbsf in Hole 1039B and ~363−442.13 mbsf in Hole 1039C) and consists of mottled ivory-colored nannofossil ooze, interbedded in the lower part with diatomaceous ooze and matrix-supported breccia of calcareous and siliceous ooze clasts. Preliminary shipboard X-ray fluorescence (XRF) results show that the basal oozes of Subunit U3C are metalliferous, being enriched in nickel, copper, and zinc.

Unit U4 (post-16.49 Ma) was encountered at depths of ~378−381 mbsf in Hole 1039B and ~422−445.15 mbsf in Hole 1039C. It consists of fine- to medium-grained glassy pyroxene gabbro with plagioclase glomerocrysts. Multiple chill zones were recovered within the 22 m of gabbro. The reason for the difference in the depth to the top of the intrusion in Holes 1039B and 1039C is not yet known.

A complete or nearly complete late Pleistocene through early middle Miocene (~16.49 Ma) section cored at Site 1039 is recognized in the combined calcareous nannofossil, diatom, and planktonic foraminifer record. An age-depth model calculated from the combined last and/or first occurrence datums of index microfossils yields average rates of about 46 m/m.y. (0−120 mbsf) for the Pleistocene in the upper part of the section, 6 m/m.y. for the upper Miocene and Pliocene interval (120−200 mbsf), and 47 m/m.y. for the middle Miocene interval (200−448 mbsf). Calcareous nannofossil, diatom, and planktonic foraminifer biostratigraphic zones are easily resolved in the sections of higher interval/age rates. However, in the upper Miocene and Pliocene section, a few of the late Miocene and Pliocene zones apparently cannot be resolved because of low rates and widely spaced (9.6 m) sampling intervals. All microfossils generally exhibit good preservation and sufficient abundances for reliable biostratigraphic analysis. The distribution of diatoms with depth shows clear relationships with the boundaries between Units U1 and U2 and between Units U2 and U3.

Demagnetization of natural remanence in both split cores and discrete samples was successful in defining portions of magnetostratigraphy at Site 1039. The uppermost sequence (0−132 mbsf) has reversals ranging in age from the Blake (0.105 Ma) and Jamaica (0.200 Ma) Events to the termination of Chron C2An.3n (3.33 Ma). The lower sequence of well-defined reversals (302−387 mbsf) spans Chrons C5Ar.1n (12.678 Ma) to C5Cn.2n (16.488 Ma). A large interval of predominantly normal polarity, coinciding with a zone of increased intensity of remanence (120−180 mbsf) occurs within sediment ranging in age from 3.5 to 8.2 Ma. Calculated age-depth rates are 105 m/m.y. for Subunit U1A and 30 m/m.y. for the interval 11−133 mbsf. Within Unit U3, rates decrease from 20 m/m.y. (305−370 mbsf) to 5 m/m.y. (370−380 mbsf) downhole.

The geochemical objectives at Site 1039, similar to those of lithostratigraphy and biostratigraphy, were to obtain a reference section for the distribution of chemical components in the incoming sedimentary section. Here again our objectives were met. Concentrations of methane were low throughout Site 1039. Only in the interval between 25 and 110 mbsf did methane contents exceed the background concentration of 4−8 ppmv. In this sequence, slightly enhanced methane concentrations ranging from 11 to 110 ppmv were detected. The strongly reducing conditions needed for bacterial methane generation evidently have never been achieved in the sediments at Site 1039, and sulfate concentrations remain high throughout the recovered sedimentary sequence.

The carbonate content varies from 0.5 to 87.8 wt%, assuming that all of the carbonates are present as pure calcite. Low $CaCO_3$ concentrations (0.3−4.6 wt%) are found in the upper part of the sediment column (Unit U1). At depths between 113 and 152 mbsf, alternating high- and low-carbonate contents were measured (Unit U2). Below this zone, $CaCO_3$ increases rapidly (up to 87.8 wt%) and remains high throughout Unit U3.

Organic carbon contents range from 0.1 to 1.89 wt%. The highest concentrations occur in the turbidite sequence, suggesting downslope transport of sediments enriched in organic compounds. The pelagic, calcareous sediments are characterized by low total organic carbon (TOC) concentrations ranging from 0.1 to 0.6 wt%. The depth profile for sulfur concentrations parallels that of organic carbon contents. Only the hemipelagic sediments contain significant amounts of sulfur, whereas no sulfur was detected in the sequence dominated by carbonates.

In the organic rich hemipelagic lithologic Unit U1, with 0.6−1.9 wt% TOC, and also in Unit U2, with 0.4−0.6 wt% TOC, bacterially mediated organic matter diagenesis, dissolution of diatoms, and volcanic ash alteration reactions control the chemistry of the pore waters. These reactions affect the physical, magnetic, and chemical properties of the sediments via carbonate, sulfide(s), and probably magnetite precipitation, as well as ion-exchange reactions between ammonium, K, and Na in the clay minerals. In the pelagic calcareous Unit U3, where the TOC content is mostly <0.3 wt% and where dissolved sulfate concentration is close to that of seawater, the chemical signatures of the pore waters are controlled by volcanic ash alteration, diatom dissolution, and, to a lesser extent, carbonate recrystallization. Dissolved silica concentrations are at equilibrium with amorphous silica (opal-A) solubility, and Ca concentrations are twice as high as in seawater. The concentration depth profiles of Ca, Mg, Si, and Cl faithfully reflect the lithologic units, and even the subunits, at this site. In the lowermost variegated, somewhat metalliferous, sedimentary Subunit U3C, diffusion of dissolved metals such as Mn influences sediment color and distribution. Except for a fluid conduit at 95−130 mbsf, the pore-water chemical depth profiles do not support vertical or horizontal fluid advection within the sediment section. In the basal section, however, the pore-water concentration profiles of Cl, K, Ca, Mg, and Si indicate seawater flow in the upper oceanic basement. This hydrologic regime may be responsible for the unusually low heat flow at this site.

XRF geochemistry shows that (1) ashes above 300 mbsf have trace element signatures indicating derivation from arc volcanoes, whereas those below 330 mbsf probably were derived from the Galapagos Hotspot; (2) gabbros are chemically homogeneous and similar to Galapagos lavas rather than East Pacific Rise basalts; and (3) for recycling purposes, the sediment entering the trench off Costa Rica is enriched in K and depleted in Ba and Sr relative to that subducting beneath Guatemala.

Physical properties objectives included obtaining complete distributions of in situ density and porosity, magnetic susceptibility, thermal conductivity, and changes in original lithology, consolidation state, and diagenesis in the sedimentary section. These objectives were met with abundant core and downhole measurements at Site 1039. Lithostratigraphic units are mapped with the color spectrometer, mainly because of the differences in color between the diatomaceous ooze, the nannofossil ooze, and the ash-rich layers. Magnetic susceptibility also mapped the transitions from hemipelagic to pelagic carbonate intervals, as well as intervals with abundant ash. Porosities are high and show a general decrease downsection from about 75% at the seafloor to 65%−70% at the base of Unit U3. A marked drop in porosity and an increase in bulk density and thermal conductivity occur at about 180 mbsf, marking the region where the sediments become dominated by calcareous oozes. *P*-wave velocities are exceptionally low, attaining maximum values of 1650 m/s at 350 mbsf.

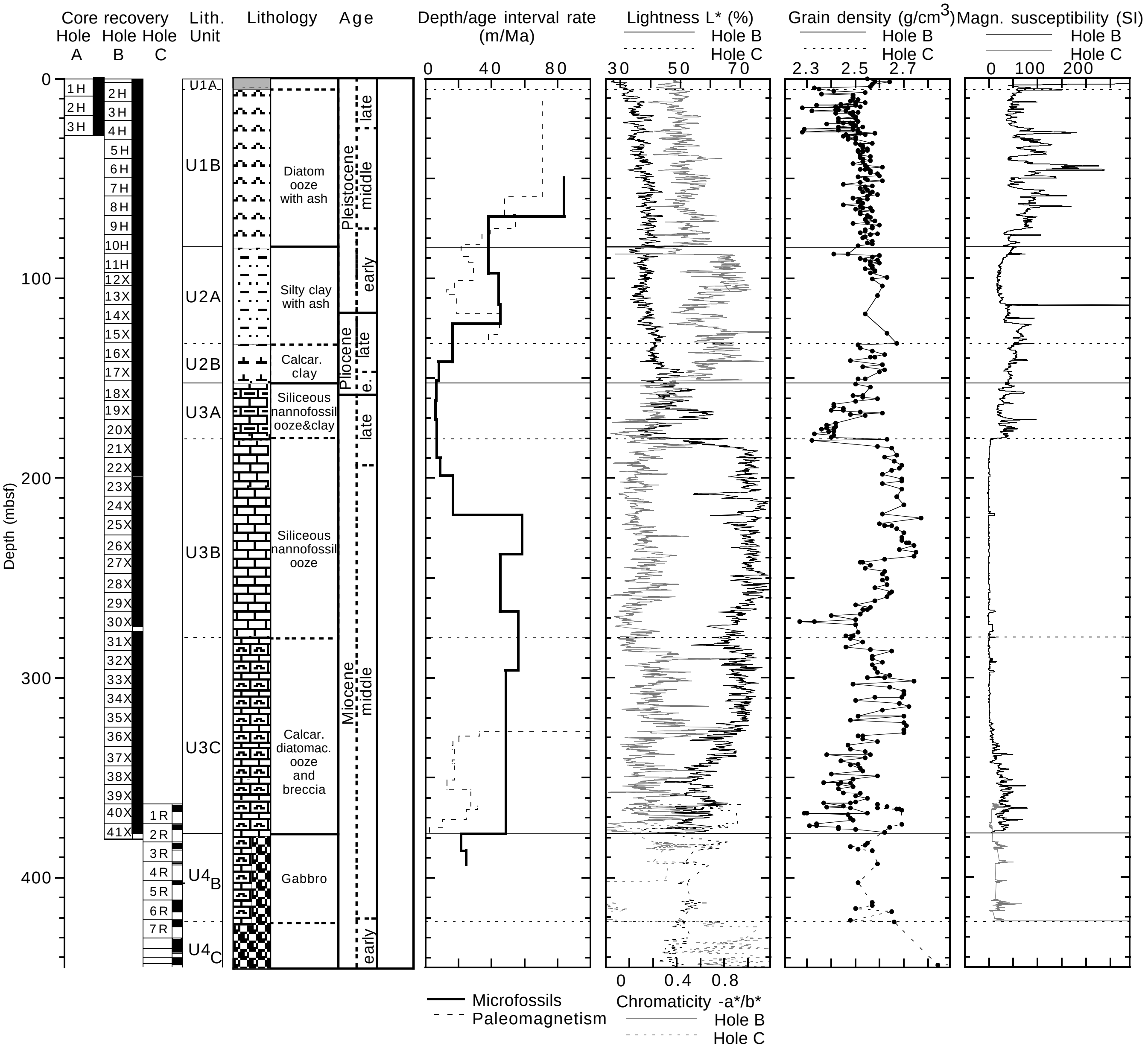

Figure 1. Graphical representation and summary plots of shipboard core and downhole measurements. Explanations of data types and their acquisition are found in the "Explanatory Notes" chapter (this volume). Shipboard descriptions of data are found in relevant sections in this chapter. LWD = logging while drilling, MST = multisensor track, SGR = spectral gamma ray (total counts), and CGR = computed gamma ray (total counts minus contribution of uranium). Gabbro contact was located about 40 m deeper in Hole 1039C than in Hole 1039B; it remains uncertain whether this is caused by a depth datum problem or by a local geological feature (fault; inclined or discontinuous gabbro intrusion). Difference of gabbro depth between Holes 1039B and 1039D (about 15 m) can be attributed to measured deviation of Hole 1039D from vertical.

In situ density and porosity measurements were collected by the compensated density neutron (CDN) tool as part of the logging-while-drilling (LWD) downhole assembly. Downhole measurements correlate closely with core measurements, although downhole densities are a little higher than the core-based values, particularly for carbonate Subunit U3B below 200 mbsf. Major features on the downhole profiles occur at slightly greater depths (a few meters) than on the core-based profiles. This effect may be caused by a small angle hole deviation of Hole 1039D relative to Hole 1039B. Below 395 mbsf, exceptionally high density values (up to 2.8 g/cm^3) are consistent with the gabbro intrusions in this interval.

Porosities calculated directly from the neutron log fluctuate widely throughout the logged interval. The filtered neutron porosity profile correlates well with porosity measurements on core specimens. The large decrease in porosity at 185–195 mbsf corresponds with a marked increase in downhole bulk density at 188 mbsf. Cyclical changes in porosity occur over the interval 195–285 mbsf, with rapid downward decreases between more gradual downward increases.

In situ resistivity measurements were collected using the compensated dual resistivity (CDR) tool of the LWD assembly in Hole 1039D. The deep and shallow resistivity logs show very similar trends and amplitudes, indicating excellent hole conditions. Computed formation factors, based on a constant pore-water salinity of 35, range from 1.7 to 3 and show the same trends as the resistivity variations. Resistivity trends largely mimic the bulk density log. They vary between 0.6 and 0.8 Ωm over the sedimen-

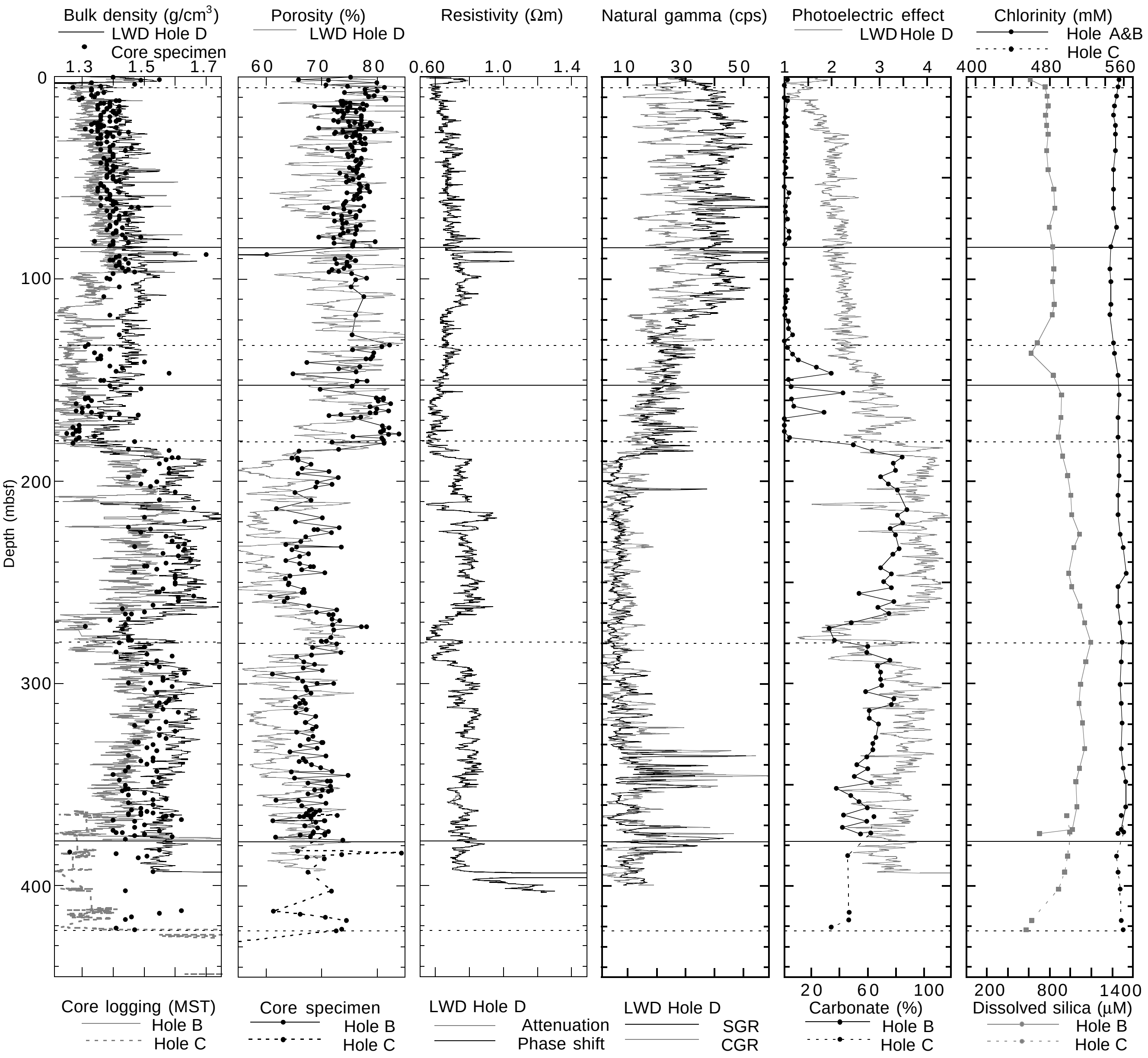

Figure 1 (continued).

tary interval. The gabbro intrusion of the interval 395–398 mbsf shows exceptionally high resistivities (up to 20 Ωm).

In situ natural gamma-ray measurements were collected by CDR, and the photoelectric effect (PEF) was measured by CDN in Hole 1039D. The profile of the total spectral gamma ray shows a similar trend to the magnetic susceptibility profile from cores throughout the section. Uranium yields distinctively decrease at 127 mbsf. Most of the strong peaks of the gamma-ray profile can be correlated to ash layers. The PEF profile shows a similar trend to that of carbonate and colorimetry. In the interval 138–188 mbsf, PEF increases from 2 to 4, which coincides with the increasing carbonate content in lithologic Subunit U3A. In the intervals 210–227 and 267–292 mbsf, PEF decreases to values as low as 1.5, which is best explained by an increased abundance of biogenic opal.

To better understand the anomalously low heat flows reported from this region, one objective of drilling was to obtain temperature measurements throughout the sedimentary section. Our efforts here were successful. Temperature measurements at Site 1039, using the APC temperature tool and the Davis-Villinger Temperature Probe (DVTP) tools, reveal a geothermal gradient of 9.8 K/km. Measured thermal conductivity of 0.85 W/(m·K) gives a heat flow of 8.4 mW/m^2, very close to that measured by surface heat flow. This anomalously low heat flow suggests that processes act to refrigerate the uppermost igneous crust in this location.

In summary, all lithostratigraphic, biostratigraphic, geochemical, and physical properties objectives were reached in the sedimentary section of Site 1039. We were not completely successful with the basement section, because the basal units cored are gabbroic intrusive rocks, and therefore they do not represent true basement. A seismic-reflection model of the intrusions suggests a thickness of about 70 m. We concluded that finding extrusive basalt, although useful, did not justify the potential time expenditure at this site. Lack of a 50-m hole into true basement limited our ability to understand the recycling of the deeper crustal rocks. A further goal, to obtain an unequivocal maximum age of the downgoing crust, was not achieved for the same reasons. Future drilling here should plan to obtain 100–200 m of oceanic basement for modeling geochemical recycling.

BACKGROUND AND SCIENTIFIC OBJECTIVES

The objectives of Leg 170 were to determine the mass and fluid-flow paths through the Costa Rica subduction complex. Fundamental to these objectives is an understanding of the nature of the incoming sediment and crust on the Cocos Plate, before subduction. Site 1039 was chosen from a set of closely spaced seismic-reflection profiles based on the following characteristics. First, it is located in the trench seaward of the frontal thrust (Fig. 2). Second, it is located away from normal faults that cut the lower plate, and no such fault occurs between this site and the frontal thrust (Fig. 5, "Introduction" chapter, this volume). Third, this site contains a clear seismic record of the plate stratigraphy (Fig. 3). Fourth, Site 1039 is located on the same seismic line as Site 1040, where the toe of the upper plate was drilled (Fig. 6, "Introduction" chapter, this volume). In addition, Site 1039 is far enough away from the frontal thrust that it is expected to be reasonably far from the influence of downslope debris flows that might emanate from an active convergent margin slope.

Two dominant seismic stratigraphic units have been recognized in the seismic data at this site (Fig. 3). The upper unit has lower reflectivity and lower continuity of individual reflectors. It has been inferred to be hemipelagic deposits. This unit is mapped from the seafloor to a depth of about 180 mbsf, using the velocity data of K. McIntosh (unpubl. data). There is a hint of slightly higher reflectivity in the uppermost few tens of meters of this section, but it is difficult to distinguish clearly because of the interference of the strong seafloor reflection. The second unit has high reflectivity and good continuity of individual reflectors and makes up the lower part of the sedimentary section, below about 180 mbsf. The lowermost few tens of meters of this section have a lower reflectivity and reflection continuity than does the bulk of the unit, possibly indicating a change in composition or material properties near the base of the sediments.

The sedimentary section rests on a high-amplitude basement, which shows as one or two major reflections beneath the trench region. Two high-amplitude reflections occur beneath the sedimentary section at the location of Site 1039. The upper basement reflection ends ~1 km northeast of the site, consistent with the geometry of a sill. The surface of the upper basement reflection at Site 1039 shows apparent relief of about 10 m over a distance of a few hundred meters. A major normal fault occurs 1 km southwest of Site 1039, showing an apparent vertical displacement of about 150 m. The zone affected by normal faulting is about 400 m wide.

Heat-flow measurements (Fig. 7, "Introduction" chapter, this volume) made in the trench near Site 1039 showed values ranging from 8 to 15 mW/m^2 (Langseth and Silver, 1996). Fifteen measurements were made in the trench region, with a mean value of ~12 mW/m^2. One of the cruise objectives is to try to shed light on the reasons for this low heat flow. The age of the incoming lithosphere is somewhat uncertain. Earlier reports placed the age at 25–27 Ma (Hey, 1977; Lonsdale and Klitgord, 1978), although recent studies imply a young-

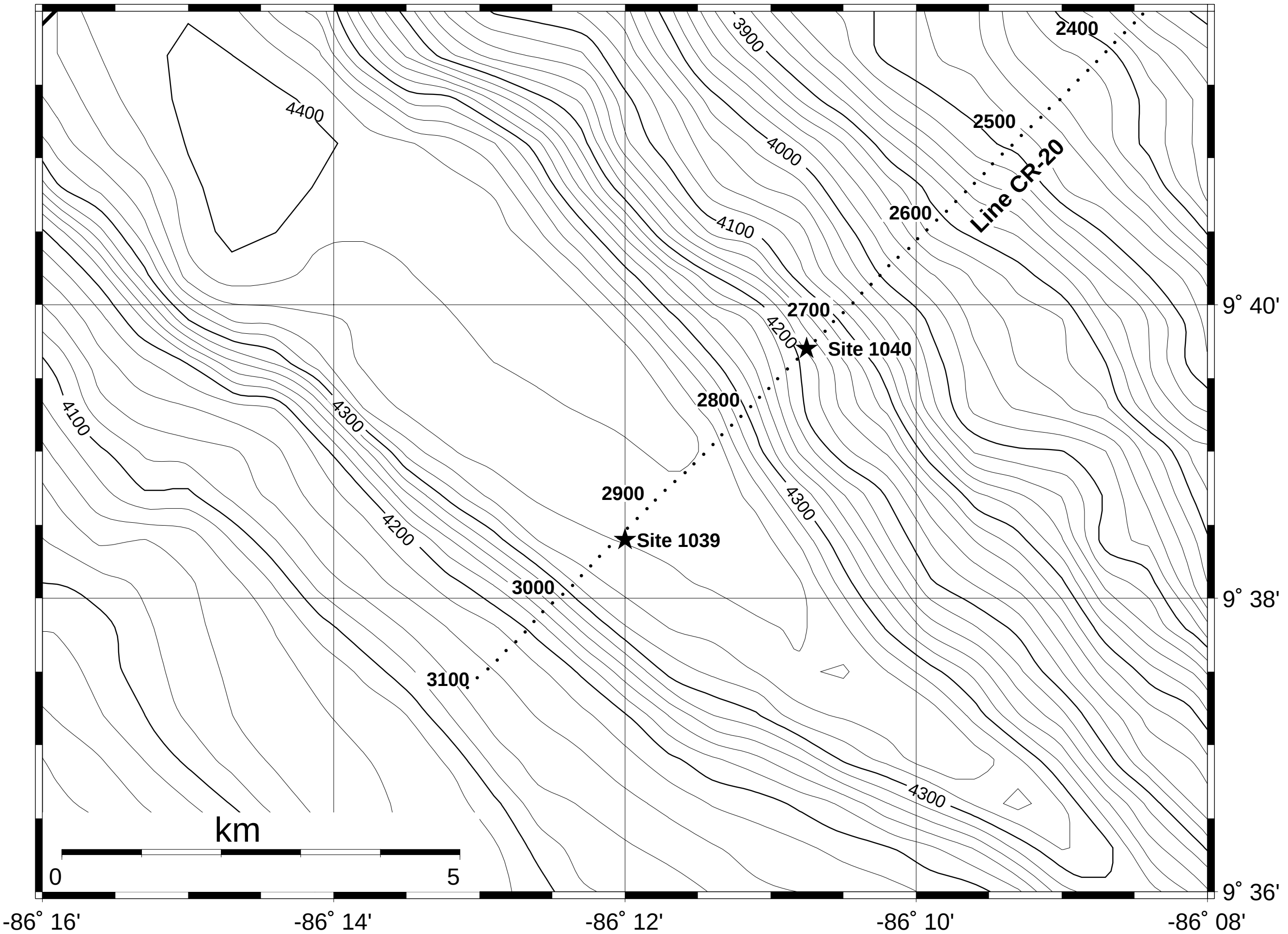

Figure 2. Bathymetric map of the Middle America Trench off the Nicoya Peninsula, Costa Rica, showing the location of seismic Line CR-20 and ODP Sites 1039 and 1040 (from hydrosweep bathymetry, provided by R. von Huene, unpubl. data).

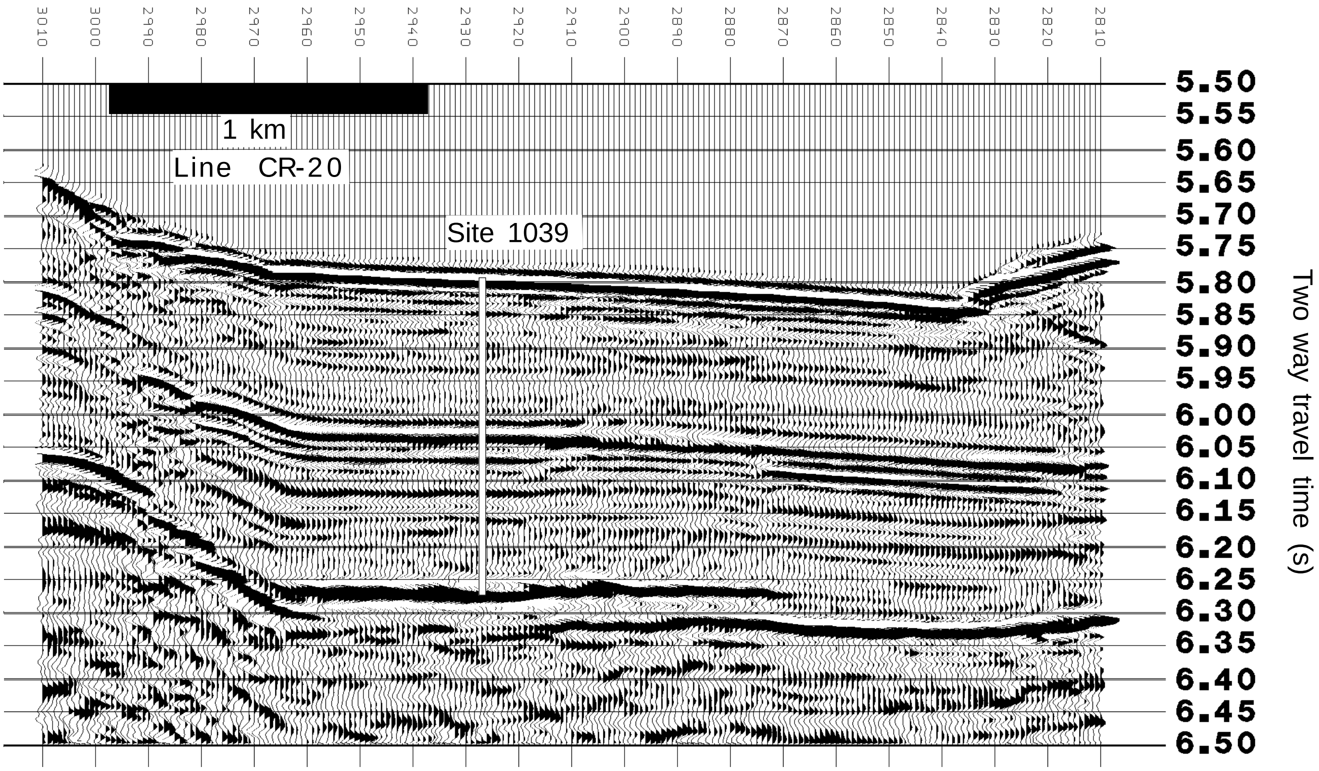

Figure 3. Detailed seismic image of the Middle America Trench from seismic Line CR-20, showing the location of Site 1039.

er age (Wilson, 1996). The oldest ages recovered at Site 844 from Ocean Drilling Program (ODP) Leg 138 (410 km from Site 1039) are 15–17 Ma. This site is about 400 km from the trench axis, so it would imply an older age at the trench. Lithosphere of Oligocene–Miocene age is expected to have relatively high heat flow—the order of 80–100 mW/m^2. The extremely low heat flow observed on crust of approximately this age suggests drastic cooling in the near surface.

Another objective at Site 1039 was to apply LWD technology. This technology was expected to provide both high-quality and high-resolution downhole logs of density, porosity, and resistivity, to compare with the core data and the results of similar logging at Site 1040. The specific operational objectives at Site 1039 were to obtain a continuous coring record of the incoming sediment on the Cocos Plate, before encountering the subduction zone of the Middle America Trench, and to obtain a downhole record of the chemistry of the pore waters, the distribution of physical properties, in situ density and porosity using LWD technology, the distribution of ages and mass accumulation rates, the temperature gradient with depth and corresponding heat flow, and the nature and age of basement beneath the sedimentary section.

OPERATIONS

Transit to Site 1039

The ship departed San Diego on 22 October 1996 at 1900 hr and set a southerly course to Sites 1039 and 1040. At 1200 hr on 26 October, medical evacuation of a roustabout took place by motor launch near Mazatlan, Mexico. An hour later the ship continued its approach to the first site. Work begun or completed during the transit included general rig maintenance; installation of an air duct extension; standpipe pressure testing for Leg 174 hammer drill tests; installation of a new top drive electrical umbilical; sand-blasting, painting, and coating of the helicopter pad; and changing the identification name on all ship's equipment in preparation for changing the official name of registry in Panama from *SEDCO/BP 471* to *JOIDES Resolution.*

The ship arrived in the survey area at 0630 hr, 1 November 1996. The course was changed to allow a survey across Sites 1039 and 1040. Both 200- and 80-in^3 water guns were deployed; however, a hose failed on the 80-in^3 gun 20 min into the survey, and the 200-in^3 gun was used for the remainder of the survey. Once the survey was completed, the ship returned to Site 1039 and prepared for drilling operations. A positioning beacon was dropped at 0930 hr, 1 November, initiating operations at Site 1039.

Hole 1039A

Because of the loss of the drill string on Site 1038 during ODP Leg 169, refurbished 5-in drill pipe and new drill collars had to be picked up for this site. In addition, a new seal bore drill collar for advanced hydraulic piston coring (APC) had to be picked up.

Hole 1039A was spudded at 0015 hr, 2 November 1996. The mudline core recovered 9.0 m (Tables 1, 2), placing the drill pipe measured seafloor at 4362.5 m, or 5.9 m above the corrected precision depth recorder (PDR) mudline of 4368.4 m. The plan was to only recover three piston cores from this hole. Coring was terminated after Core 3H at a total depth of 28.0 mbsf. The drill string was pulled above the mudline, and the vessel was immediately offset 10 m to the north in preparation for spudding Hole 1039B.

Hole 1039B

Hole 1039B was spudded at 0430 hr, 2 November 1996. The first core recovered 2.02 m and established a seafloor depth of 4364.5 m, or 3.9 m above the corrected PDR mudline for this site. APC coring continued with electronic core orientation (Tensor), beginning on

Table 1. Coring summary for Site 1039.

Core	Date (Nov. 1996)	Time (UTC)	Depth (mbsf)	Length cored (m)	Length recovered (m)	Recovery (%)
170-1039A-						
1H	02	0645	0.0-9.0	9.0	9.00	100.0
2H	02	0810	9.0-18.5	9.5	9.94	104.0
3H	02	0920	18.5-28.0	9.5	9.97	105.0
Coring totals:				28.0	28.91	103.2
170-1039B-						
1H	02	1055	0.0-2.0	2.0	2.02	101.0
2H	02	1410	2.0-11.5	9.5	9.87	104.0
3H	02	1520	11.5-21.0	9.5	8.96	94.3
4H	02	1650	21.0-30.5	9.5	10.05	105.8
5H	02	1930	30.5-40.0	9.5	9.88	104.0
6H	02	2035	40.0-49.5	9.5	9.80	103.0
7H	02	2200	49.5-59.0	9.5	10.00	105.2
8H	03	0115	59.0-68.5	9.5	9.91	104.0
9H	03	0220	68.5-78.0	9.5	9.90	104.0
10H	03	0340	78.0-87.5	9.5	10.01	105.3
11H	03	0445	87.5-97.0	9.5	9.90	104.0
12X	03	0001	97.0-103.5	6.5	9.75	150.0
13X	03	0715	103.5-113.1	9.6	9.63	100.0
14X	03	0825	113.1-122.7	9.6	9.63	100.0
15X	03	0945	122.7-132.2	9.5	9.76	103.0
16X	03	1235	132.2-141.8	9.6	9.59	99.9
17X	03	1355	141.8-151.4	9.6	9.41	98.0
18X	03	1510	151.4-161.1	9.7	9.59	98.8
19X	03	1630	161.1-170.6	9.5	9.65	101.0
20X	03	1745	170.6-180.2	9.6	9.78	102.0
21X	03	2010	180.2-189.8	9.6	9.69	101.0
22X	03	2115	189.8-199.5	9.7	8.87	91.4
23X	03	2215	199.5-209.1	9.6	9.29	96.8
24X	03	2315	209.1-218.7	9.6	9.35	97.4
25X	04	0025	218.7-228.4	9.7	9.61	99.1
26X	04	0240	228.4-238.0	9.6	9.63	100.0
27X	04	0335	238.0-247.7	9.7	9.59	98.8
28X	04	0435	247.7-257.4	9.7	9.60	98.9
29X	04	0545	257.4-267.1	9.7	9.47	97.6
30X	04	0650	267.1-276.7	9.6	7.08	73.7
31X	04	1020	276.7-286.4	9.7	9.59	98.8
32X	04	1130	286.4-296.0	9.6	9.76	101.0
33X	04	1400	296.0-305.6	9.6	9.69	101.0
34X	04	1510	305.6-315.2	9.6	9.78	102.0
35X	04	1620	315.2-324.8	9.6	9.68	101.0
36X	04	1730	324.8-334.4	9.6	9.84	102.0
37X	04	1840	334.4-344.0	9.6	9.85	102.0
38X	04	2000	344.0-353.6	9.6	9.87	103.0
39X	04	2110	353.6-363.2	9.6	9.74	101.0
40X	04	2320	363.2-372.8	9.6	9.71	101.0
41X	05	0100	372.8-380.8	8.0	5.38	67.2
42X	05	0335	380.8-384.3	3.5	0.30	8.6
Coring totals:				384.3	382.46	99.5
170-1039C-						
1R	09	2045	363.1-372.7	9.6	3.84	40.0
2R	09	2215	372.7-382.3	9.6	3.17	33.0
3R	09	2340	382.3-391.9	9.6	4.11	42.8
4R	10	0115	391.9-401.5	9.6	1.75	18.2
5R	10	0240	401.5-411.2	9.7	1.58	16.3
6R	10	0405	411.2-420.8	9.6	6.11	63.6
7R	10	0710	420.8-430.3	9.5	3.89	40.9
8R	10	1415	430.3-435.7	5.4	5.43	100.0
9R	10	1900	435.7-439.9	4.2	2.64	62.8
10R	10	2335	439.9-443.0	3.1	3.14	101.0
11R	11	0405	443.0-448.7	5.7	1.99	34.9
Coring totals:				85.6	37.65	44.0

Note: UTC = Universal Time Coordinated.

Core 5H at a depth of 40.0 mbsf. Oriented APC coring was terminated with Core 11H at a depth of 97.0 mbsf after Cores 10H and 11H failed to fully stroke. A maximum overpull of 50 kilo-pounds (kips) was experienced on Core 8H.

Coring continued using the extended core barrel (XCB) system to ~378 mbsf, where a drilling break was noted. The formation turned hard and drilling torque increased. Core 41X was pulled early after an 8.0-m advance. One meter of fill was detected on bottom before cutting Core 42X. The hole was advanced an additional 3.5 m to a total depth of 384.3 mbsf. Core 42X recovered gabbroic rock fragments.

Immediately after recovering the mudline core, a water-sampling temperature probe (WSTP) was deployed with an APC temperature tool measurement sub attached. The bit was positioned 10 m above the seafloor for taking a bottom-water sample and temperature reading. During recovery, the tool hung up at ~45 m above the seafloor. After jarring, the tool came free. It is assumed that an errant APC shear pin stub wedged the barrel. The bottom-water sample had a salinity of 31.5, indicating surface-water contamination caused by the circulation used to pump the tools to bottom. Future bottom-water deployments were done without circulation by running the wireline winch at slower speeds.

After taking three more piston cores, another WSTP fluid sample was taken after Core 4H at a depth of 30.5 mbsf. Apparently the wrong sub was installed for this run, because the tool only sampled drill-pipe circulating fluid. Another WSTP fluid sample was attempted after Core 7H at a depth of 59.0 mbsf. This time the tool hung up at ~1800 m below the ship during deployment. After 20 min of working the wireline jars, the overshot shear pin sheared and the barrel dropped to bottom. An attempt to get data was made, but the temperature data indicated that the tool never penetrated the formation. It appears that the core line operator ran the tool in too fast, causing the barrel to float. When the line went slack on the XCB latch, it allowed the latch dogs to come out enough to wedge the barrel. The WSTP system was not deployed for the remainder of the hole.

A total of 10 temperature measurements were taken, four with the APC temperature tool during APC coring and six with the DVTP during XCB coring. One APC temperature tool measurement was bad because of battery failure. One DVTP measurement was bad. Results are presented in the “Physical Properties” section (this chapter).

There were no significant hydrocarbon shows identified while drilling this hole. Methane ranged from 3 to 36 ppmv, and there was no ethane or propane identified with the exception of Core 10X at 84 mbsf, where 110 ppmv methane and 6 ppmv ethane were recorded.

No mud sweeps were required during coring. Once coring had ceased, the hole was filled with 10.5 lb/gal mud, and the drill string was tripped out of the hole. While pulling pipe, an overpull of 50 kips was taken at a depth of 4600 m. The drill string cleared the seafloor at 2400 hr, ending Hole 1039B.

Operations at Site 1040

Before drilling deeper at Site 1039 using the rotary core barrel (RCB) system, operations began at Site 1040 with the APC and XCB to save a pipe trip. See the “Operations” section, “Site 1040” chapter (this volume), for report.

Hole 1039C

The ship was located 30 m south of Hole 1039A for spudding Hole 1039C. An RCB bottom-hole assembly (BHA) was made up, and the RCB core barrels space-out was checked. The BHA was tripped in the hole, and the top drive was picked up, placing the bit at a depth of 4313.0 m. The rig floor corrected PDR water-depth reading for this site was 4366.4 m. This was very close to the drill-pipe measured depth of 4362.5 for Hole 1039B. Because of the proximity of the two holes, the water depth of Hole 1039A was used for Hole 1039C.

After collecting a bottom-water fluid sample, a center bit was deployed, the pipe was tripped the remaining distance to bottom, and Hole 1039C was spudded. Drilling ahead with a center bit continued to a depth of 363.1 mbsf. A sepiolite mud sweep was pumped at 344.0 mbsf to flush any remnant cuttings from the hole before RCB coring began with Core 1R. Coring continued through Core 7R, where a gabbro intrusion was contacted at a drillers’ depth of 4789.7 m (427.2 mbsf). This is about 46 m deeper than where gabbro was contacted in Hole 1039B. Coring continued through apparent sills and occasional

Table 2. Coring section summary for Site 1039.

Leg	Site	Hole	Core	Type	Top (mbsf)	Bottom (mbsf)	Advancement	Section number	Liner length (m)	Curated length (m)	Map interval top (mbsf)	Map interval bottom (mbsf)	Map type
170	1039	A	1	H	0.0	9.0	9.0	1	1.50	1.50	0.00	1.50	STD
170	1039	A	1	H	0.0	9.0	9.0	2	1.50	1.50	1.50	3.00	STD
170	1039	A	1	H	0.0	9.0	9.0	3	1.50	1.50	3.00	4.50	STD
170	1039	A	1	H	0.0	9.0	9.0	4	1.50	1.50	4.50	6.00	STD
170	1039	A	1	H	0.0	9.0	9.0	5	1.50	1.50	6.00	7.50	STD
170	1039	A	1	H	0.0	9.0	9.0	6	1.25	1.25	7.50	8.75	STD
170	1039	A	1	H	0.0	9.0	9.0	7	0.25	0.25	8.75	9.00	STD
170	1039	A	2	H	9.0	18.5	9.5	1	1.50	1.50	9.00	10.50	STD
170	1039	A	2	H	9.0	18.5	9.5	2	1.50	1.50	10.50	12.00	STD
170	1039	A	2	H	9.0	18.5	9.5	3	1.50	1.50	12.00	13.50	STD

Note: STD = standard.

This is a sample of the table that appears on the volume CD-ROM.

thin (1.0–3.0 m thick) softer material with dramatically different drilling rates, presumed to be sediments. However, no sediments were recovered from these intervals. Coring continued through Core 11R to a total depth of 4811.2 m (448.7 mbsf). Coring was terminated because of a slow rate of penetration (ROP; 0.5–1.0 m/hr) through the massive gabbroic units, and an inability to recover the softer interlayered sediments.

No drilling mud was circulated during the coring operation. However, the hole was displaced with 10.5-lb/gal mud before pulling out. Overpulls of 20–30 kips were required while pulling out of the hole from 340.9 to 167.8 mbsf.

No temperature measurements were made in this hole and no WSTP fluid samples were taken except for a bottom-water sample collected before spudding the hole at ~50 m above the seabed. No significant hydrocarbon shows were identified while drilling this hole. Methane ranged from 3 to 4 ppmv, and neither ethane nor propane was identified.

Operations at Site 1040

After completion of Hole 1039C, the ship returned to Site 1040 to drill the RCB Hole 1040C (see "Operations" section, "Site 1040" chapter, this volume). During the transit back on Site 1039, the drill string was recovered and preparations for LWD were made.

Hole 1039D

The ship was already positioned on the drilling location for Hole 1039D before the drill string and BHA were fully recovered aboard ship. Hole 1039D was to be spudded 50 m south of Hole 1039A.

Before making up the LWD tools, the drill line was slipped and cut. It required 2.5 hr to make up the LWD tools (CDN and CDR), load the nuclear sources, and make up the cross-over sub.

Drilling proceeded slowly at first until the BHA was fully buried. Overall, the ROP averaged 23.3 m/hr, which was very close to the maximum desired rate of 25 m/hr. A 3.5-m-thick hard layer was contacted at a depth of 395.0 mbsf. A reduced ROP of ~2.5 m/hr continued until breaking out at a depth of 398.5 mbsf. The original drilling rate resumed until severe torquing began ~5 m later. During the course of drilling, the bit became stuck on bottom, requiring 40 kips overpull to free. The driller immediately pumped a 30-bbl sepiolite mud sweep and pulled above the hard layer. Reaming back through this area proceeded without incident until the bit was again on bottom, where torque increased again dramatically and the bit became stuck again. The bit was freed with 40 kips overpull, and the decision was made to terminate the LWD hole at a depth of 4769.5 m, or 407.0 mbsf. The stabilizer on the LWD tools was suspected of causing the problem as it entered the hard layer. It was felt that continued reaming of the area, coupled with the use of generous mud sweeps, would probably have corrected the problem. However, the co-chiefs decided that the main objectives were achieved, and the decision was made to pull out of the hole. The hole was subsequently filled with 10.5-lb/gal mud, and the drill string was pulled clear of the seafloor. The trip continued to the surface, where the nuclear sources were removed, and the LWD collars were laid out. The positioning beacon for this site was released/recovered, and the bit cleared the rotary table at 0915 hr, ending Hole 1039D and operations at Site 1039.

LITHOSTRATIGRAPHY AND STRUCTURES

Introduction

Site 1039 was drilled to establish a reference section to compare with the subducted section below the décollement at Sites 1040 and 1043. It was originally planned to penetrate to 500 mbsf, including about 50 m into oceanic basement. However, intrusive gabbro encountered around 400 mbsf caused very slow drilling, and Site 1039 was abandoned after recovering 22 m of pyroxene gabbro.

Three sedimentary units and one intrusive unit were recognized at Site 1039 (Fig. 1; Table 3). Unit U1 (Underthrust 1) consists of olive green diatomaceous ooze with numerous ash layers. Subunit U1A (Holocene, 0–5.5 mbsf) is distinguished by abundant graded sand layers interpreted as turbidites, and grades downward into Subunit U1B (early–late Pleistocene, 5.5–84 mbsf), in which graded sand layers are rare.

Unit U2 marks a sharp decrease in biogenic sediment and a corresponding increase in clay downsection. Subunit U2A (Pliocene–Pleistocene, 84–133 mbsf) consists of dark olive green silty clay, and grades downward into Subunit U2B (Pliocene, 133–152 mbsf). Subunit U2B consists of dark olive green silty clay interbedded with light olive green calcareous clay. Ash layers are common throughout Unit U2.

Unit U3 records a dramatic increase in biogenic components downsection, changing sharply from the nearly barren clays of Unit U2 to calcareous and siliceous oozes. Ash layers are rare throughout most of Unit U3. Subunit U3A (upper Miocene–lower Pliocene, 152–180 mbsf) consists of ivory-colored siliceous nannofossil ooze interbedded with calcareous clay. Subunit U3B (middle–late Miocene, 180–280 mbsf) consists of ivory to light green and mottled siliceous nannofossil ooze with few ash layers. Subunit U3B grades downward into Subunit U3C (middle Miocene, 280 to ~400 mbsf), a mottled ivory-colored calcareous ooze interbedded with matrix-supported breccia of calcareous ooze clasts.

Unit U4 was encountered at depths of 378 mbsf in Hole 1039B and 423 mbsf in Hole 1039C. The reason for this difference in depths is unknown. The unit consists of fine- to medium-grained glassy pyroxene gabbro with plagioclase glomerocrysts. Multiple chill zones within the 22 m of gabbro recovered, plus two changes in the ROP that suggests softer material that was not recovered, support the interpretation that multiple thin intrusions are present.

Table 3. Site 1039 lithostratigraphic units.

Unit	Subunit	Intervals	Thickness (m)	Depth (mbsf)	Age
U1: diatomaceous ooze (0-84.43 mbsf)	U1A: diatomaceous ooze with sand and ash layers	1039A-1H-1, 0 cm, to 1H-3, 55 cm 1039B-1H-1, 0 cm, to 2H-1, 68 cm	5.55	0-5.55	<0.105 Ma
	U1B: diatomaceous ooze with ash layers	1039A-1H-3, 55 cm, to 3H-CC, 21 cm 1039B-2H-1, 68 cm, to 10H-5, 40 cm	78.75	5.55-84.43	early to late Pleistocene
U2: silty clay (84.43-152.49 mbsf)	U2A: silty clay with ash layers	1039B-10H-5, 40 cm, to 16X-1, 75 cm	48.44	84.43-132.87	late Pliocene to early Pleistocene
	U2B: silty clay with calcareous clay, ash layers	1039B-16X-1, 75 cm, to 18X-1, 109 cm	19.62	132.87-152.49	early to late Pliocene
U3: calcareous ooze (152.49-422.13 mbsf)	U3A: siliceous nannofossil ooze and calcareous clay	1039B-18X-1, 109 cm, to 20X-CC, 31 cm	27.89	152.49-180.38	late Miocene to early Pliocene
	U3B: nannofossil ooze	1039B-20X-CC, 31 cm, to 31X-3, 23 cm	99.55	180.38-279.93	middle to late Miocene
	U3C: nannofossil ooze with diatomaceous ooze and breccia	1039B-31X-3, 23 cm, to 41X-CC, 35 cm 1039C-1R-1, 0 cm, to 7R-2, 31 cm	98.06 >59.03	279.93-377.99 363.10-422.13	middle Miocene early to middle Miocene
U4: pyroxene gabbro (377.99-445.14 mbsf)		1039B-41X-CC, 35 cm, to 42X-1, 30 cm 1039C-7R-2, 31 cm, to 11R-2, 92 cm	>3.01 >23.03	377.99-381.0 422.11-445.14	Post-15.6 Ma Post-16.49 Ma

Description of Lithostratigraphic Units

Unit U1: Diatomaceous Ooze

Intervals: 170-1039A-1H-1, 0 cm, to 3H-CC, 21 cm; 170-1039B-1H-1, 0 cm, to 10H-4, 40 cm
Thickness: 84.43 m
Depth: 0–84.43 mbsf
Age: Pleistocene

Subunit U1A: Diatomaceous Ooze with Sand-silt Layers

Intervals: 170-1039A-1H-1, 0 cm, to 1H-3, 55 cm; 170-1039B-1H-1, 0 cm, to 2H-1, 68 cm
Thickness: 5.55 m
Depth: 0–5.55 mbsf
Age: <0.105 Ma

Subunit U1B: Diatomaceous Ooze

Intervals: 170-1039A-1H-3, 55 cm, to 3H-CC, 21 cm; 170-1039B-2H-1, 68 cm, to 10H-5, 40 cm
Thickness: 78.88 m
Depth: 5.55–84.43 mbsf
Age: early–late Pleistocene

Unit U1 consists mainly of olive green diatomaceous ooze with common to trace amounts of sponge spicules, radiolarians, and silicoflagellates (Table 4). Carbonate content is <5% throughout Unit U1. Subunit U1A is distinguished from Subunit U1B by its numerous graded sand and silt layers with sharp, scoured basal contacts. The top 22 cm in Hole 1039A and the top 17 cm in Hole 1039B consist of poorly sorted, brownish gray, medium- to coarse-grained sand in a matrix of clayey diatomaceous ooze (Fig. 4).

Below the uppermost sand, Subunit U1A consists of diatomaceous ooze with thin (0.5–1 cm) layers of sand and silt spaced 5–15 cm apart in the upper part of the unit. These thinner layers grade from fine, medium, or coarse sand at the base upward into fine sand or silt mixed with diatomaceous ooze at their tops. Sand- and silt-sized grains include quartz, feldspar, amphibole, opaque minerals, glauconite, fragments of phosphate nodules, shell fragments, foraminifers, sponge spicules, and tephra (Table 4). The coarse layers decrease in number and thickness downward throughout Subunit U1A. A layer of light gray lithic-vitric ash mixed with ooze occurs at the base of a sand layer, 0.17 mbsf (Hole 1039B). Some of the sand-silt layers in Subunit U1A are so rich in volcanic debris that they appear to be reworked ashes.

Subunit U1B is dominated by olive green diatomaceous ooze with minor thin silt or fine sand layers in the upper part. In addition to abundant diatoms, the ooze includes common to trace amounts of radiolarians, sponge spicules, and silicoflagellates. Foraminifers and radiolarians are locally abundant. Some intervals are extensively bioturbated and burrowed, with *Zoophycos* being the most recognizable trace fossil (Fig. 5). Disseminated framboidal pyrite is common throughout Subunit U1B and is locally abundant, with some framboid-filled microfossil tests. Pyrite concretions are common throughout Subunit U1B. The rare silt-sand layers in Subunit U1B typically consist of fine- to medium-grained sand, silty sand, or fine- to very fine-grained sandy silt. Clast composition within Subunit U1B is similar to that observed in Subunit U1A sands.

Volcanic glass, pumice, and scoria occur as disseminated particles throughout Unit U1 and as distinct layers of ash or ash mixed with terrigenous debris. Many of these ashy layers grade upward from fine sand-sized grains above a sharp base into silt-sized grains and then into diatomaceous ooze. Many ash layers are burrowed. Ash also occurs as isolated pods or lenses, in some cases filling burrows. Most ash in Unit U1 is light gray vitric ash or medium to dark gray lithic-vitric ash in which the rock fragments are tephra (Table 4). Tephra fragments typically display tiny euhedral plagioclase crystals and, rarely, olivine or quartz. They range from light grayish brown pumice to dark scoriaceous obsidian. Figure 6 is a typical example of the light-colored ashes recovered from the upper part of Site 1039, with a nearly pure vitric ash at its base and grading upward into vitric ash mixed with diatomaceous ooze. A distinctive fining upward layer, 4 cm thick, of black crystal-vitric ash occurs at 7.26–7.3 mbsf in Hole 1039A and at 5.63–5.67 mbsf in Hole 1039B. Below 60 mbsf in Subunit U1B, sparse layers of pinkish gray, yellowish gray, or brownish ash are interspersed with the more common light to dark gray ash layers.

Unit U2: Silty Clay

Interval: 170-1039B-10H-5, 40 cm, to 18X-1, 109 cm
Thickness: 68.06 m
Depth: 84.43–152.49 mbsf
Age: early Pliocene–early Pleistocene

Subunit U2A: Silty Clay

Interval: 170-1039B-10H-5, 40 cm, to 16X-1, 75 cm
Thickness: 48.44 m
Depth: 84.43–132.87 mbsf
Age: late Pliocene–early Pleistocene

Subunit U2B: Silty Clay and Calcareous Clay

Interval: 170-1039B-16X-1, 75 cm, to 18X-1, 109 cm
Thickness: 19.62
Depth: 132.87–152.49 mbsf
Age: early–late Pliocene

Unit U2 is recognized by a sharp decrease in the biogenic component corresponding to an increasing proportion of terrigenous material, especially clay. Although the change occurs across an interval of poor recovery and suck-in at the base of Core 170-1039B-10H, the

Table 4. Site 1039 smear-slide descriptions.

Sample number							Depth	Imp.		Size				Composition																		Fossils												
Leg	Site	Hole	Core	Type	Section	Interval (cm)	mbsf	Major lithology	Minor lithology	Med.-coarse sand	Fine sand	Silt size	Clay size	Quartz	Feldspar	Clay	Mica	Rock fragments	Volcanic glass	Amphibole	Olivine	Glauconite	Phosphate	Zeolites	Dolomite	Carbonate	Micrite	Opaque	Framboid	Iron oxide	Other	Nannofossils	Foraminifers	Diatoms	Radiolarians	Silicoflagellates	Sponge spicules	Shell debris	Fish remains	Peloids/pellets	Organic matter	Unidentified	Sediment or rock name	Comments
170	1039	A	1	H	3	82	2.32	X				A	C			T																		A	T		C						Dark olive green diatomaceous ooze	
170	1039	A	1	H	2	92	2.42		X	C	A	C	C	A	A	C			C	C		T	T						C			C	T	C	T	T	C		T				Dark olive green silty sand with nannofossils and diatoms	
170	1039	A	1	H	4	62	5.12	X				A	C	T		T												C						A	C	T	C						Dark olive green diatomaceous ooze	
170	1039	A	1	H	5	128	7.28		X		C	A	A		A	A	T		C			T						C	C					C	T		C						Crystal-vitric ash with diatoms and framboids	
170	1039	A	2	H	1	14	9.14	X				C	A	T		T			T	T		T							T					A	C	T	C		T				Dark olive green diatomaceous ooze with radiolarians	
170	1039	A	2	H	2	143	11.93		X	A				C	C	T	T	A	C							T			A				A		T		T						Dark greenish gray coarse sand with pyrite-filled foraminifers	Foraminifers are filled with pyrite
170	1039	A	2	H	3	63.5	12.64		X		C	A	T	T	C			A	T				T						T			T		T			T		T				Crystal-lithic ash	Rock fragments are tephra with feldspar microlites
170	1039	A	2	H	3	74	12.74	X				C	A	C		T	T	C	T	T		T										T		A	T	T	C		T				Dark olive green diatomaceous ooze	
170	1039	A	2	H	5	14	15.14		X		T	C	A	C	T	T		C	A	T									C					A	T		T						Diatomaceous lithic-vitric ash with framboids	
170	1039	A	2	H	7	52	18.52	X				C	A	T		C						T	T						T			C	T	C	C	T	C						Olive green siliceous ooze with nannofossils	

Notes: Imp. = importance. A = abundant, C = common, T = trace, and blank = not observed.

This is a sample of the table that appears on the volume CD-ROM.

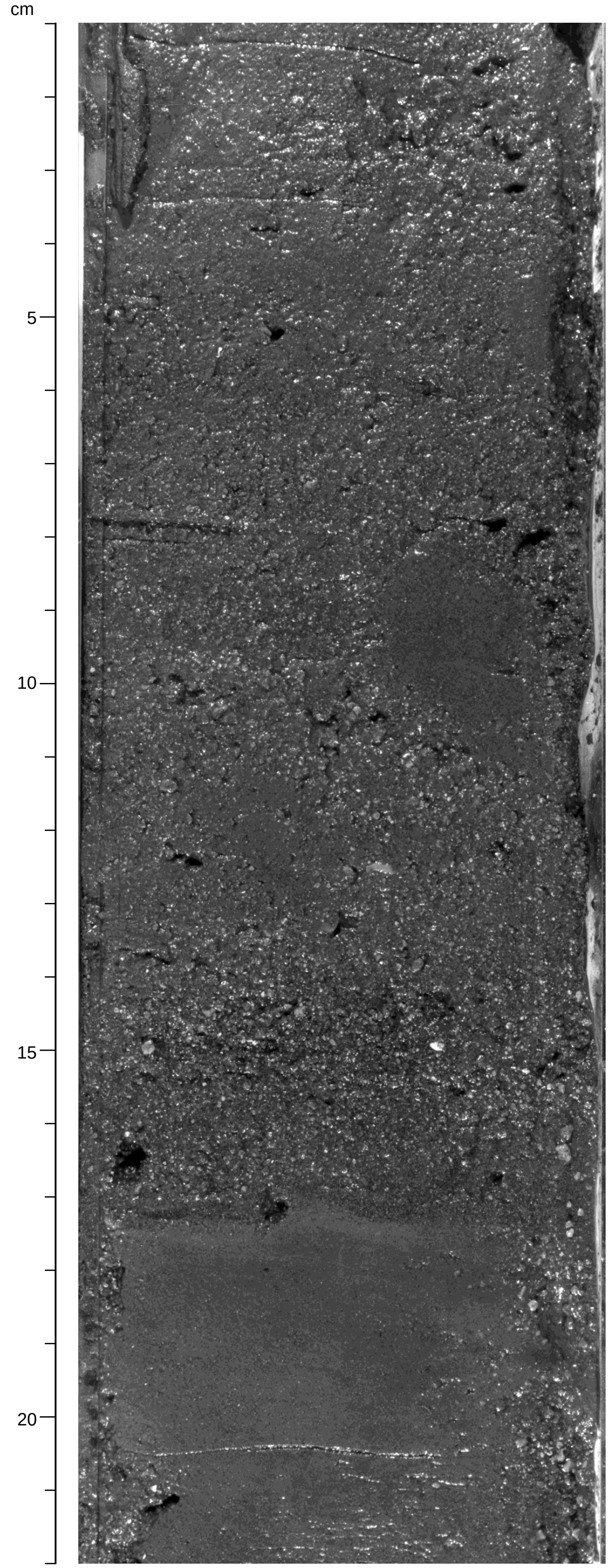

Figure 4. Uppermost layer in Hole 1039B, consisting of medium and coarse terrigenous ashy sand with diatomaceous ooze, grading upward into fine sand and silt. The top 5 cm of this layer is dark reddish brown. Sharp base of layer is scoured into underlying ooze. Streaks of coarse sand along sides of core are drilling disturbance (interval 170-1039B-1H-1, 1–22 cm).

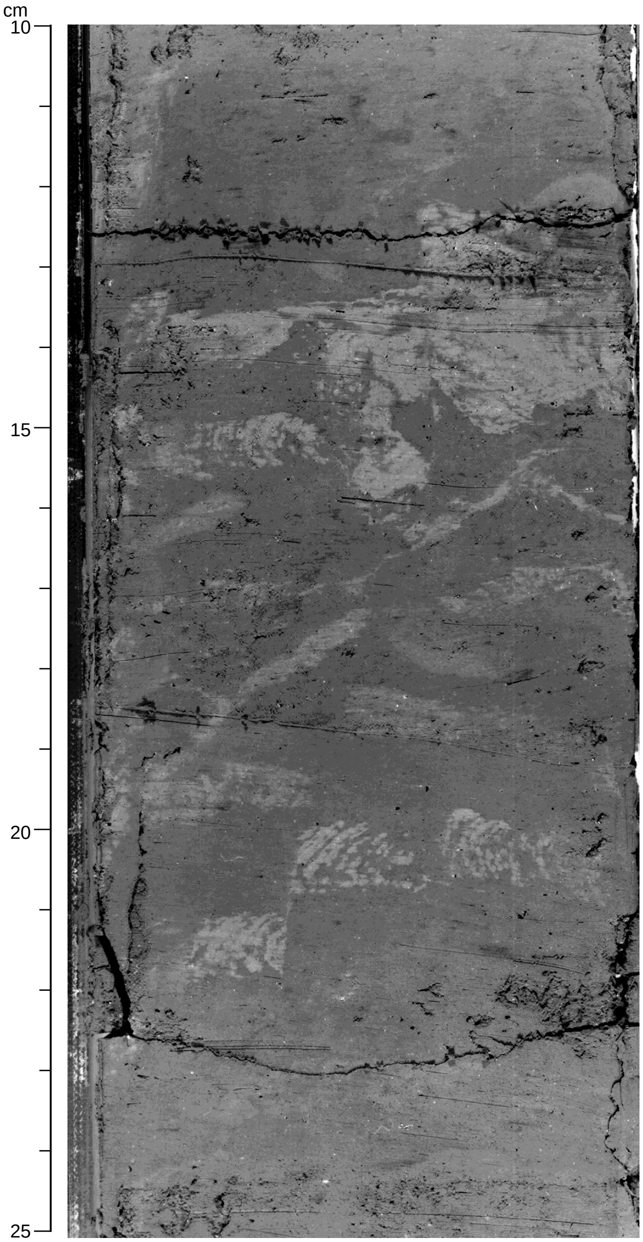

Figure 5. Intensely bioturbated and burrowed interval with *Zoophycos,* typical of burrowed zones throughout Unit U1. Small normal faults offsetting the *Zoophycos* burrows at 20–23 cm may be drilling induced (interval 170-1039B-9H-5, 10–25 cm).

transition probably occurs within about three stratigraphic meters. Most of Unit U2 was intensely disrupted by extended core barrel–related drilling disturbance.

Unit U2 consists of mottled olive green silty clay that is extensively bioturbated and lacks primary sedimentary structures. Local dark greenish gray to black pyrite concentrations and nodules are distributed throughout Unit U2, becoming more common in Subunit U2B. The silty clay typically consists of abundant clay minerals, with clay- to silt-sized clasts of quartz being abundant to common. Other components observed include common to trace amounts of feldspar, amphibole, opaque minerals, volcanic glass, pumice or obsidian scoria, diatoms, radiolaria, and sponge spicules (Table 4).

Subunit U2A contains generally <5% carbonate (Fig. 1). Subunit U2B is distinguished from U2A by light green to greenish gray interbeds of calcareous clay alternating with the darker silty clays. The ap-

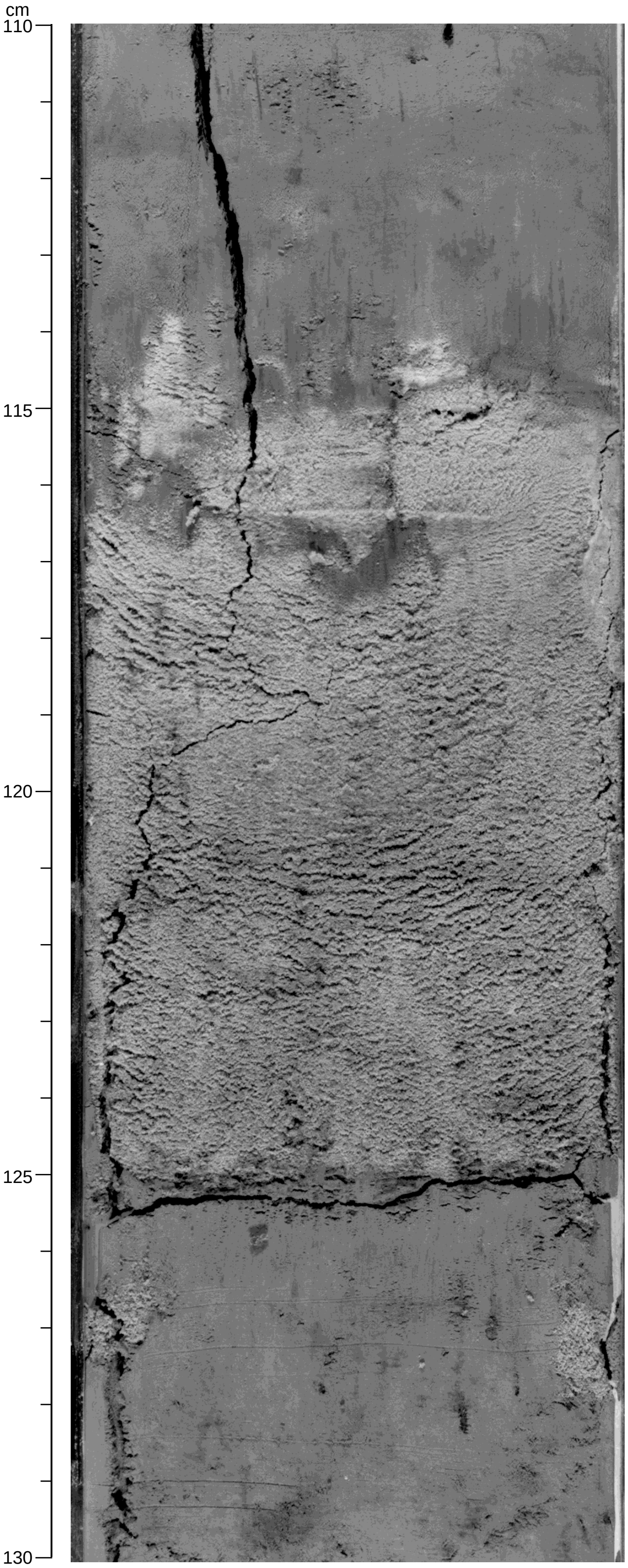

Figure 6. Light gray vitric ash layer with a sharp sand-sized base grading up into silt-sized ash mixed with diatomaceous ooze. This layer is typical of the light-colored ashes in Units U1 and U2 (interval 170-1039B-7H-2, 110–130 cm).

pearance of calcareous interbeds in Subunit U2B correlates with a fluctuation in carbonate content between ~5% and more than 20% (Fig. 1). Nannofossils are common to abundant in Subunit U2B, along with micrite and calcite grains. Foraminifers are present in trace amounts.

Ash layers and pods are common throughout Unit U2, with most being the light gray vitric to dark gray lithic-vitric ashes typical of Unit U1 (Fig. 6). Sparse layers of dark brown, brownish gray, or reddish brown crystal-vitric or lithic-vitric ash occur throughout Unit U2. Volcanic glass, pumice, and scoriaceous obsidian grains are disseminated throughout the clays of Unit U2 in trace to abundant amounts.

Unit U3: Calcareous Ooze

Intervals: 170-1039B-18X-1, 109 cm, to 41X-CC, 35 cm; 170-1039C-1R-1, 0 cm, to 7R-2, 31 cm
Thickness: 225.50 m in Hole 1039B
Depth: 152.49–377.99 mbsf in Hole 1039B; 363.10–422.13 mbsf in Hole 1039C
Age: middle Miocene–early Pliocene

Subunit U3A: Siliceous Nannofossil Ooze and Calcareous Clay

Interval: 170-1039B-18X-1, 109 cm, to 20X-CC, 31 cm
Thickness: 27.89 m
Depth: 152.49–180.38 mbsf
Age: late Miocene–early Pliocene

Subunit U3B: Nannofossil Ooze

Interval: 170-1039B-20X-CC, 31 cm, to 31X-3, 23 cm
Thickness: 99.55 m
Depth: 180.38–279.93 mbsf
Age: middle–late Miocene

Subunit U3C: Nannofossil Ooze, Diatomaceous Ooze, and Breccia

Intervals: 170-1039B-31X-3, 23 cm, to 41X-CC, 35 cm; 170-1039C-1R-1, 0 cm, to 7R-2, 31 cm
Thickness: 98.06 m in Hole 1039B; >59.03 m in Hole 1039C
Depth: 279.93–377.99 mbsf in Hole 1039B; 363.10–422.13 mbsf in Hole 1039C)
Age: early–middle Miocene

The boundary between Units U2 and U3 is placed at the horizon where the composition changes from clay dominated to biogenic dominated. At this interval, the color changes abruptly from green to light greenish gray, the carbonate content fluctuates strongly between 5%–10% and 20%–40% (Fig. 1), and color reflectance begins a fluctuating increase in the median reflectance 400–700 nm (Fig. 1). Distinct ash layers are rare, as are terrigenous components, and the entire unit is extensively bioturbated.

Subunit U3A is a transitional unit that consists of light gray to ivory white siliceous nannofossil ooze interbedded with green calcareous nannofossil-rich clay. The clay-sized fraction of the ooze consists of abundant nannofossils, abundant to common micrite, and common to trace amounts of crystalline calcite (Table 4). Trace amounts of foraminifers and siliceous microfossils are also present, with the siliceous material increasing downsection. Volcanic glass is common in the ooze, but terrigenous components such as quartz and feldspar are present only in trace amounts. The calcareous clay is silty, with common to abundant clay minerals mixed with common to trace amounts of nannofossils and micrite. Terrigenous components are slightly more abundant in the clays than in the oozes, but decrease in abundance downsection until they nearly disappear around 180 mbsf.

Ooze and clay layers in the upper part of Subunit U3A range from 0.1 to 0.75 m thick, with the ooze layers gradually thickening downward until the sediment consists entirely of the nannofossil ooze of Subunit U3B. The greenish clay disappears abruptly within a drilling breccia at the base of Core 170-1039B-20X, marking the top of Subunit U3B. This lithologic change corresponds to a jump in carbonate content to >50%, and the carbonate content remains >30% to the base of Subunit U3B (Fig. 1). This contact also corresponds to a sharp jump in many physical properties (Fig. 1; see "Physical Properties" section, this chapter).

Subunit U3B ranges in color from ivory white to light gray, with mottled patches, bands, and diffuse layers of lavender, green, yellow, pink, and gray. Some of the dark gray to black colors seem to be associated with pyritiferous zones, but no reason for the other colors could be determined from smear slides. In composition, Subunit U3B varies from nannofossil ooze with siliceous microfossils to siliceous ooze with nannofossils. Although this terminology reflects changing proportions of siliceous and calcareous components, the unit is dominated by nannofossils with diatoms, sponge spicules, foraminifers, radiolarians, and silicoflagellates in decreasing order of abundance (Table 4). Micrite and silt-sized carbonate grains are common to abundant throughout Subunit U3B, but terrigenous grains such as quartz and feldspar are almost completely absent.

Although ubiquitous throughout Subunit U3B, disseminated volcanic glass is generally present only in trace amounts (Table 4). The rare layers of volcanic ash are dark gray to black vitric and crystal-vitric ash (Fig. 7). They differ from the light to dark gray ashes of Units U1 and U2 in that they contain brown glass, and pumice fragments are uncommon.

The top of Subunit U3C is defined by a pair of dark green diatomaceous ooze layers clearly visible in the photograph of Section 170-1039B-31X-3. This interval was not cored in Hole 1039C, but a similar pair of layers was observed at Site 1040. These diatom-rich layers, a few centimeters thick and about 15 cm apart, mark the beginning of an increase in diatom mats and diatomaceous ooze layers, which become increasingly important downhole until the base of the unit is dominated by diatoms rather than nannofossils. Subunit U3C consists of green and gray siliceous calcareous oozes and diatomaceous oozes interbedded with strongly mottled, ivory white calcareous oozes. Burrows are commonly filled with material of contrasting color reworked from adjacent layers (Fig. 8).

The base of Subunit U3C records the unexpected appearance of clastic layers, just above the gabbro intrusion of Unit U4. Although the subunit is dominated by biogenic material, it is the minor layers of volcaniclastic sands, silts, and graded granule-pebble breccias (Fig. 9) that stand out as important marker lithologies that were also recognized in Site 1040 cores below the décollement (see "Site 1040" chapter, this volume). These thin and volumetrically minor clastic layers are an important addition to the tectonic story.

Many of the coarse-grained layers in Subunit U3C are matrix-supported ooze breccias, with varicolored graded assemblages of clasts composed of calcareous and siliceous oozes (Fig. 9). The grading in Figure 9 is subtle, but if only the largest grains at each internal horizon within the bed are considered it becomes clear that overall grain size decreases upward. Ooze clasts are angular to subrounded in shape, and some layers are clast supported. Sharp-scoured bases are common in the coarse-graded beds of ooze fragments, suggesting debris-flow deposition. In Hole 1039B, about 10% of the coarse layers in the lower 30 m of Subunit U3C consists of tephra fragments suspended in ooze, or of clast-supported tephra layers with ooze matrix. Some tephra-rich layers are thinly laminated. The best marker lithology is light brown, with graded thin laminae (Fig. 10), and consists of ash-rich calcareous ooze grading upward into ash-rich diatomaceous ooze. This distinctive lithology was recovered in both Holes 1039B (0.92 m thick in interval 170-1039B-41X-2, 85 cm, to 41X-3, 28 cm) and 1039C (1.37 m thick in interval 170-1039C-5R-1, 48 cm, to 6R-1, 27 cm), as well as in Hole 1040C below the décollement (see "Site 1040" chapter, this volume).

Dark gray to black scoriaceous obsidian clasts are common throughout Subunit U3C as isolated fragments within the oozes (Fig. 10) and as coarse sand- to gravel-sized fragments within the clastic layers. Distinct layers of vitric, crystal-vitric, and lithic-vitric ash and lapilli are common throughout the lower part of Subunit U3C. The volcanic ash contains a significant component of brown glass in addition to clear glass. The ash layers range in color from dark gray to black and from reddish brown to light or dark brown.

Preliminary shipboard XRF results show that the basal oozes of Subunit U3C are metalliferous, being enriched in zinc, nickel, and copper (see "Geochemistry" section, this chapter). Varicolored Liesegang rings surround the numerous burrows (Fig. 11), as well as layers in which diatom spicules are concentrated. The Liesegang rings are concentrated around some, but not all, of the tephra clasts (Fig. 11).

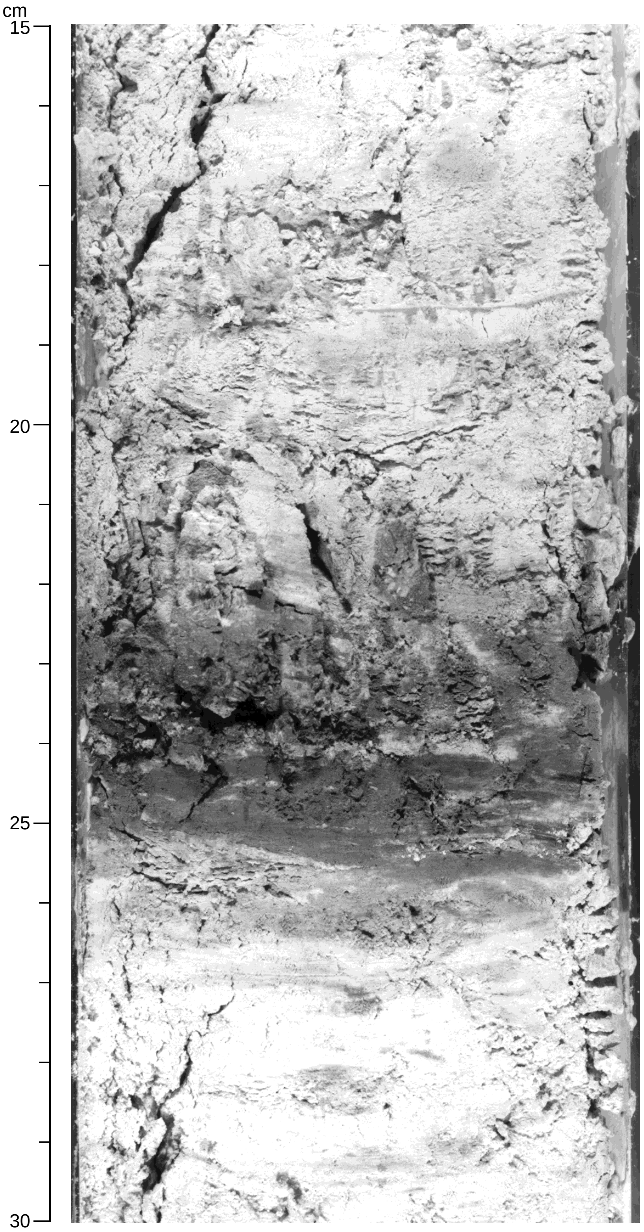

Figure 7. Black crystal-vitric ash layer in ivory white nannofossil ooze. Dark ashes in Subunit U3B differ from the gray ashes of Units U1 and U2 in the absence of pumice and the presence of brown glass rather than clear glass (interval 170-1039B-31X-3, 15–30 cm).

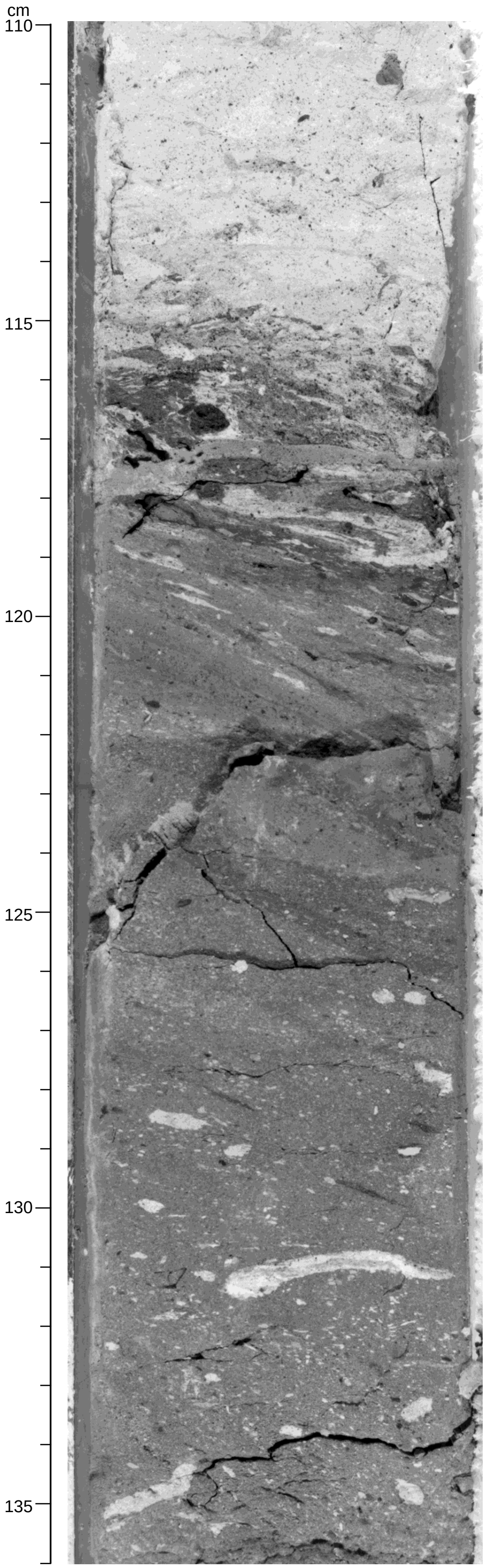

Figure 8. Typical dark green diatomaceous ooze layer of Subunit U3C. Burrows are filled with white nannofossil ooze reworked from adjacent layer (interval 170-1039B-40X-1, 110–136 cm).

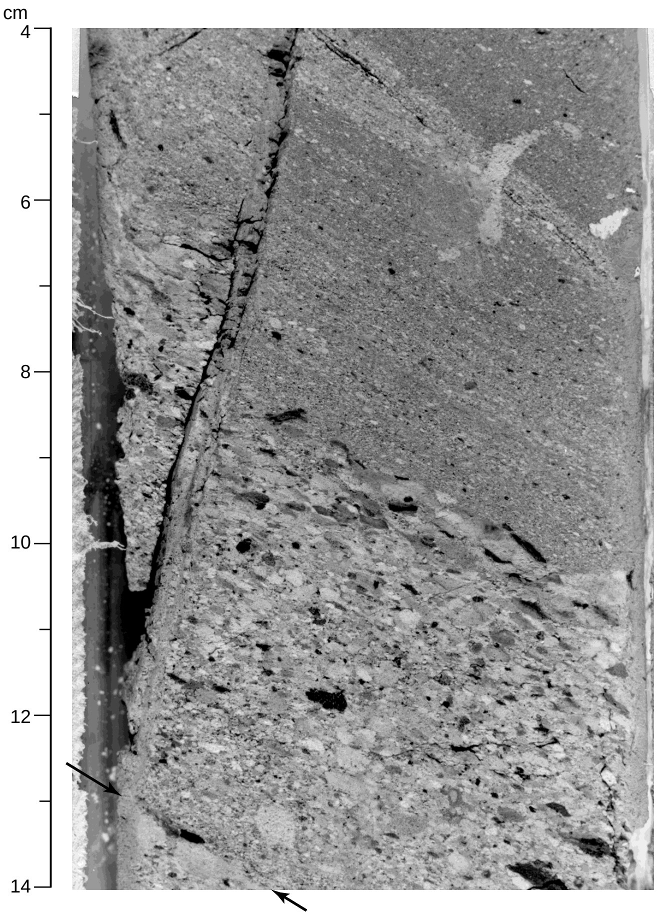

Figure 9. Graded bed of granule-pebble breccia with a sharp scoured base (arrows), Subunit U3C. Chalk-filled burrows penetrate the sandy layers. Fault is a drilling disturbance (interval 170-1039B-40X-2, 4–14 cm).

Unit U4: Pyroxene Gabbro

Intervals: 170-1039B-41X-CC, 35 cm, to 42X-1, 30 cm; 170-1039C-7R-2, 31 cm, to 11R-2, 92 cm
Thickness: >23.03 m in Hole 1039C
Depth: 377.99–381.0 mbsf in Hole 1039B; 422.11–445.14 mbsf in Hole 1039C
Age: post-15.6 Ma in Hole 1039B; post-16.49 Ma in Hole 1039C

Unit U4 consists of pyroxene gabbro, recovered from both Holes 1039B and 1039C. Gabbro was first encountered at 377.9–381 mbsf in Hole 1039B, during the XCB drilling. Only rubble was recovered from this layer in Hole 1039B. In Hole 1039C, gabbro was recovered from 422.11 to 445.14 mbsf before terminating the hole. The reason for the different depths of the top of the gabbro at the two sites remains unknown. Samples recovered from Holes 1039B and 1039C are very similar in hand specimen and thin section, supporting our interpretation that they represent the same or closely related intrusions.

Unit U4 consists of fine-grained one-pyroxene (augite) gabbro with medium-grained glomerocrysts of plagioclase or, more rarely, plagioclase plus pyroxene, in a nearly to completely holocrystalline matrix (Fig. 12). The gabbro of Unit U4 is clearly intrusive into the basal sediments of Unit U3. An inclined, irregular glassy contact was recovered in Sample 170-1039C-7R-2, 32–34 cm. Sediment along the contact is a 2-cm-thick band of hard, dark green hornfels containing relict quartz clasts, glass shards, and nannofossils. The contact crosscuts bedding at a steep angle, suggesting that the intrusion is not a simple sill.

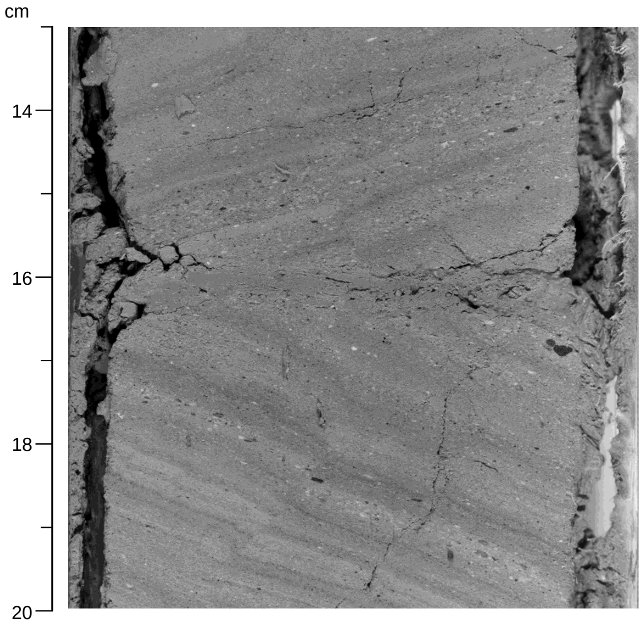

Figure 10. Tephra beds interbedded with graded thin laminae of ash-rich diatomaceous ooze and calcareous ooze. This distinctive light brown unit was recovered just above the gabbro intrusion in Holes 1039B and 1039C, as well as in Hole 1040C. A drilling-induced fault crosses the core face horizontally at about 16 cm, dividing the core into two "biscuits" rotated relative to each other (interval 170-1039B-41X-3, 13–20 cm).

Hand-sample, thin-section (Table 5), and operational data indicate that more than one intrusion was drilled in Hole 1039C. Chilled margins were recovered at 423.5 mbsf (0.5 cm thick), 431.6 mbsf (0.5 cm thick) and 445 mbsf (1.0 cm thick). Penetration rates were generally very slow through the igneous rocks in Hole 1039C. However, drilling breaks accompanied by significant increases in ROP were observed by the driller at approximately 431–432 mbsf and 439–442 mbsf, suggesting significantly softer material that was not recovered in the cores. We tentatively interpret these softer intervals as sediment between different apophyses of gabbro. Altogether, these results suggest multiple intrusions into the Miocene ooze and clastics of Subunit U3C. These intrusions are post-15.6 to -16.4 Ma in age, based on nannofossils in the intruded oozes.

Textural and structural features seen in core hand specimens include variations in grain size and proportions of plagioclase, pyroxene, and glass, as well as both glass-filled and mineral-filled veins as much as 3 mm thick (Fig. 12). Some of the grain size variations probably represent chilled margins (Fig. 13A) or cumulate layering. The late-stage, mineral-filled fracture veins (Fig. 14) contain calcite, chlorite, zeolite, and trace amounts of pyrite and chalcopyrite.

Eighteen thin sections from the two holes were examined petrographically, and mineral proportions were estimated visually (Table 5). Small textural and mineralogical variations are noted in cores from throughout Hole 1039C, but all thin sections share many common features. Glomerocrysts (1–5 mm across) of euhedral to subhedral plagioclase or, more rarely, euhedral to subhedral plagioclase plus subhedral clinopyroxene, are present in all thin sections, and constitute 3%–15% of the rock. Plagioclase in the glomerocrysts is bytownite-anorthite ($An_{85–95}$) and the pyroxene is augite. Stubby augite prisms 0.1–1 mm across and plagioclase laths ($An_{78–85}$) 0.2–0.8 mm across are the major phases observed in all thin sections (4%–40% augite and 15%–47% plagioclase).

Many plagioclase laths form rosettes or sprays. The spaces between laths are occupied by the smaller augite grains, opaque minerals with exsolution lamellae, or greenish brown glass with variable degrees of alteration. The opaque minerals as much as 0.2 mm in size are probably titanomagnetite, based on reflected light observations. The interstitial glass is partly to completely replaced with saponite and commonly a trace of chlorite and zeolite (natrolite?). Acicular to anhedral titanomagnetite (?) is common within the interstitial melt pockets, and traces of sulfides (probably pyrite and chalcopyrite) are also present within the interstitial glass. Below 444.8 mbsf, most of the interstitial glass is crystallized into microphenocrysts (0.02–0.06 mm) of plagioclase and pyroxene.

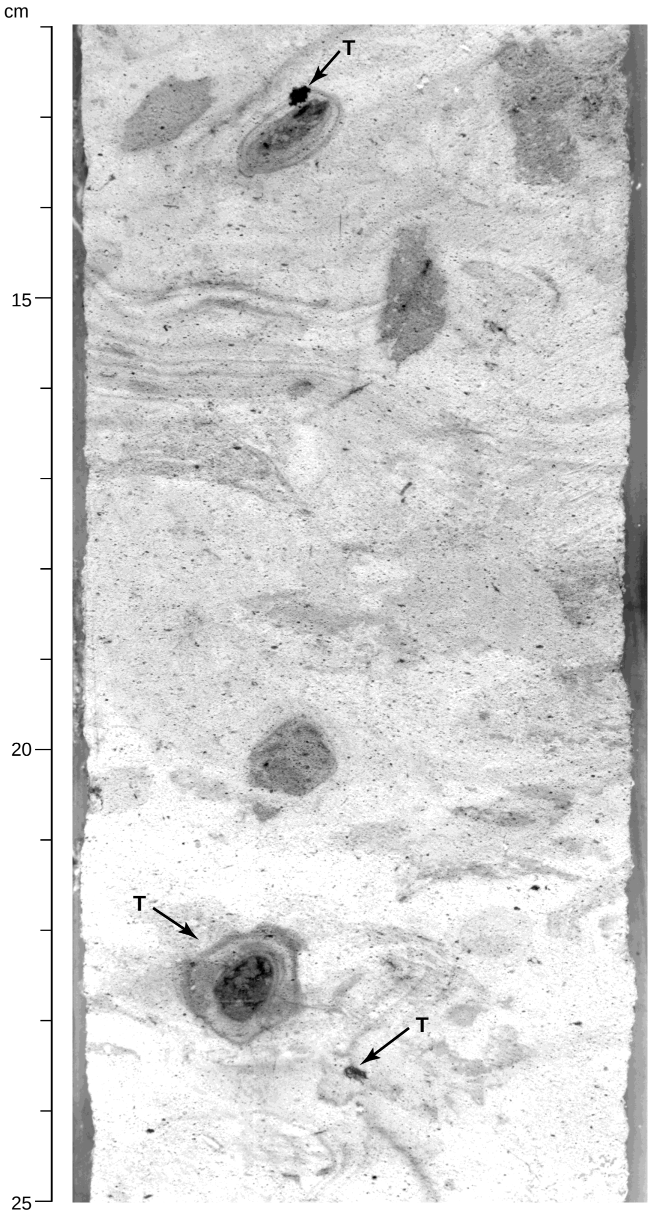

Figure 11. Varicolored halos of Liesegang rings around burrows and diatom spicule concentrations in the calcareous oozes of Subunit U3C. Large isolated black clasts are tephra (labeled "T"; interval 170-1039C-1R-3, 12–25 cm).

Features that vary with depth are shown in Figure 13 and Table 5. Glass percentages observed in the cores and in thin sections peak at three stratigraphic levels, suggesting chilled margins at about 423.5, 431.7, and 445 mbsf (Fig. 13A). Proportions of glomerocrysts vary from ~3% to 15%, with highest percentages observed near chilled

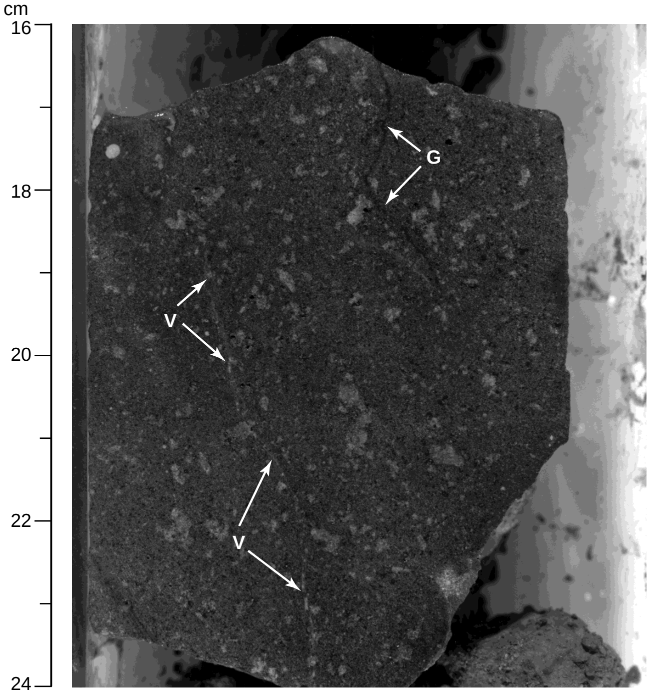

Figure 12. Glomeroporphyritic pyroxene gabbro of Unit U4. The large white clots are clusters of plagioclase crystals that comprise the glomerocrysts. The fine-grained groundmass consists of smaller plagioclase laths, stubby augite grains, skeletal titanomagnetite, and interstitial glass. A very thin glassy vein (labeled "G") crosses the specimen from 20 to ~17 cm. A second vein (labeled "V") crosses the specimen from 24 to ~17 cm and probably represents a filled fracture (interval 170-1039B-24X-1, 16–24 cm).

margins (Fig. 13A, B). Augite grains are largest near the base of the recovered igneous section (Fig. 13C).

Textural and mineralogical characteristics seen in core and thin sections suggest an origin that is at least partly cumulate. Faint layers and laminations can be observed in the cores themselves, especially around 473 mbsf (Sample 170-1039C-8R-1, 43–45 cm). The tendency of augite grains to concentrate near the base of the section suggests that they may have settled (Fig. 13C). Near the base of the recovered section, some relatively large pyroxene grains appear to poikilitically enclose small plagioclase grains. The intervals between poikilitic pyroxenes are filled by a fine-grained groundmass composed of euhedral to subhedral plagioclase laths with subhedral pyroxene and interstitial glass, suggesting an alternation of plagioclase and pyroxene crystallization, ending with sudden chilling of the final fluid.

Minor glass veins 1–2 mm wide are observed in a number of thin sections and in the cores (Fig. 12). These veins are petrographically identical to the interstitial glass observed in most thin sections. They consist of greenish brown glass, devitrified and generally altered to saponite plus chlorite and traces of zeolite, with minor crystals of plagioclase, opaques, and sulfides. The veins are generally undulose to anastomosing, and in some cases break apart and slightly rotate grains through which they pass. These observations suggest that melt veins were injected forcefully into a body that was largely crystalline, but not yet completely solidified. We speculate that the glass veins may have been derived from filter pressing during crystal settling and accumulation.

Structural Geology

The cores recovered at Site 1039 are only slightly to moderately deformed by drilling disturbance because the sediments are generally firm. The unit with the most drilling disturbance is Unit U2, where the first XCB cores were recovered. The recognition of drilling-produced structures is discussed in the "Explanatory Notes" chapter (this volume). Figures 8 through 10 exhibit fractures or faults that are examples of drilling disturbance.

Sediments recovered at Site 1039 show little evidence of deformation by tectonic processes except in Subunit U3C. Unit U1, from 0 to 84.43 mbsf, exhibits subhorizontal bedding attitudes, with undeformed sedimentary structures. Unit U2, from 84.43 to 152.49 mbsf, also exhibits subhorizontal bedding. In Core 170-1039B-9H (~69.5–71.5 mbsf), at least three normal faults were observed with displacements of 2–10 cm and a core-face trace length of about 20 cm. Along one fault plane, a 1-cm-thick zone of cohesive, unfoliated cataclasite was observed.

Most of Unit U3 was too soft to be cut with a saw and the wire cutter caused homogenization of the core surfaces, rendering any structures present indistinguishable. Structures were displayed well only in the lower part of Subunit U3C (Cores 170-1039B-39X through 41X and 170-1039C-1R through 7R). Subunit U3C corresponds to the breccia- and conglomerate-rich zone (Figs. 9, 10). Several small faults nearly perpendicular to bedding and shear zones parallel to bedding were observed with displacements on the order of a few millimeters to centimeters (Fig. 10). Cores of Subunit U3C also exhibit apparent pressure solution surfaces, resulting in an incipient stylolitization (Fig. 15), together with some very weakly developed mullions. Both the stylolites and the mullions represent a flattening perpendicular to the bedding. The close spatial association of these features with the debris-flow breccias and igneous intrusions suggests that this deformation is the result of intrusion emplacement and perhaps near-ridge tectonic processes (tilting and fault block rotation).

In summary, the evidence of post-depositional deformation exhibited at Site 1039 consists of some minor faulting and bedding-perpendicular flattening near the base, and only very minor faulting above that. From a structural point of view, Site 1039 represents a good reference site for the lower continental slope sites.

Discussion

The sand layers in Subunit U1A are probably turbidites, as suggested by their sharp scoured contacts, internal grading, and the terrigenous nature of their coarse components. The lack of turbidites below 5.55 mbsf suggests a fairly recent change in the sedimentation style of this part of the Cocos Plate, probably caused by its approaching the Middle America Trench. The numerous ash pods and ash-filled burrows as well as the ubiquitous disseminated tephra throughout the stratigraphic section at Site 1039 suggest extensive biogenic reworking of ash layers; it is likely that only relatively thick ash deposits or those that were rapidly buried have survived as discrete original layers. The graded tephra layers with sharp bases, seen throughout the stratigraphic section, are turbidites rather than air-fall deposits. This interpretation suggests extensive redeposition of the volcanic material.

The relatively low proportion of biogenic components in Unit U2, compared with Units U1 and U3, is difficult to explain. Smear-slide observations indicate that siliceous microfossils are nearly absent and calcareous microfossils are much less common than in Units U1 and U3.

The clastic layers in Subunit U3C (Fig. 9) exhibit debris flow and turbidite features (graded beds with sharp scoured bases). These Subunit U3C volcaniclastic layers suggest a nearby source of scoriaceous obsidian and crystal-vitric ash, possibly the Galapagos Hotspot. The isolated tephra lapilli that are commonly suspended in the oozes of Subunit U3C also support the proximity of a nearby volcaniclastic source. Their number and distribution suggest relatively constant pyroclastic deposition. The Subunit U3C breccias, composed of ooze fragments, suggest submarine erosion of pelagic sediments and redeposition by debris flows and turbidites.

Table 5. Thin-section summary for gabbros.

Site	Hole	Core	Section	Top (cm)	Piece	Depth (mbsf)	Rock type	Glom (%)	Size, glom	Plag (%)	Size, laths	Cpx (%)	Size, px	Glass (%)	Alt (%)	Comments
1039	B	42X	1	22		381.0	Gabbro	20	4	33	0.20	37	1.0	0	5.0	Vein
1039	C	7R	2	31		423.5	Gabbro	5	3	16	0.30	10	0.1	10	10.0	
1039	C	7R	2	31		423.5	Chilled margin	3	1	35	0.08	10	0.1	50	25.0	Chilled margin
1039	C	7R	2	43		423.7	Gabbro	10	7	45	0.60	40	0.2	2	3.0	
1039	C	7R	3	73		425.5	Gabbro	5	1	40	0.80	40	0.6	5	5.0	
1039	C	8R	1	7	3	431.6	Gabbro	25	5	28	0.08	27	0.1	15	15.0	
1039	C	8R	1	7	3	431.6	Chilled margin	15	1.5	10	0.04	10	0.0	58	15.0	Chilled margin
1039	C	8R	3	90	1B	434.2	Gabbro	5	4	50	0.20	40	0.3	3	2.0	
1039	C	8R	5	63	2	436.5	Gabbro	3	2	42	0.30	42	0.2	5	20.0	Larger grains fractured
1039	C	9R	1	1	1A	437.1	Gabbro	5	3	35	0.50	45	0.4	10	15.0	Larger grains fractured
1039	C	9R	2	45	2	438.8	Gabbro	3	4	47	0.50	40	0.3	5	6.0	Partial cumulate?
1039	C	10R	1	64	10	441.8	Gabbro	5	3	75	0.50	11	0.1	5	20.0	Glass vein
1039	C	10R	3	25	1B	443.3	Gabbro	5	3	51	0.40	34	0.3	5	8.5	Larger grains fractured
1039	C	11R	1	58	5	444.8	Gabbro	15	5	14	0.20	15	1.5	5	13.0	Seriate porphyritic
1039	C	11R	1	82	7	445.0	Gabbro	15	4	21	0.20	4	1.5	15	17.0	Seriate porphyritic
1039	C	11R	1	82	7	445.0	Chilled margin?	10	2	35	0.05	25	0.2	30	30.0	Chilled margin?
1039	C	11R	2	47	1C	445.6	Gabbro	10	4	40	0.40	40	0.8	5	5.5	Glass vein
1039	C	11R	2	74		445.9	Gabbro	10	3	39	0.60	37	1.0	9	5.0	Glass vein; cumulate?

Notes: Glom = glomerocryst, Plag = plagioclase, Cpx = clinopyroxene, px = pyroxene, and Alt = alteration. Mineral sizes are in millimeters.

This table also appears on the volume CD-ROM.

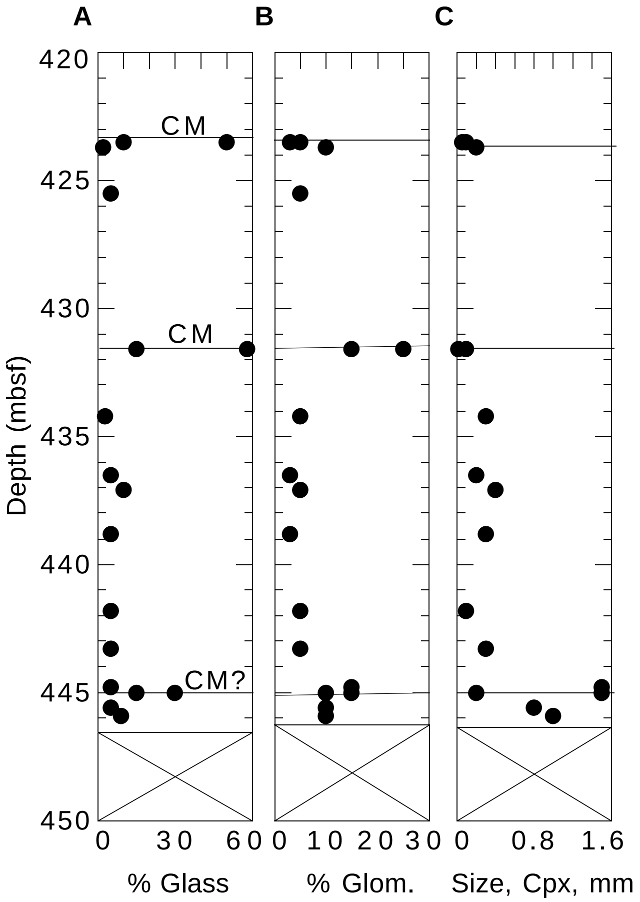

Figure 13. Compositional variations with depth in pyroxene gabbro. **A.** Percentage of glass is nearly constant at <10% except at 423.5, 431.7, and 445 mbsf, which may represent chilled margins (CM) of multiple intrusions. **B.** Percentage of glomerocrysts appears to correlate with the chilled margins. **C.** Percentage of pyroxene increases near the base of the recovered section.

Evidence for a Galapagos Hotspot signature in the tephra record is seen in the overall distribution of ashes and in their composition, as well as in the proximity to the Cocos Ridge. Layers of ash and tephra turbidites are most common in two stratigraphic intervals at Site 1039: below 277 mbsf and above 200 mbsf. The lower interval (below 277 mbsf), where the brown-glass–rich, crystal-vitric ashes, and tephra layers dominate the record, probably represents a Galapagos source. As the Cocos Plate moved eastward away from the Galapagos Hotspot, Site 1039 entered a zone relatively far from volcanic sources, explaining the scarcity of ash in the interval 200–277 mbsf. The upper interval of strata (above 200 m) is dominated by the gray lithic-vitric ashes, which are probably derived from the Central American Arc. As Site 1039 (riding on the Cocos Plate) approached the arc, it moved out of the ash-barren zone into the zone of arc deposition. The preliminary geochemical results of shipboard XRF on selected ash layers also supports our interpretation of two distinct sources (see “Geochemistry” section, this chapter).

Although the seismic section at this site (Fig. 3) shows a high-amplitude horizontal reflection at about the right location for the gabbro intrusion and termination of the reflection 1 km from Site 1039, which tempts one to interpret it as a sill, the only contact recovered cut across bedding at a steep angle. Thus, the gabbro is at least locally not a sill, because it is not parallel to bedding. Evidence from depth of recovery and ROP also supports the interpretation of multiple gabbro intrusions or a single intrusion that crosses bedding very steeply.

Our main purpose at Site 1039 was to establish a reference section to compare with the sequence recovered from below the décollement at Site 1040. Although we never reached oceanic basement and thus do not know its exact age or composition in this part of the Cocos Plate, the sedimentary and igneous section recovered was distinct enough to correlate with the subducted section at Site 1040. Furthermore, the correlation includes specific marker beds and lithologic subunits within the recovered sequences at both sites.

BIOSTRATIGRAPHY AND MAGNETOSTRATIGRAPHY

Biostratigraphy

Calcareous nannofossils, diatoms, and planktonic foraminifers are present in all three holes drilled at Site 1039, immediately seaward of the Middle America Trench. With a few exceptions, descriptions of the microfossil assemblages from each core are for core-catcher samples only. A summary of the biostratigraphic zonations observed at Site 1039 is given in Figure 16.

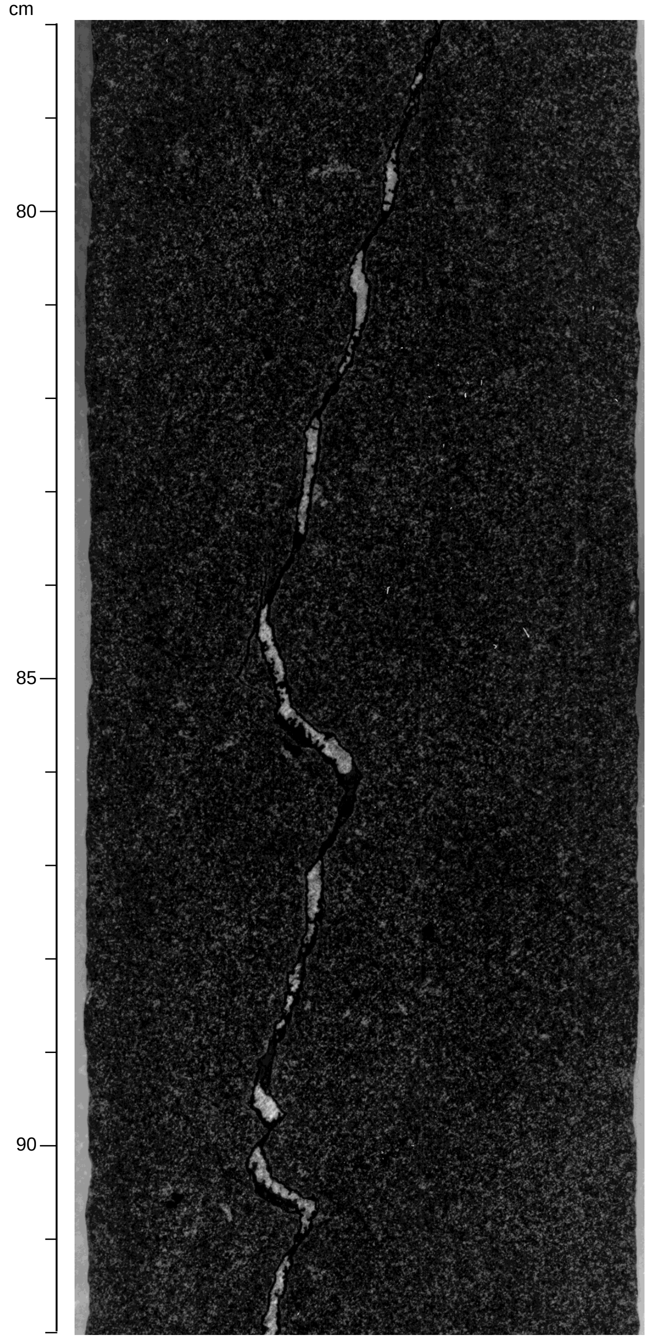

Figure 14. Fracture vein in pyroxene gabbro intrusion, filled with calcite (light), chlorite and zeolite (dark), minor pyrite, and chalcopyrite. Weak grain-size gradation in the gabbro is visible from 92.5 to 80 cm (interval 170-1039C-10R-2, 78−92 cm).

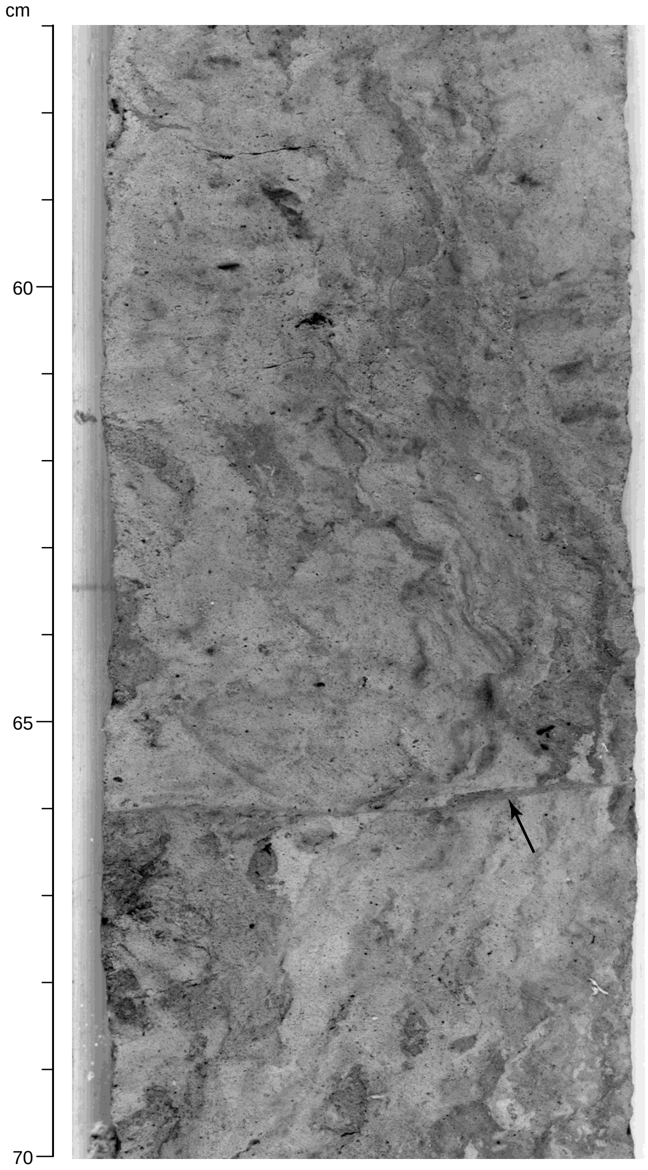

Figure 15. Pressure solution feature (arrow) in varicolored siliceous nannofossil oozes of Subunit U3C (interval 170-1039C-6R-3, 57−70 cm).

Calcareous Nannofossils

The occurrence, abundance, and preservation of the calcareous nannofossils recovered from Site 1039 are reported. The letters in parentheses after species names for Hole 1039A indicate the abundance of that species, as discussed in the “Explanatory Notes” chapter (this volume). A range-distribution chart is presented for calcareous nannofossils observed in Hole 1039B (Table 6).

Hole 1039A

Calcareous nannofossils are not present in Sample 170-1039A-1H-CC, nor are nannofossils present in several samples observed immediately upsection in this core. However, Sample 170-1039A-2H-CC contains *Gephyrocapsa* spp. (F), *Calcidiscus leptoporus* (R), and *Gephyrocapsa oceanica* (F), which are all poorly to moderately preserved.

Nannofossils are abundant and moderately preserved in Sample 170-1039A-3H-CC. Present are small *G. oceanica* (A), large *G. oceanica* (A), *G. caribbeanica* (A), *Helicosphaera carteri* (C), *G. sinuosa* (A), and *C. leptoporus* (A).

The absence of *Pseudoemiliania lacunosa* indicates that the assemblages in all three samples from this hole are characteristic of Zones NN21/NN20. The presence of *Emiliania huxleyi* in Samples 170-1039A-2H-CC and 3H-CC will be determined by shore-based scanning electron microscope (SEM) analysis.

Hole 1039B

Core-catcher Samples 170-1039B-1H-CC through 5H-CC contain assemblages of poorly to moderately preserved calcareous nannofossils in abundances of few to abundant. Dominating the assemblages are both large and small *G. oceanica* and *G. caribbeanica*. Also present are *C. leptoporus*, *Helicosphaera carteri*, *H. hyalina*, and *Ceratolithus cristatus*. Assemblages in these samples are tentatively assigned to Zones NN21/NN20, based on the absence of *P. lacunosa*. Shore-based SEM analysis will determine the presence of *E. huxleyi*.

The last occurrence (LO) of *P. lacunosa* (0.46 Ma) occurs in Sample 170-1039B-6H-CC. The occurrence of *P. lacunosa* and the absence of *Discoaster brouweri* and *Helicosphaera sellii* indicate that this assemblage is characteristic of the Pleistocene interval of Zone NN19. Assemblages that indicate Zone NN19 are also found in Samples 170-1039B-7H-CC, 8H-5, 89 cm; 9H-5, 14 cm; and 10H-CC. Core-catcher Samples 170-1039B-8H-CC and 9H-CC are barren. Nannofossils occurring in this interval include *P. lacunosa*, large *G. oceanica*, small *G. oceanica*, *C. leptoporus*, *H. carteri*, *Pontosphaera discopora*, *G. caribbeanica*, *Helicosphaera neogranulata*, and *Helicosphaera columbiana*. All samples exhibit good preservation.

The LO of *H. sellii* (1.47 Ma, equatorial Pacific) and the absence of *Gephyrocapsa* species are observed in Sample 170-1039B-11H-CC. The remaining assemblage is similar to that found upsection in Sample 170-1039B-6H-CC, and is representative of the Pleistocene and latest Pliocene Zone NN19. Preservation is good. Sample 170-1039B-12X-CC does not contain nannofossils.

The LO of *Discoaster brouweri* (1.95 Ma) is observed in Sample 170-1039B-13X-CC. The LO of *D. brouweri* defines the top of late Pliocene Zone NN18. Both Samples 170-1039B-13X-CC and 14X-

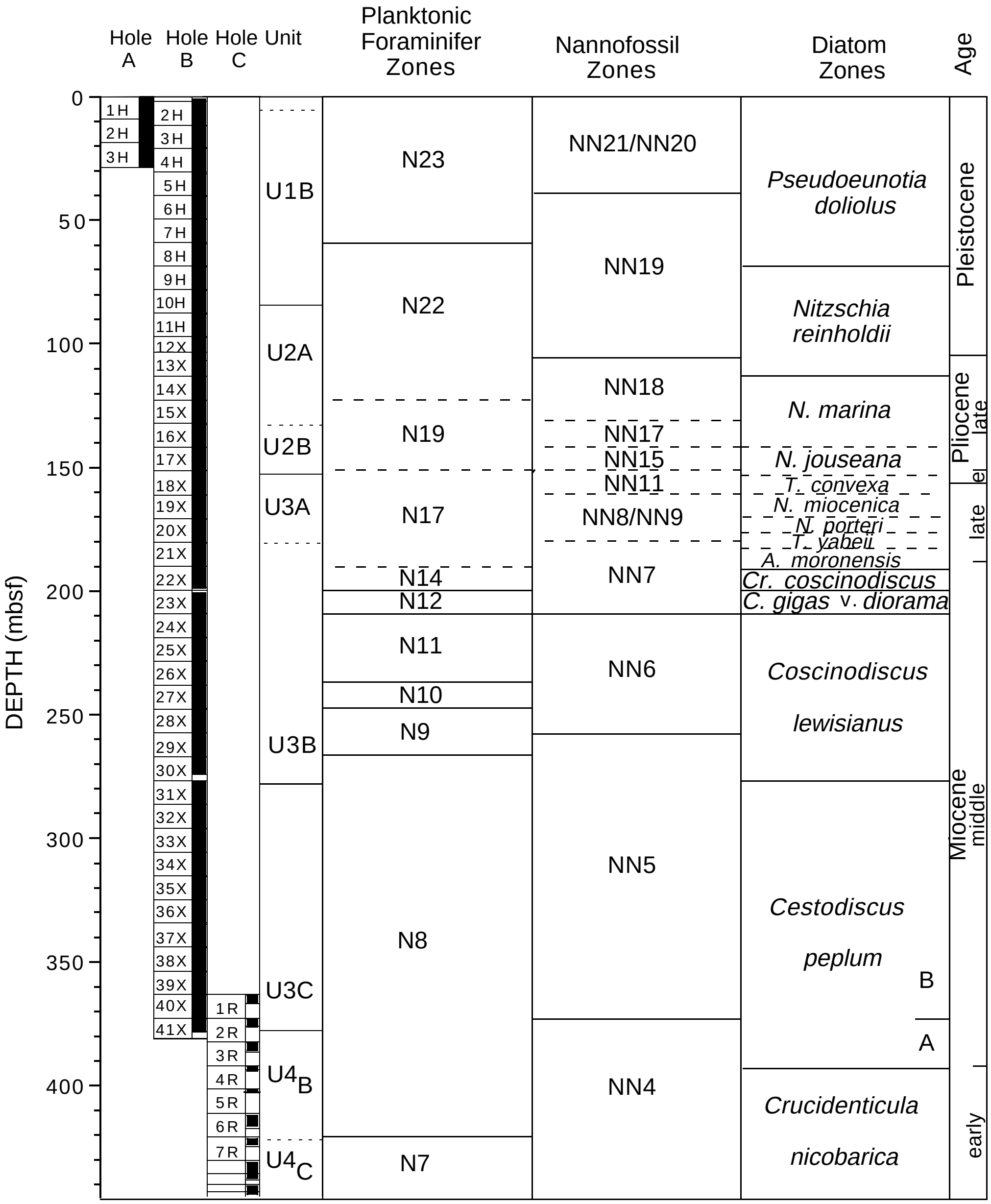

Figure 16. Correlation of the planktonic foraminifer, calcareous nannofossil, and diatom zones with Site 1039 cores and sedimentary units. Dashed lines represent uncertainty in placement of the zonal boundary.

Table 6. Calcareous nannofossil range distribution chart for Hole 1039B.

Calcareous nannofossil zone(s)	Core, section	Depth (mbsf)	Abundance	Preservation	Small reticulofenestrids	*Coccolithus miopelagicus*	*Coronocyclus nitescens*	*Cyclicargolithus floridanus*	*Discoaster deflandrei*	*Discoaster intercalaris*	*Helicosphaera ampliaperta*	*Helicosphaera carteri*	*Reticulofenestra pseudoumbilicus*	*Sphenolithus heteromorphus*	*Sphenolithus moriformis*	*Discoaster variabilis*	*Sphenolithus verensis*	*Pontosphaera discopora*	*Calcidiscus leptoporus*	*Calcidiscus macintyrei*	*Discoaster exilis*	*Hayaster perplexus*	*Discoaster kugleri*	*Discoaster bellus*	*Sphenolithus abies*	*Discoaster berggrenii*	*Discoaster brouweri*	*Discoaster neorectus*	*Discoaster quinqueramus*	*Discoaster surculus*	*Discoaster asymmetricus*	*Discoaster misconceptus*	*Gephyrocapsa caribbeanica*	*Gephyrocapsa oceanica*	*Helicosphaera sellii*	*Helicosphaera neogranulata*	*Pseudoemiliania lacunosa*	*Ceratolithus cristatus*	*Helicosphaera hyalina*	*Emiliania huxleyi*	Unidentifiable 6-rayed discoasters	Unidentifiable placoliths
NN21	1H-1	0	F	P																													F							F		
NN21-NN20	1H-CC	1.9	A	M								C							A														A	A				R	F			
	2H-5	8.19	A	M								F							C														C	C				R	R			
	3H-CC	20.43	A	M								F							C														C	C				R	F			
	4H-CC	31.03	A	M								F							C														C	C				R	F			
	5H-CC	40.38	A	M								F							C														C	C				R	R			
NN19	6H-CC	49.78	A	M								F						F	C														C	C		F	F					
	7H-CC	59.48	A	M								F						F	C														C	C			F					
	8H-CC	68.88	B																																							
	9H-CC	78.37	B																																							
NN19	10H-CC	87.98	A	M								F						F	C														C	C		R	F					
	11H-CC	97.37	A	M								F						F	F														C	C	F							
	12X-CC	106.71	B																																							
NN18	13X-CC	113.09	A	M	A							C						F	F								C															
	14X-CC	122.7	A	M	A							F							F								C															
	15X-CC	132.42	B																																							
NN17	16X-CC	141.77	A	M	A														F								F				R	F										
NN15	17X-CC	151.19	A	M	A							F	C					R	F						A		F			F												
NN11	18X-CC	160.97	A	M	C								C						F						F	F	F	R	F	F												
NN8	19X-CC	170.73	A	M	F							F			C	F			F					F	C																	
	20X-CC	180.37	A	M	F							F	F		C	F	F		F					R	C																	
NN7	21X-CC	189.87	A	M	C	C			R			F			C				F	R	F		F																			
	22X-CC	198.65	A	M	C	F			R			F							F	R	F		F																			
	23X-CC	208.76	A	M	C	F			R			R			C				F	F	R		F																			
NN6	24X-CC	218.43	A	M		C	F	F	F			F							C		F	R																				
	25X-CC	228.27	A	M	C	C	C	F	F			C			C				C		F	R																				
	26X-CC	238	A	M	C	C	C		F			F			C				C		F	R																				
	27X-CC	247.56	A	M	C	C	C					C			C				C			R																				
	28X-CC	257.27	A	M	A	C	C					F	C		C		C		C			R																				
NN5	29X-CC	266.84	A	M		C	C	R	F			C		F	C				C		F																					
	30X-CC	274.15	A	M	A	C	F		R			F	C	C	C		C	F	C	R	R																					
	31X-CC	286.25	A	G	D	F	F					C	C	C	C		C	R	C	F																						
	32X-CC	296.14	A	G	A	C	C					C	A	C	A		C	F	F	F																						
	33X-CC	305.67	A	G	A	C	C					C	C	C	C			R																								
	34X-CC	315.36	A	G	A	C	C	C				C	R	C	F			R																								
	35X-CC	324.86	A	M	A	C	C	F				C		C	F			R																								
	36X-CC	334.62	A	G	A	C	F				R	C		C	F																											
	37X-CC	344.23	A	G	A	C	C	F	C			C	F	C	F	F																										
	38X-CC	353.85	A	G	A	C		C	F			F	F	C	C	F	F																									
	39X-CC	363.32	A	G	A	C	C	C	F			C	C	F	C	F	C																									
NN4	40X-CC	372.89	A	G	A	C	F	C	C	R	R	F	C	C	C																									

Notes: Abbreviations for abundances are as follows: A = abundant, C = common, F = few, R = rare, and B = barren. Abbreviations for preservation are as follows: G = good, M = moderate, and P = poor. For more specific definitions, refer to the "Explanatory Notes" chapter (this volume).

This table also appears on the volume CD-ROM.

CC have nannofossil assemblages that are assigned to Zone NN18. Nannofossils present in this interval exhibit moderate to good preservation and include *C. leptoporus*, small reticulofenestrids, *H. carteri*, and *P. discopora.* Sample 170-1039B-15X-CC is barren of nannofossils.

The late Pliocene Zone NN17 is observed in Sample 170-1039B-16X-CC with the LO of *Discoaster pentaradiatus* (2.46–2.56 Ma). Included in the well-preserved nannofossil assemblage of this sample are *D. brouweri, Ceratolithus rugosus, P. discopora, D. challengeri, D. asymmetricus,* and small reticulofenestrids.

Both the LO of *Sphenolithus* spp. (3.60 Ma) and the LO of *Reticulofenestra pseudoumbilica* (3.75 Ma) are observed in Sample 170-1039B-17X-CC, which places this sample in the early Pliocene Zone NN15. The LO of *Discoaster surculus,* which defines the base of Zone NN17 and the top of late Pliocene Zone NN16, was not encountered probably because of the wide sampling interval. The LO of *D. surculus* may be found between Samples 170-1039B-17X-CC and 16X-CC during much higher resolution shore-based analysis. Species present in Zone NN15 in this hole include well-preserved *Sphenolithus abies/neoabies, D. surculus, D. brouweri, D. pentaradiatus,* small reticulofenestrids, *P. discopora,* and *S. verensis.* Late Pliocene Zone NN16, early Pliocene Zones NN14 and NN13, and early Pliocene–latest Miocene Zone NN12 could not be resolved from the core-catcher sampling interval, and no hiatus or series of hiatuses is implied (Fig. 16). This section lies in an interval (2.5–12 Ma), with a linear sedimentation rate of ~6 m/m.y. (see below). This rate averages to ~250 k.y. per core section (1.5 m), or 1.5 m.y. per core. With a sampling interval of 9.6 m, it is clear how easily the shorter duration zones might be missed because of being sampled only from the core catchers.

The LO and first occurrence (FO) of *Discoaster quinqueramus* (5.6 and 8.6 Ma, respectively) define the top and bottom of late Miocene Zone NN11. *D. quinqueramus* is found in Sample 170-1039B-18X-CC only. Other species found in this sample include *D. brouweri, D. surculus, D. berggrenii, D. neorectus,* and *R. pseudoumbilica,* in moderate to good preservation.

The only sample containing *Discoaster hamatus* is Sample 170-1039B-19X-3, 125 cm. Because late Miocene Zone NN9 is defined as a range zone that is bound by the FO and LO of *D. hamatus* (9.4–10.7 Ma), Sample 170-1039B-19X-3, 125 cm, is assigned to Zone NN9. Included in the nannofossil assemblage are *Sphenolithus* spp., *D. surculus, D. challengeri, H. carteri,* and *Discoaster variabilis,* with all exhibiting moderate to good preservation.

Samples 170-1039B-19X-CC and 20X-CC do not contain *D. hamatus* or *D. kugleri* and are thus tentatively assigned to late Miocene Zone NN8. The nannofossil assemblage in these two samples includes *D. bellus, Sphenolithus* spp., *D. variabilis,* and *H. carteri. Catinaster coalitus* was not found in these samples.

Samples 170-1039B-21X-CC through 23X-CC contain *D. kugleri* (FO = 11.8 Ma, LO = 11.5 Ma) and are assigned to middle to late Miocene Zone NN7. *Coccolithus miopelagicus* is also observed in these samples for the first time while working downsection, indicating that even if the *D. kugleri* are reworked, this sample may not be younger than the LO of *C. miopelagicus* and is still assigned to Zone NN7. *Calcidiscus macintyrei, C. leptoporus, Discoaster exilis, Discoaster deflandrei,* and *H. carteri* are all observed in moderate to good preservation in this interval.

Samples 170-1039B-24X-CC through 28X-CC are assigned to middle Miocene Zone NN6, based on the absence of *D. kugleri* and *Sphenolithus heteromorphus.* Nannofossil species common in this interval are *Sphenolithus moriformis, C. miopelagicus, C. leptoporu*s, *H. carteri, D. adamanteus, Hayaster perplexus, Sphenolithus compactus, D. exilis, D. deflandrei, Coronocyclus nitiscens,* and *Cyclicargolithus floridanus.* All discoasters and most sphenoliths exhibit poor to moderate preservation. The placolith preservation is moderate to good.

The LO of *S. heteromorphus* (13.6 Ma) is found in Sample 170-1039B-29X-CC. Middle Miocene Zone NN5 is defined from the LO of *Helicosphaera ampliaperta* to the LO of *S. heteromorphus.* Thus, Samples 170-1039-29X-CC through 39X-CC are assigned to Zone NN5. Typical species found in these samples include *C. nitiscens, S. moriformis, H. carteri, C. leptoporus, D. deflandrei, C. floridanus, C. miopelagicus,* and *D. exilis.* As in Zone NN6, the discoasters and sphenoliths in Zone NN5 are poorly to moderately preserved, whereas the placolith preservation is moderate to good.

Early to middle Miocene Zone NN4 is recognized in Samples 170-1039B-40X-CC, 41X-2, 58 cm, and 41X-2, 108 cm, because of the presence of *H. ampliaperta* and absence of *Sphenolithus belemnos.* Zone NN4 is defined from the LO of *S. belemnos* (18.3 Ma) to the LO of *H. ampliaperta* (15.6 Ma). Species typical in this interval are the same as those found in the overlying Zone NN5, with the addition of *H. ampliaperta* (F–A). Discoasters are very poorly preserved, and placolith preservation is moderate.

Hole 1039C

Sample 170-1039C-1R-CC is assigned to middle Miocene Zone NN5, based on the presence of an assemblage of calcareous nannofossils comparable to the assemblage observed in nearby Hole 1039B, Samples 170-1039B-29X-CC through 39X-CC. From Samples 170-1039C-2R-CC through 7R-2, the added presence of *H. ampliaperta* indicates that these assemblages be assigned to Zone NN4. The calcareous nannofossils observed in this interval are also comparable to the assemblage seen in nearby Hole 1039B. Core 170-1039C-7R terminated in a pyroxene gabbro sill. Core 170-1039C-8R is composed of pyroxene gabbro with the exception of a 3-cm-thick sediment layer in Sample 170-1039C-8R-1, 8–11 cm. The sediment layer does not contain nannofossils.

Diatoms

Diatoms recovered from Site 1039 represent a nearly continuous stratigraphic record from the Holocene *Pseudoeunotia doliolus* Zone to the lower Miocene *Crucidenticula nicobarica* Zone (Table 7). Diatom abundance and preservation vary greatly from sample to sample with the largest changes occurring at the major lithologic unit boundaries. Diatoms in Unit U1 (diatomaceous ooze) are common to abundant, with moderate to good preservation. Rare to few amounts of reworked Pliocene and Miocene diatoms are present in Unit U1, particularly in the turbidites of Subunit U1A. Diatoms in Unit U2 (silty clay) are poorly preserved, are barren to few in abundance, and contain reworked taxa. In Unit U3 (siliceous nannofossil ooze), diatoms are common to abundant, and the preservation is good. The poor preservation of diatoms in Unit U2, combined with the slow sedimentation rates during the lower Pliocene and upper Miocene (see “Age-Depth Plots” section, this chapter), makes placement of the zonal boundaries tentative in parts of the section and prevents the placement of many subzonal boundaries (Fig. 16).

Diatoms from Hole 1039A, Samples 1H-CC through 3H-CC, are dominated by *P. doliolus, Thalassiosira oestrupii, Azpeitia nodulifer, Nitzschia marina,* and *Thalassionema nitzschiodes* (Table 7). This assemblage is characteristic of the *Pseudoeunotia doliolus* Zone of the late Pleistocene, which ranges in age from 0 to 0.62 Ma.

Diatoms from Hole 1039B, Samples 1H-CC through 8H-CC (lithologic Unit U1), are also characteristic of the late Pleistocene *P. doliolus* Zone and include common *P. doliolus, T. oestrupii, A. nodulifer, N. marina, T. nitzschiodes,* and *Hemidiscus cuneformis* (Table 7).

The LO of *Nitzschia reinholdii* occurs in Sample 170-1039B-9H-CC and marks both the 0.62-Ma datum and the top of the Pleistocene to late Pliocene *N. reinholdii* Zone (its rare occurrence in Sample 170-1039B-6H-CC is thought to be reworked). Samples 170-1039B-9H-CC and 10H-CC have common to few *T. oestrupii, T. nitzschiodes,* and *A. nodulifer.* These species, along with rare *P. doliolus, N. marina,* and *N. reinholdii*, support assignment to the *N. reinholdii* Zone, which spans 0.62–2.01 Ma. Samples 170-1039B-11H-CC and 12X-CC, respectively, show barren and rare diatom abundances which makes zonal assignment of these samples approximate. Extrapolated ages from the age-depth plot (Fig. 17) support placement of these samples in the *N. reinholdii* Zone.

Diatom assemblages from Sample 170-1039B-13X-CC lack *P. doliolus,* whose FO is 2.01 Ma; therefore this sample, which contains few to common *N. marina, N. fossilis, T. oestrupii,* and *A. nodulifer*, correlates to the late Pliocene *N. marina* Zone (2.01–2.78 Ma). Diatom abundance and preservation continues to deteriorate in the samples of Unit U2 from few with poor to moderate preservation in Sample 170-1039B-13X-CC, to rare with poor preservation in Sample 170-1039B-14X-CC, and to barren in Samples 170-1039B-15X-CC and 16X-CC. Extrapolation from the age-depth plot (Fig. 17) suggests that Samples 170-1039B-14X-CC through 16X-CC are within the *N. marina* Zone and are between 2.01 and 2.78 Ma. Diatom flora are few in Sample 170-1039B-17X-CC and are only poorly preserved, but include *N. marina, N. reinholdii, Rhizosolenia praebergonii* var. *robusta,* and *A. nodulifer*. Extrapolation from the age-depth plot places this sample in the *Nitzschia jouseana* Zone, which is between 2.78 and 5.18 Ma.

Diatom abundance increases, and the preservation improves in Samples 170-1039B-18X-CC and 19X-CC, which are part of lithologic Unit U3. Sample 170-1039B-18X-CC contains abundant *Thalassiothrix longissima* and few to rare amounts of *Nitzschia miocenica, N. marina, N. reinholdii, T. oestrupii, A. nodulifer,* and *H. cuniformis.* The LO of *N. miocenica* is 6.07 Ma and marks the *Thalassiosira convexa* Subzone C/B boundary of the latest Miocene. Sample 170-1039B-19X-CC contains an assemblage very similar to that of Sample 170-1039B-18X-CC, but it also contains *Rossiella paleacea,* whose LO is 7.37 Ma, which places this sample in *N. porteri* Subzone B of the late Miocene. The apparent absence of *T. convexa* Subzone C between Samples 170-1039B-18X-CC and 19X-CC is likely related to the low age-depth rates during this time (see “Age-Depth Plots” section, this chapter) and our low sampling resolution. Higher resolution analysis of the diatom subzonal boundaries will be a priority during the post-cruise research.

Table 7. Diatom range distribution chart for Site 1039.

Diatom zone	Hole, core, section	Depth (mbsf)	Abundance	Preservation	*Actinocyclus ellipticus*	*Actinocyclus ellipticus* f. *lanceolata*	*Actinocyclus ellipticus* var. *javanica*	*Actinocyclus ingens*	*Actinocyclus moronensis*	*Actinoptychus minutus*	*Actinoptychus senarius*	*Annellus californicus*	*Asterolampra acutiloba*	*Asteromphalus elegans*	*Azpeitia nodulifer*	*Cavitatus jouseanus*	*Cestodiscus peplum*	*Cestodiscus pulchellus*	*Cestodiscus pulchellus* var. *maculatus*	*Coscinodiscus gigas* var. *diorama*	*Coscinodiscus lewisianus*	*Coscinodiscus lewisianus* var. *similis*	*Coscinodiscus marginatus*	*Coscinodiscus temperei* var. *delicata*	*Craspedodiscus coscinodiscus*	*Crucidenticula nicobarica*	*Denticulopsis hustedtii*	*Hemidiscus cuneiformis*	*Nitzschia fossilis*	*Nitzschia marina*	*Nitzschia miocenica*	*Nitzschia reinholdii*	*Pseudoeunotia doliolus*	*Raphidodiscus marylandicus*	*Rhizosolenia praebergonii*	*Rhizosolenia praebergonii* var. *robusta*	*Rossiella paleacea*	*Thalassionema nitzschioides*	*Thalassiosira oestrupii*	*Thalassiosira plicata*	*Thalassiosira tappanae*	*Thalassiosira yabei*	*Thalassiothrix longissima*	*Triceratium pileus*
	170-1039A-																																											
	1H-CC	8.75	A	G						F	R				F													F		F			C			r		C	C				C	r
	2H-7	18.5	A	G							R		R	R	C								F					R		F			C			r			C					r
	2H-CC	18.66	A	G						R	R			F	F															F			C			r		C	C				C	
	3H-CC	28.42	A	G							R		R	R	C								F					R	r	R			C			r		C	C				C	r
	170-1039B-																																										
P. doliolus	1H-CC	1.9	C	M					r		R		F	F	C								R							F			F		P			F	C				F	
	2H-5	8.19	A	G							R				C													F		F			C					C	F				F	
	3H-CC	20.43	A	M						F	F		F	F	C											r		F		F			F			r		F	C				R	r
	4H-CC	31.03	C	M											F													R	R	F			C			r			F					r
	5H-CC	40.38	A	G							R				F															C			C						C					
	6H-CC	49.78	A	G											R													R		F		R						C	C					
	7H-CC	59.48	A	M									R	R	F														R	F			F			r		C	F					r
	8H-CC	68.88	F	M										R	F														R	R									F					
	9H-CC	78.37	C	M							R				F														R	R		R	R			r		F	F					r
N. reinholdii	10H-CC	87.98	F	P											F													R	R	R		R	R					F	F				F	
	11H-CC	97.37	B																																									
	12X-CC	106.71	R	P																																		R					R	
	13X-CC	113.09	F	M							F		R	R	F													F	F	P		R				R			F				R	
N. marina	14X-CC	122.7	F	P																										P		R												
	15X-CC	132.42	B																																									
	16X-CC	141.77	B																																									
N. jouseanus	17X-CC	151.19	C	M	r				r						F															R		F				R								r
T. convexa	18X-CC	160.97	A	M							R				R								R					R		R	R	R						A	R				A	r
N. porteri	19X-CC	170.73	A	M																	r										R						R	C					C	
T. yabei	20X-CC	180.37	A	G							R																F	R										C				F	C	
Cr. coscinodiscus	21X-CC	189.87	A	G										R							F				R		F										F					F	A	r
C. gigas v. *diorama*	22X-CC	198.65	A	G			R																	R			F										F	C				F	C	
	23X-CC	208.76	A	G																	F				C		C										F	C				F	A	
	24X-CC	218.43	A	G					F							F				R	F	F					C										F	C				R	A	
	25X-CC	228.27	A	M											R						F				F	F	C										F	C		F			A	
C. lewisianus	26X-CC	238	A	M				F													F				F	C	F											C					C	
	27X-CC	247.56	A	M														R							F	A	F										R	C					C	
	28X-CC	257.27	A	G		R		F								R					F	F			R	R	C										R	C			C		A	
	29X-CC	266.84	A	M																	C					C	C											C					A	
	30X-CC	274.15	A	G			R	R									R	F			C				F	C	C											C	F		F		A	
	31X-CC	286.25	A	M				F	R				R		F		R	F			F		F			C															F		C	r
	32X-CC	296.14	A	M				F								F	R	C			F		F		F	C											F	F					A	
	33X-CC	305.67	A	M				C									F						C		F	F											F	F			F		C	
	34X-CC	315.36	A	G				F								F	R	F			R		C		F	F											R	C					A	
C. peplum sz B	35X-CC	324.86	A	M				F						R		F	R	F					F		R	F											R	F					C	
	36X-CC	334.62	A	M												F	F	F					F			F											R	F					C	
	37X-CC	344.23	A	G				C								C	R	F			C		F														C	F					A	
	38X-CC	353.85	A	M				C			R		R			F		C			F		F		R	R											F	F			R		C	
	39X-CC	363.32	A	M												F	R	A					F			C												F					C	
	40X-CC	372.89	A	M								R				C	R	C	C		F					R											F	C					A	
C. peplum sz A	41X-CC		B																																									

Table 7 (continued).

Diatom zone	Hole, core, section	Depth (mbsf)	Abundance	Preservation	*Actinocyclus ellipticus*	*Actinocyclus ellipticus* f. *lanceolata*	*Actinocyclus ellipticus* var. *javanica*	*Actinocyclus ingens*	*Actinocyclus moronensis*	*Actinoptychus minutus*	*Actinoptychus senarius*	*Annellus californicus*	*Asterolampra acutiloba*	*Asteromphalus elegans*	*Azpeitia nodulifer*	*Cavitatus jouseanus*	*Cestodiscus peplum*	*Cestodiscus pulchellus*	*Cestodiscus pulchellus* var. *maculatus*	*Coscinodiscus gigas* var. *diorama*	*Coscinodiscus lewisianus*	*Coscinodiscus lewisianus* var. *similis*	*Coscinodiscus marginatus*	*Coscinodiscus temperei* var. *delicata*	*Craspedodiscus coscinodiscus*	*Crucidenticula nicobarica*	*Denticulopsis hustedtii*	*Hemidiscus cuneiformis*	*Nitzschia fossilis*	*Nitzschia marina*	*Nitzschia miocenica*	*Nitzschia reinholdii*	*Pseudeunotia doliolus*	*Raphidodiscus marylandicus*	*Rhizosolenia praebergonii*	*Rhizosolenia praebergonii* var. *robusta*	*Rossiella paleacea*	*Thalassionema nitzschioides*	*Thalassiosira oestrupii*	*Thalassiosira plicata*	*Thalassiosira tappanae*	*Thalassiosira yabei*	*Thalassiothrix longissima*	*Triceratium pileus*
	170-1039C-																																											
C. peplum sz A	1R-4	366.92	A	M				F			R	R		R	F	F	F	F			R		C			F											F				R		A	
	2R-CC	375.85	A	M				F			R	F				C	F				F		F			F											F	F					C	
	3R-CC	386.39	A	M								R		R		C	F				F		F			F											F						C	
	4R-CC	393.6	C	M				R			R	R				C		C			F		F		R	F											F	F					C	
C. nicobarica	5R-CC	403.06	C	P								R				R		C			F		F			F									R		R						F	
	6R-CC	417.28	A	M									R	R		F		C			F		C		F	F											F	F					C	
	7R-1	421.32	A	P								F	F	F		F		C			F		C		R	R											F	F					C	

Notes: Abbreviations for abundances are as follows: A = abundant, C = common, F = few, R = rare, B = barren, and lowercase letters = reworked. Abbreviations for preservation are as follows: G = good, M = moderate, and P = poor. For more specific definitions, refer to the "Explanatory Notes" chapter (this volume). Sz = subzone.

This table also appears on the volume CD-ROM.

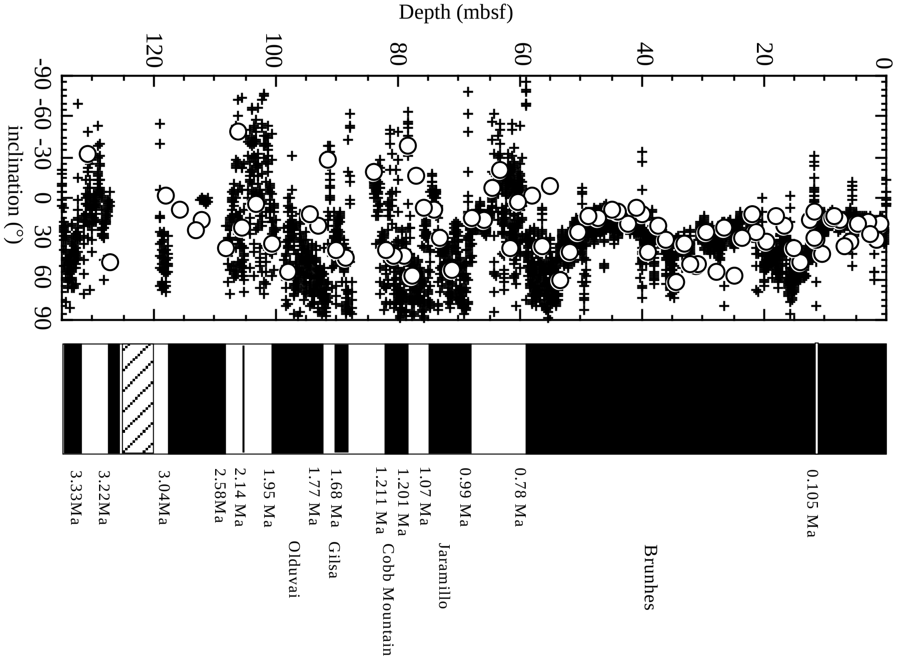

Figure 17. Inclinations of remanence after 20-mT demagnetization of split cores from Hole 1039B, 0–133 mbsf (crosses), and from discrete samples (circles). The interpreted magnetostratigraphy, with reversal ages from Berggren et al. (1995a) is shown on the right.

Sample 170-1039B-20X-CC has abundant diatoms that show moderate to good preservation. Broken frustules of *T. longissima*, *Denticulopsis hustedtii*, and *Thalassiosira yabei* are common; *H. cuneiformis* is also present in small amounts. The LO of *T. yabei* is 8.17 Ma, suggesting that this sample corresponds to the top of the late Miocene *T. yabei* Zone. The apparent absence of the late Miocene *N. miocenica* Subzone A and the entire *N. porteri* Zone between core-catcher samples is related to the low sedimentation rate and to the low sampling resolution as discussed previously. Similarly, the A Subzone of the *T. yabei* Zone and the *Actinocyclus moronensis* Zone have not yet been resolved between Samples 170-1039B-20X-CC and 21X-CC.

Samples 170-1039B-21X-CC and 22X-CC span the late middle Miocene *Craspedodiscus coscinodiscus* Zone, which is marked by the LO of *C. coscinodiscus* (11.34 Ma) and occurs in Sample 21X-CC, to the FO of *C. temperi* var. *delicata* (12.06 Ma), which occurs in Sample 22X-CC and marks the upper boundary of the *Coscinodiscus gigas* var. *diorama* Zone. Both of these samples have abundant *T. longissima*, and few *Rossiella paleacea*, *T. yabei*, *D. hustedtii*, and *Asteromphalus elegans*.

Samples 170-1039B-23X-CC through 30X-CC all have abundant diatoms that show good preservation and correspond to the middle Miocene interval of lithologic Subunit U3B (Fig. 16), which has a relatively high age-depth rate. The assemblages are characterized by abundant *T. longissima*, common *Coscinodiscus lewisianus*, *D. hust-*

Table 8. Planktonic foraminifer range distribution chart for Site 1039.

Planktonic foraminifers zone	Hole, core, section	Depth (mbsf)	Abundance	Preservation	*Catapsydrz stainforthi*	*Dentoglobigerina altispira*	*Dentoglobigerina globosa*	*Fohsella fohsi sensu stricto*	*Fohsella peripheroacuta*	*Fohsella peripheronda*	*Globigerina nepenthes*	*Globigerina bulloides*	*Globiferina umbilicata*	*Globigerinatella insueta*	*Globigerinella aequilateralis*	*Globigerinella calida*	*Globigerinoides altiapertura*	*Globigerinoides conglobatus*	*Globigerinoides diminutus*	*Globigerinoides extremus*	*Globigerinoides immaturus*	*Globigerinoides mitrus*	*Globigerinoides obliquus*	*Globigerinoides parawoodi*	*Globigerinoides quadrilobatus*	*Globigerinoides ruber*	*Globigerinoides sacculifer*	*Globigerinoides sicanus*	*Globigerinoides subquadratus*	*Globigerinoides trilobus*	*Globoquadrina baroemoenensis*	*Globoquadrina dehiscens*	*Globoquadrina venzuelana*	*Globorotalia archeomenardii*
	170-1039A-																																	
N23	1H-CC	8.75	R	M											R	R										R								
	2H-CC	18.66	C	M											R											R	R							
	3H-CC	28.42	R	M									R													R	R							
	170-1039B-																																	
	1H-CC	1.9	C	M								R			R	R										R	R							
	3H-CC	20.43	R	G											R											R	R							
	4H-CC	31.03	C	G																						R	R							
	5H-CC	40.38	C	G																						R	R							
	6H-CC	49.78	C	G																														
	7H-CC	59.48	C	M														R			R					R	R							
N22	8H-CC	68.88	R	M											R																			
	9H-CC	78.37	R	M																						R	R							
	10H-CC	87.98	R	G																						R	R							
	11H-CC	97.37	T	M																														
	12X-CC	106.71	B																															
	13X-CC	113.09	R	M																			R			R	R							
	14X-CC	122.7	R	G																R			R											
	15X-CC	132.42	B																															
	16X-CC	141.77	B																															
N19	17X-CC	151.19	R	M		R					R																							
N17	18X-CC	160.97	R	M		R																												
	19X-CC	170.73	R	G		R														R													R	
	20X-CC	180.37	B																															
	21X-CC	189.87	C	M		F	R																											
N14	22X-CC	198.65	R	M		R					R																					R		
N12	23X-CC	208.76	C	G																														
N11	24X-CC	218.43	C	M				F																										
	25X-CC	228.27	C	M		F		F																	R				R			R	F	
	26X-CC	238	C	M		F		F																			R					R	F	
N10	27X-CC	247.56	C	G		F	R		R	F												R										R	F	
N9	28X-CC	257.27	C	G		F	R																R						R			R	F	
	29X-CC	266.84	C	G		F	R																R				F			R		R	F	
N8	30X-CC	274.15	R	G		R	R														R		R				R					R	F	R
	31X-CC	286.25	C	G		R								R							R				R							F	R	
	32X-CC	296.14	C	G		R	R																						R	R	R	F	F	
	33X-CC	305.67	C	M		R	R																R				R		R			R	R	
	34X-CC	315.36	C	M		R	R							R													R	R	R			R	R	
	35X-CC	324.86	A	G		R								R					R		R		R		R		R	R				R		
	36X-CC	334.62	R	M		R													R									R				R	R	
	37X-CC	344.23	R	M		R																					R	R	R	R	R	R		
	38X-CC	353.85	R	G		R													R													R	F	
	39X-CC	363.32	R	M		F																						R				R		
	40X-CC	372.89	R	M						R																					R	R		
	41X-CC	378.15	B																															
	170-1039C-																																	
	1R-4	366.92	A	G		F																					F	R	R	F		R	F	
	2R-CC	375.85	R	M													R				R				R				R					
	3R-CC	386.39	C	G		F																						R			R	R	F	
	4R-CC	393.6	R	G		R				R				R			R		R		R			R				R	R	R				
	5R-CC	403.06	C	M		F																									R	R		
	6R-CC	417.28	C	M	R	R																										R	R	

Notes: Abbreviations for abundances are as follows: A = abundant, C = common, F = few, R = rare, B = barren, and lowercase letters = reworked. Abbreviations for preservation are as follows: G = good, M = moderate, and P = poor. For more specific definitions, refer to the "Explanatory Notes" chapter (this volume).

This table also appears on the volume CD-ROM.

edtii, and *C. coscinodiscus. T. longissima* is particularly abundant in Samples 170-1039B-28X-CC through 30X-CC. This abundance distribution likely corresponds to the laminated diatom oozes (LDO) identified during Leg 138 as monospecific *T. longissima* assemblages (Kemp et al., 1995). The LO of *C. lewisianus* occurs in Sample 23X-CC, which corresponds to the top of the *C. lewisianus* Zone and an age of 12.86 Ma. The base of the zone occurs in Sample 170-1039B-30X-CC and is marked by the LO of *Cestodiscus peplum* at an age of 14.03 Ma.

The middle Miocene *C. peplum* Subzone B (14.03–15.00 Ma) occurs in Samples 170-1039B-30X-CC through 39X-CC, which contain common *C. peplum, C. pulchellus, Actinocyclus ingens,* and *Crucidenticula nicobarica,* in addition to *T. longissima*. The *C. peplum* Subzone A/B boundary is recognized by the LO of *Annellus californicus* in Sample 170-1039B-40X-CC at an age of 15.00 Ma. Sample 170-1039B-41X-CC is barren of diatoms.

Samples 170-1039C-1R-CC through 3R-CC have abundant to common diatom assemblages that are typical of the early middle Miocene *C. peplum* Subzone A and contain *C. peplum, A. californicus,* and *A. ingens* (Table 7). The boundary with the *Crucidenticula nicobarica* Zone is marked by the FO of *C. peplum,* which occurs in Sample 170-1039C-3R-CC at an age of 16.4 Ma. Samples 170-1039C-4R-CC through 7R-CC contain common *C. nicobarica, A. ingens, C. pulchellus,* and *Synedra jouseana* and correspond to the ear-

Table 8 (continued).

Planktonic foraminifers zone	Hole, core, section	Depth (mbsf)	Abundance	Preservation	*Globorotalia birnageae*	*Globorotalia fohsi lobata*	*Globorotalia hirsuta*	*Globorotalia juani*	*Globorotalia menardii*	*Globorotalia merotumida*	*Globorotalia peripheroronda*	*Globorotalia praescitula*	*Globorotalia scitula*	*Globorotalia siakensis*	*Globorotalia theyeri*	*Globorotalia tosaensis*	*Globorotalia tumida*	*Globorotalia ungulata*	*Globorotaloides hexagona*	*Jenkinsella bella*	*Neogloboquadrina acostaensis*	*Neogloboquadrina dutertrei*	*Neogloboquadrina humerosa*	*Neogloboquadrina mayeri*	*Orbulina bilobata*	*Orbulina suturalis*	*Orbulina universa*	*Praeorbulina circularis*	*Pulleniatina obliquiloculata*	*Sphaeroidinella dehiscens*	*Sphaeroidinellopsis seminulina*	*Zeaglobigerina decoraperta*	*Zeaglobigerina druryi*	*Zeaglobigerina woodi*
N23	170-1039A-																																	
	1H-CC	8.75	R	M					R									R	R			R												
	2H-CC	18.66	C	M					R								R	R				R					R		R					
	3H-CC	28.42	R	M					R				R					R				R							R					
	170-1039B-																																	
	1H-CC	1.9	C	M					R								R	R	R			R							R					
	3H-CC	20.43	R	G					R						R			R	R															
	4H-CC	31.03	C	G													R	R				R			R				R					
	5H-CC	40.38	C	G					R								R		R			R							R					
	6H-CC	49.78	C	G			R		R								R					F	F						R					
	7H-CC	59.48	C	M					R				R				R	R				R								R				
N22	8H-CC	68.88	R	M					R							T	R	R				F	F						R					
	9H-CC	78.37	R	M					R				R									R							R					
	10H-CC	87.98	R	G					R													R							R					
	11H-CC	97.37	T	M					P													T												
	12X-CC	106.71	B																															
	13X-CC	113.09	R	M												R	R		R			R							R	R				
	14X-CC	122.7	R	G																									R	R				
	15X-CC	132.42	B																															
	16X-CC	141.77	B																															
N19	17X-CC	151.19	R	M																	R									R	R			
N17	18X-CC	160.97	R	M				R	R	R																								
	19X-CC	170.73	R	G																														
	20X-CC	180.37	B																															
	21X-CC	189.87	C	M																			R								R			
N14	22X-CC	198.65	R	M										R										R										R
N12	23X-CC	208.76	C	G		F								R												R						R		
N11	24X-CC	218.43	C	M										F										F							R			
	25X-CC	228.27	C	M										R										F							R			
	26X-CC	238	C	M								R		F										F							R			
N10	27X-CC	247.56	C	G																							R				R			
N9	28X-CC	257.27	C	G							F															R	R							
	29X-CC	266.84	C	G							F			R										F		R					R			
N8	30X-CC	274.15	R	G							F													R									R	
	31X-CC	286.25	C	G							F													R							R		R	
	32X-CC	296.14	C	G										R										R										
	33X-CC	305.67	C	M										R										R										
	34X-CC	315.36	C	M										R										R				R			R			
	35X-CC	324.86	A	G										R										R							R			
	36X-CC	334.62	R	M										R										R										
	37X-CC	344.23	R	M										R										R										
	38X-CC	353.85	R	G																														
	39X-CC	363.32	R	M							F			R										R										
	40X-CC	372.89	R	M	R									R						R														
	41X-CC	378.15	B																															
	170-1039C-																																	
	1R-4	366.92	A	G	F						F	T		F						R				F										
	2R-CC	375.85	R	M										R										R										
	3R-CC	386.39	C	G	R							R		F										F										
	4R-CC	393.6	R	G	R																													
	5R-CC	403.06	C	M	R						F			F						R				F										
	6R-CC	417.28	C	M							F	R		F										F										

ly middle Miocene *C. nicobarica* Zone. The presence of the LO of *Raphidodiscus marylandicus* in Sample 170-1039C-5R-CC at an age of 16.49 Ma confirms the assignment to the uppermost part of the *C. nicobarica* Zone.

Planktonic Foraminifers

Planktonic foraminifers in samples at Site 1039 range in age from the Pleistocene to the earliest part of the middle Miocene. The distribution and range of foraminifers from Hole 1039A is presented in Table 8. Planktonic foraminifers are present in all samples except Samples 170-1039B-12X-CC, 15X-CC, 16X-CC, 20X-CC, and 41X-CC (Table 8).

Planktonic foraminiferal zonation was not established in the upper part of Hole 1039B, from Samples 170-1039B-1H-CC through 21X-CC, because of the absence of zonal marker species. However, zonal intervals were identified by the presence of some age-diagnostic species. In the lower part of the sequence, middle Miocene assemblages are dominant, and some zonal marker species are present.

In the upper part of Hole 1039B, from Sample 170-1039B-1H-CC through 8H-CC, the assemblages yielded *Globigerinoides ruber*, *Globigerinoides sacculifer*, *Globorotalia menardii*, *Globorotalia tumida*, *Globorotalia ungulata*, *Neogloboquadrina dutertrei*, and very rare *Pulleniatina obliquiloculata* (dextrally coiling in Samples 170-1039-1H-CC through 6H-CC, and sinistrally coiling in Sample 170-1039B-8H-CC). The FO of *Globorotalia hirsuta* is recognized in Sample 170-1039B-6H-CC, which indicates an age of 0.47 Ma.

In Samples 170-1039B-9H-CC through 16H-CC, planktonic foraminifers are very rare or absent. The rare assemblages consists of *G. ruber*, *G. sacculifer*, *N. dutertrei*, *Neogloboquadrina humerosa*, *Orbulina universa*, and *P. obliquiloculata* (sinistrally coiling in Samples 170-1039B-8H-CC through 13X-CC, and dextrally coiling in

Sample 170-1039B-14X-CC). The LO of *Globigerinoides extremus* is recognized in Sample 170-1039B-14X-CC, which indicates an age of 1.77 Ma. In Sample 170-1039B-17X-CC, the assemblage contains *G. extremus, G. ruber, G. sacculifer, Neogloboquadrina acostaensis, O. universa, Globoquadrina altispira,* and *Sphaeroidinella dehiscens.* The sample was assigned to Zone N19, based on the occurrence of *S. dehiscens* and *Globigerina nepenthes.* In Samples 170-1039B-18X-CC through 20X-CC, the assemblage yielded *Globorotalia menardii, Dentoglobigerina altispira,* and *Globigerinoides obliquus.* The samples were assigned to Zone N17, based on occurrence of *Globorotalia juanai, N. humerosa,* and *G. extremus.*

Middle Miocene assemblages are dominated by *D. altispira, Globoquadrina venezuelana, Neogloboquadrina mayeri, Globorotalia peripheroronda, Globorotalia siakensis,* and *Globigerinoides subquadratus.*

Sample 170-1039B-22X-CC was assigned to Zone N14 on the basis of the co-occurrence of *N. mayeri* and *G. nepenthes.* Zone N13 was not identified. Sample 170-1039B-23X-CC was assigned to Zone N12 on the basis of FO of *Globorotalia foshi lobata.* The interval from Samples 170-1039B-24X-CC through 26X-CC was assigned to Zone N11, between the first and last occurrences of *Globorotalia foshi foshi* in Samples 24X-CC and 26X-CC. Sample 170-1039B-27X-CC was assigned to Zone N10 on the basis of the co-occurrence of *Globorotalia peripheroronda* and *Globorotalia peripheroacuta.* The interval from Samples 170-1039B-28X-CC through 29X-CC was assigned to Zone N9 on the basis of the FO of *Orbulina suturalis* in Sample 29X-CC. The interval from Samples 170-1039B-30X-CC through 170-1039C-6R-CC was assigned to Zone N8, between the FO of *O. suturalis* in Sample 170-1039B-29X-CC and the FO of *Globigerinoides sicanus* in Sample 170-1039C-6R-CC. Sample 170-1039C-7R-1, 85−100 cm, was assigned to Zone N7 based on the absence of *G. sicanus.*

Hole 1039C comprises cores that were obtained to overlap the lower part of Hole 1039B. Samples 170-1039C-1R-CC through 6R-CC yield abundant to common middle Miocene planktonic foraminifers that are well preserved.

Paleomagnetism

Sediments

Demagnetization of natural remanence in both split cores and discrete samples was successful in defining portions of the magnetostratigraphy at Site 1039, despite complications posed by poor-quality APC and XCB cores. The ubiquitous, steeply inclined drilling-related overprint of the natural remanent magnetization (NRM) found in most ODP cores was removed in these sediments by an alternating field of 2−10 mT. Two intervals within core from Hole 1039B contain relatively well-defined sequences of magnetic field reversals. The uppermost sequence, from 0 to 132 mbsf, has reversals ranging in age from the Blake Event (0.105 Ma) to the termination of Chron C2An.3n (3.33 Ma; Fig. 17A). The lower sequence of well-defined reversals extends from 302 to 378 mbsf, spanning Chrons C5Ar.1n (12.678 Ma) through C5Cn.2n (16.488 Ma; Fig. 17B). Identification of reversals between 302 and 132 mbsf has thus far been unsuccessful. A large interval of predominantly normal polarity, coinciding with a zone of increased intensity of remanence from 120 to 180 mbsf (Fig. 18), occurs within sediments ranging in age from 3.5 to 8.2 Ma. During this period of time, 13 major changes in magnetic field polarity should be observed; the lack of these reversals in the split-core record from Hole 1039B suggests either a remagnetization event related to diagenesis within this interval or contamination by a drilling-related overprint. Resolution of the magnetostratigraphy within this interval will await detailed study of discrete samples.

Remanence intensity corresponds well with the observed lithostratigraphic units and sediment physical properties (compare Fig. 1 with Fig. 19). High NRM intensities occur within Unit U1 and rapidly drop off at the base of Subunit U1A. A sharp drop in intensity marks the change from Subunits U3A to U3B at 180 mbsf, and an NRM increase occurs just above the gradational contact between Subunits U3B and U3C (350 mbsf). The pattern of NRM intensity variations is very similar to that of the whole-core magnetic susceptibility records for this site (Fig. 1).

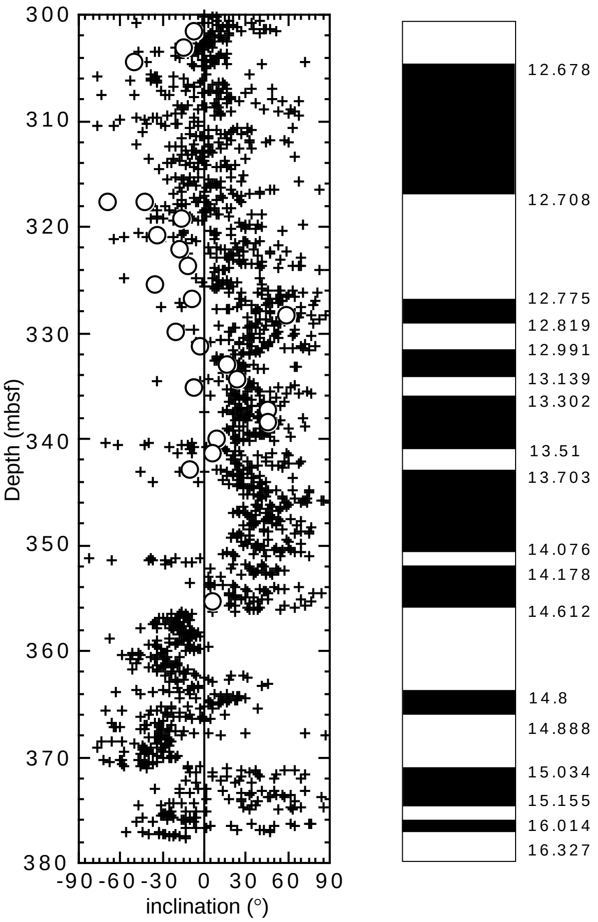

Figure 18. Inclinations of remanence after 20-mT demagnetization of split cores from Hole 1039B, 300−380 mbsf (crosses), and from discrete samples (circles). The interpreted magnetostratigraphy, with reversal ages from Berggren et al. (1995a) is shown on the right.

Gabbro Intrusions

Demagnetization of the gabbro intrusions from the lower portions of Hole 1039B and 1039C revealed that these intrusions have highly variable magnetic inclinations, even within long (30−60 cm) intact portions of core (Fig. 20). The variable inclinations display apparent polarity reversals, although a corresponding (and expected) change in declinations across these reversals is not observed. To account for this odd behavior, a magnetic viscosity test of a minicore was performed by placing an undemagnetized sample in the low (<0.3 G) magnetic field within the pass-through magnetometer, and monitoring the change in NRM with time. Large changes, particularly in the Z (vertical) magnetization component were observed over a time span of several minutes, suggesting that the variation in inclinations observed for these gabbros is caused by unstable magnetic behavior. Examination of thin sections under reflecting light confirms that there is an abundance of large (>100 µm) multidomain magnetite grains within these rocks. The gabbro from Hole 1039B displayed more stable behavior and yielded a normal polarity direction. The inclination of the Hole 1039B gabbro was 10°, which, assuming the in-

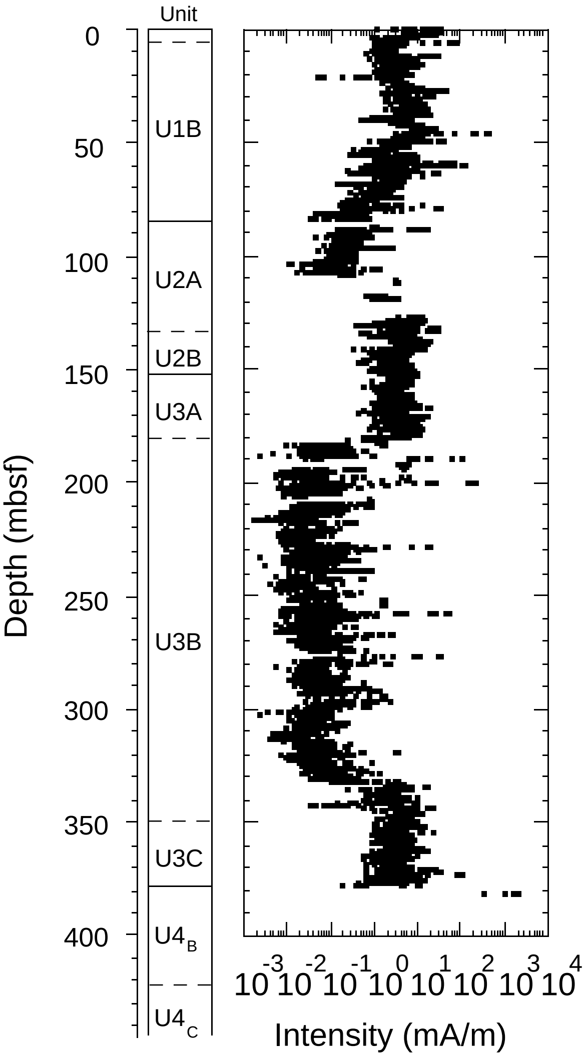

Figure 19. Intensity (mA/m) of remanence after 20-mT demagnetization from Hole 1039B, with lithostratigraphic units for comparison.

trusion was horizontal, indicates it was cooled at a paleolatitude of 5°N.

Age-Depth Plots

Two age-depth plots are presented. One plot is based on biostratigraphic datums, and the other is based on magnetostratigraphy (datums are shown in Table 9). Combining the two stratigraphies into a single age-depth curve results in several contradictions. Therefore, we choose to present both age-depth plots for comparison (Fig. 21; see also Fig. 1). It is likely that the contradictions between the two curves will be reconciled with higher resolution paleontologic analysis and further magnetostratigraphic analysis during shore-based study.

A complete or nearly complete late Pleistocene through middle Miocene (~16.49 Ma) section cored at Site 1039 is recognized in the combined last and/or first occurrence datums of the diatom, foraminifer, and calcareous nannofossil record (Table 9). A linear age-depth plot calculated from the combined index microfossil datums (Fig. 21) indicates age-depth rates that approximate 46 m/m.y. for the Pleistocene (50–120 mbsf), 6 m/m.y. for the Pliocene and upper Miocene interval (120–200 mbsf), and 47 m/m.y. in the middle Miocene interval (200–448 mbsf).

Using the magnetostratigraphic age-depth relationship as outlined above, age-depth rates for Site 1039 can be estimated (Fig. 21). For Subunit U1A from 0 to 18.7 mbsf, rates are 95 m/m.y., and from 18.7 to 133 mbsf, age-depth rates are 30 m/m.y. Within Unit U3, age-depth rates average 20 m/m.y. from 305 to 370 mbsf, and decrease to 5 m/m.y. from 370 to 380 mbsf.

More detailed age-depth rate curves are shown in Figure 1. These curves are generated by fitting a smoothed curve to the biostratigraphic and paleomagnetic data (see "Explanatory Notes" chapter, this volume, for a description of the procedure).

GEOCHEMISTRY

Overview of Results

The main objectives for thoroughly documenting the chemistry of the pore fluids and solids of Site 1039 are (1) to identify the distribution of key elements and isotope ratios between the pore fluids and various solid phases, (2) to quantify the fluxes of these key elements and isotopes into the subduction zone, and (3) to utilize these data for evaluating geochemical and material mass balances, as well as for constraining the importance of underplating.

Pore waters were squeezed from whole-round cores that were 5–35 cm long and were analyzed for salinity, Cl, Ca, Mg, K, Si, pH, alkalinity, sulfate, ammonium, and phosphate concentrations. Sodium concentrations were determined from the above data by charge-balance calculations. The sediments were analyzed for sulfur and total and inorganic carbon (IC) contents, and the difference between the latter two is reported as the total organic carbon (TOC). A representative suite of bulk sediments and gabbros was analyzed by XRF for major and select minor and trace element concentrations.

The depth profiles of pore-water concentration reflect the three main sediment lithologic units (see "Lithostratigraphy" section, this chapter). In the hemipelagic organic matter–rich Unit U1 with 0.6–1.9 wt% TOC, and also in the less biogenic silty clay Unit U2 with 0.4–0.6 wt% TOC, the pore-water chemical characteristics are dominated by bacterially mediated organic matter diagenesis as well as dissolution of diatoms, and to lesser extents volcanic ash alteration and clay ion-exchange reactions. The sediment total sulfur (TS) distribution with depth is also determined primarily by the same organic matter bacterially mediated reactions. TS is therefore present only in Units U1 and U2 with concentrations of 0.1–2.2 wt%, mostly as pyrite. The pyrite, and also most likely formation of diagenetic and/or bacterial magnetite, should affect the iron concentration of the two hemipelagic sediment units. Methane (C_1) concentrations are low, because sulfate reduction is incomplete even in the organic matter–rich hemipelagic section of the sediment sequence. In the pelagic calcareous and siliceous oozes with ash layers (Unit U3) having low (mostly <0.3 wt%) TOC content, the pore-water chemistry is dominated by diatom dissolution, ash alteration, and, to a lesser extent, carbonate recrystallization reactions. In the basal sediment Subunit U3C, mixing with metalliferous components is clearly reflected in both the pore-water and sediment chemistries; particularly elevated concentrations of Mn in the pore waters and of other transition metals (Ni, Cu, and Zn) in the sediments have been determined. Except for a fluid conduit at 95–130 mbsf, the pore-water chemical depth profiles do not support vertical or horizontal fluid advection within the sediment section; instead, they are controlled by diagenesis plus diffusion. In the basal section, however, the pore-water concentration profiles of Cl, K, Si, and especially of Ca and Mg, suggest seawater flow in the upper oceanic basement. Such a flow regime is most plausibly responsible for the extremely low geothermal gradient at this site.

XRF geochemistry shows the following:

1. Ashes above 300 mbsf have trace element signatures indicating derivation from a volcanic arc, whereas those from below

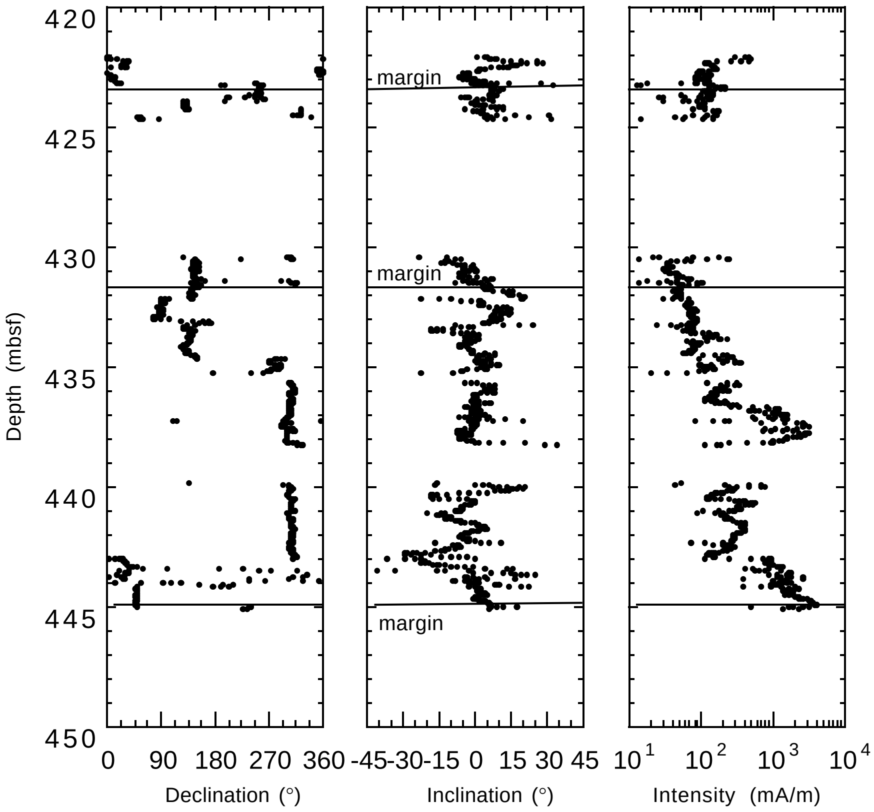

Figure 20. Declination, inclination, and intensity of remanence from split cores of the gabbro from Hole 1039C.

330 mbsf were probably derived from mantle similar to that of the Galapagos.

2. Gabbros are chemically homogeneous and similar to Galapagos lavas rather than East Pacific Rise basalts.
3. For recycling purposes, the sediment column entering the trench off Costa Rica is enriched in K and depleted in Ba and Sr, relative to that subducting beneath Guatemala.

Methods

The results of headspace gas analyses are reported in Table 10. K, Ca, and Mg concentrations were determined by two methods, as described in the “Explanatory Notes” chapter (this volume). The results of the more accurate and precise methods, atomic absorption for K and titrations for Ca and Mg, are reported in Table 11. Two 20-cm-long, whole-round samples were squeezed solely for helium-isotope analyses, and the pore fluid from an additional 35-cm-long whole-round core sample was split between a regular interstitial water (IW) sample and a 25-mL sample for He isotopes. The pore-water samples for He isotopes were promptly sealed in special gas-tight Cu tubes for shore-based analysis. The IC, TOC, and TS concentration data are reported in Table 12; the XRF data are provided in Tables 13 and 14.

Gas Results

Volatile Hydrocarbons

As part of the shipboard safety and pollution-prevention monitoring program, hydrocarbon gases were analyzed by the headspace technique (see “Explanatory Notes” chapter, this volume) in each core from Holes 1039A and 1039B. Concentrations of methane (C_1) were low throughout the whole sedimentary sequence. The results are summarized in Table 10 and graphically displayed vs. depth in Figure 22. Only in an interval between 25 and 110 mbsf do methane contents exceed the background concentration of 4–8 parts per million by volume (ppmv). In this interval, methane concentrations ranging from 11 to 110 ppmv were detected. Ethane (C_2) was observed only at 84.03 mbsf (Table 10). Sulfate concentrations remain high throughout the recovered sedimentary sequence; thus, strongly reducing conditions needed for bacterial methane generation evidently have never been achieved in the sediments at Site 1039.

Pore-Water Results

Chloride and Salinity

Chloride concentrations are approximately equal to that of seawater, except for the slightly lower Cl concentrations observed in the uppermost 100 m of the sediment section, with a minimum concentration of 545 mM (corresponding to about 2% seawater dilution) centered approximately at 95–130 mbsf and the minor 1% dilution at ~380 mbsf (Fig. 23). The former low-Cl zone is situated within the depth interval of lithologic Subunit U2A, characterized by a very low abundance or absence of diatoms and poorly preserved nannofossils (see “Biostratigraphy and Magnetostratigraphy” section, this chapter). The magnetic susceptibilities and bulk densities are also low in this horizon. Because of the low heat flow at this site, there is no known diagenetic reaction that could have produced in situ water to dilute the section, and there is barely any methane to form gas hydrate. Possibly, a low-Cl fluid conduit existed in the past; except for methane, none of the other chemical profiles clearly suggest active flow at present. The Cl gradient seems diffusive over a depth interval of about 80 m above and below the minimum. In this porous section of low formation factors, the Cl diffusion coefficient is about 6×10^{-6} cm^2/s; thus, the low-Cl fluid must have advected into this horizon prior to 180 ka. Methane concentrations above background levels are observed in Figure 22 at the upper boundary of this low-Cl zone, which may be related to the flow of fluid. The lack of diatoms and the poor preservation of the nannofossils in an otherwise diatom- and coccolith-rich sediment section also may be the result of fluid flow.

Table 9. Depths of biostratigraphic and magnetostratigraphic datums observed from Hole 1039B cores.

Depth (mbsf)	Paleomagnetic datums (Ma)	Nannofossil datums (Ma)	Diatom datums (Ma)	Foraminifer datums (Ma)
1.90				
8.19				
11.35	0.105			
11.35				
18.70	0.200			
20.43				
31.03				
40.38				
49.78		0.46		0.45
59.00	0.780			
59.48				
68.00	0.990			
68.00				
68.88			0.62	
70.00				
71.50				
72.50				
75.00	1.070			
78.00	1.201			
82.00				
83.00	1.211			
87.98				
89.00	1.680			
92.00	1.770			
97.37		1.47		
100.00				
101.00	1.950			
105.00				
106.00	2.140			
106.71				
108.00	2.580			
113.09		1.95	2.01	
118.00	3.040			
122.70				1.77
128.00	3.220			
132.00	3.330			
132.42				
141.77		2.46		
151.19		3.60		4.20
160.97		5.86	6.07	
170.73			7.37	8.30
180.37		8.60	8.17	
189.87		10.80	11.34	
198.65		11.80	12.06	11.80
208.76				
218.43		12.80	12.86	
228.27				
238.00				12.70
247.56				
257.27				
266.84		13.60		
274.15			14.03	
286.25				
296.14				
303.00				
305.00	12.678			
305.67				
315.36				
317.00	12.708			
320.00				
324.86				
327.00	12.775			
329.00	12.819			
332.00	12.991			
334.00	13.139			
334.62				
336.00	13.302			
341.00	13.510			
343.00	13.703			
344.23				
349.00				
351.00	14.076			
352.00	14.178			
352.00				
353.85				
356.00				
356.00	14.612			
363.00				
363.32				
364.00	14.800			
366.00	14.888			
366.00				
366.92				
370.00				
371.00	15.034			
372.89				
375.00	15.155			
375.00				
375.85				
376.00	16.014			
376.50				
377.00	16.327			
378.15		15.60		
381.07				
386.39			16.40	
393.60				16.40
403.06			16.49	
417.28				

Another interesting aspect of the Cl profile is its return to seawater concentration below the minor dilution spike at ~380 mbsf. The salinity depth profiles shown in Figure 23 mimic that of Cl, but with fewer details; the salinity is slightly lower than seawater salinity in the uppermost 130 mbsf and is equal to that of seawater below it.

Sodium and Potassium

The Na/Cl depth profiles of Figure 23C are equal to the seawater ratio throughout most of the section, except for the uppermost 80 mbsf where the ratio is significantly lower than in seawater, and at the basal metalliferous section where the ratio is somewhat higher. The lower ratio from near the sediment/seawater interface to about 80 mbsf is most likely the result of both clay ion-exchange reactions with the pore waters and carbonate precipitation reactions occurring within this same zone as a consequence of the bacterially mediated organic matter diagenetic reactions discussed below. XRF data may unravel the cause of the higher Na concentrations in the basal section. The K concentrations shown in Figure 23D are higher than those in seawater in the hemipelagic section and are caused by ion exchange between K and ammonia in the clay minerals. In the pelagic section, K concentrations are equal to seawater concentrations but increase slightly in the basal metalliferous section, as does the Na. The most interesting feature of the K concentration profile is that, at the base of the basal section, it returns to seawater concentration.

Sulfate, Alkalinity, Ammonium, and Phosphate

Because of moderate sedimentation rates, coupled with moderate organic matter concentrations and possibly also the mixed nature of the organic matter derived from both marine and terrestrial sources, sulfate reduction has not reached completion in the hemipelagic section. The minimum concentration of 13.2 mM occurs at about 25 mbsf (Fig. 24A). It returns to seawater concentration about 350 m deeper within the pelagic section. The long diffusional profile between the sulfate minimum and 280 mbsf indicates a steady state between rates of sulfate reduction and sulfate diffusion from seawater into the sulfate reduction zone, for a time period of ~2.5 m.y., because of the increase in sedimentation rates to ~45 m/m.y. This calculation is based on a sulfate diffusion coefficient of D = 6×10^{-6} cm^2/s (Li and Gregory, 1974).

The alkalinity profile shown in Figure 24B is a mirror image of the sulfate profile. The alkalinity production induces carbonate precipitation, as seen in Figure 25. Similarly, the production of ammonia and dissolved phosphate are intimately related to the bacterially mediated degradation of organic matter. The maximum production of ammonia and phosphate occurs in the upper hemipelagic sediment section where organic matter content is highest (Figs. 24C, D, respectively). At the bottom of the sediment section, all four dissolved biogeochemical components shown in Figure 24 have seawater concentrations.

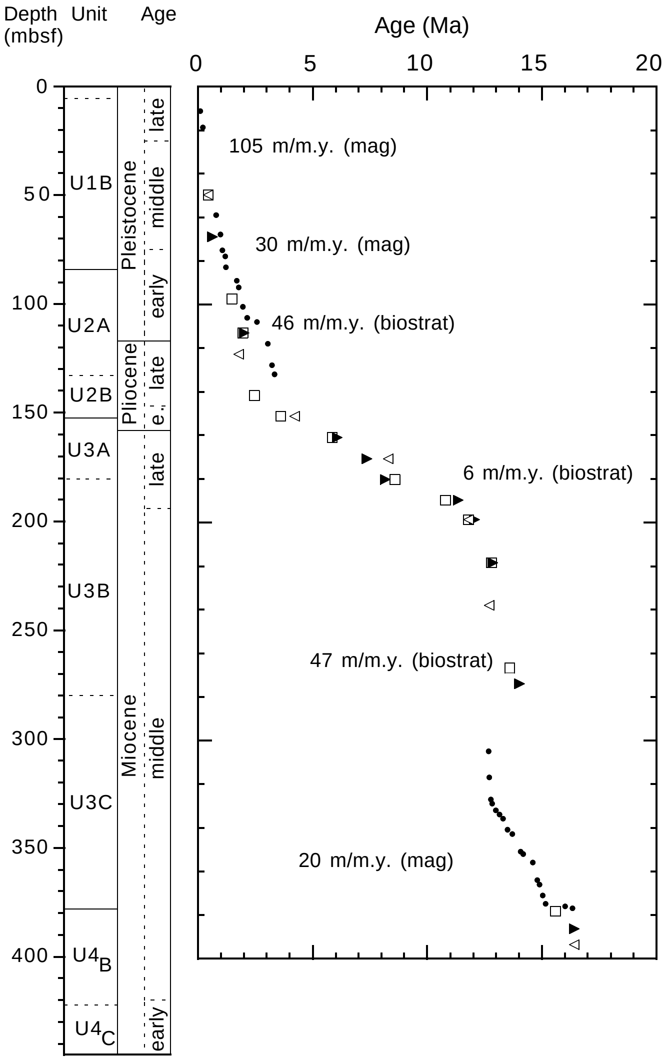

Figure 21. Age-depth relationship of key biostratigraphic datums from the composite section of Holes 1039B and 1039C. Calcareous nannofossils are represented by open boxes, diatoms by solid triangles, and planktonic foraminifers by open triangles. Age-depth rates are approximated for each major biostratigraphic segment (biostrat) of the age-depth curve. Paleomagnetic datums are plotted as solid circles for comparison with the biostratigraphic datums. Paleomagnetic linear sedimentation rates (mag) are also approximated for each major paleomagnetic interval.

Table 10. Composition of headspace gases from Site 1039.

Core, section, interval (cm)	Depth (mbsf)	C_1 (ppmv)	C_2 (ppmv)	C_3 (ppmv)
170-1039A-				
1H-5, 0-5	6.03	8	0	0
2H-5, 0-5	15.03	10	0	0
3H-4, 0-5	24.53	36	0	0
170-1039B-				
4H-2, 145-150	23.95	8	0	0
5H-5, 0-5	36.53	11	0	0
6H-5, 0-5	46.03	13	0	0
7H-5, 0-5	55.53	12	0	0
8H-5, 0-5	65.03	12	0	0
9H-5, 0-5	74.53	13	0	0
10H-5, 0-5	84.03	110	6	<1
11H-5, 0-5	93.53	17	0	0
12X-5, 0-5	103.3	9	0	0
13X-5, 0-5	109.53	11	0	0
14X-5, 0-5	119.23	8	0	0
15X-5, 0-5	128.73	7	0	0
16X-5, 0-5	138.23	8	0	0
17X-5, 0-5	147.83	9	0	0
18X-5, 0-5	157.43	9	0	0
19X-5, 0-5	167.13	8	0	0
20X-5, 0-5	176.63	7	0	0
21X-5, 0-5	186.23	6	0	0
22X-5, 0-5	195.83	5	0	0
23X-5, 0-5	205.53	5	0	0
24X-5, 0-5	215.13	5	0	<1
25X-5, 0-5	224.73	7	0	0
26X-5, 0-5	234.4	5	0	<1
27X-5, 0-5	244.03	7	0	0
28X-5, 0-5	253.73	4	0	0
29X-5, 0-5	263.43	5	0	0
30X-5, 0-5	273.13	5	0	0
31X-5, 0-5	282.73	5	0	0
32X-5, 0-5	292.43	5	0	0
33X-5, 0-5	302.03	5	0	0
35X-5, 0-5	321.23	5	0	0
36X-5, 0-5	330.83	4	0	0
37X-5, 0-5	340.43	4	0	0
38X-5, 0-5	350.03	4	0	0
39X-5, 0-5	359.63	3	0	0
40X-5, 0-5	369.23	3	0	0
41X-3, 0-5	375.82	5	0	0
170-1039C-				
1R-1, 0-5	364.13	4	0	0
2R-2, 0-5	372.73	3	0	0
3R-2, 0-5	383.83	4	0	0
5R-2, 145-150	402.98	3	0	0

Notes: C_1, C_2, and C_3 represent methane, ethane, and propane, respectively. ppmv = parts per million by volume.

This table also appears on the volume CD-ROM.

Calcium and Magnesium

Dissolved Ca concentrations, shown in Figure 25A, are lower than in seawater immediately below the sediment/water interface, and reach a minimum value of 7.8 mM at the depth where alkalinity has its maximum value and sulfate its minimum concentration value, suggesting $CaCO_3$ precipitation. The Ca concentrations then increase with depth to a maximum value of 18.6 mM at ~280 mbsf, where sulfate approaches seawater concentration; below ~280 mbsf, it again decreases with depth toward the seawater value. Alteration of the brown mafic glass-rich crystal-vitric mafic ashes in the calcareous section is most likely responsible for the very high-Ca values in this portion of the sedimentary section. The alteration reactions are consuming alkalinity. The Mg concentrations also decrease with depth from the very top of the section (Fig. 25B), but as Figure 25C shows, at first the Mg consumption with depth is less intense than the Ca consumption; therefore, Mg/Ca values increase with depth. The maximum ratio occurs at the depth of Ca and sulfate concentration minima. The Ca, Mg, and Mg/Ca depth profiles provide insights into the sequence or hierarchy of carbonate diagenetic reactions. They indicate that calcite and Mg-calcite precipitation precede dolomite formation. When sulfate is lowest and the Mg/Ca value highest, dolomite and probably also Mg-calcite formation are the dominant carbonate reactions. Dolomite formation must cease with depth because Mg concentration decreases with depth, reaching a minimum at ~110 mbsf, which is the depth of the minimum Cl concentration. Calcium concentrations increase with depth, lowering the Mg/Ca value to 2.43, about half of the seawater value. As clearly seen in Figure 25B, Mg concentrations increase with depth below 110 mbsf, approaching the value of seawater at the base of the section. The dissolved Ca and Mg concentration gradients in the lower calcareous section are particularly interesting, because most known fluid/rock reactions at both low and elevated temperatures release Ca and consume Mg, but here both behave inversely, suggesting communication with a low-Ca and high-Mg fluid at greater depth; only seawater has these chemical characteristics.

Silica

Dissolved Si concentrations are immediately much higher than the bottom-water value of 125 µM (Table 11; Fig. 25D). Except for relatively low concentrations at the depth of the inferred fluid con-

Table 11. Pore-water chemical data of major and minor constituents, Site 1039.

Core, section, interval (cm)	Depth (mbsf)	Volume (cm^3)	pH	Alkalinity (mM)	Salinity	Cl (mM)	SO$_4$ (mM)	Na (mM)	Mg (mM)	K (mM)	Ca (mM)	Si (µM)	NH$_4$ (µM)	PO$_4$ (µM)	Na/Cl	Mg/Ca
170-1039B-																
1H-1, 145-150	1.45	55	7.77	6.48	34.50	555	25.3	475	49.1	12.7	9.8	612	360	57.2	0.86	5.00
2H-2, 140-150	4.95	55	7.89	14.85	34.50	554	16.5	460	48.9	11.8	8.9	759	1081	48.3	0.83	5.48
2H-5, 140-150	9.45	55	7.74	20.87	34.50	552	15.2	457	48.5	11.5	8.5	775	1150	64.5	0.83	5.71
3H-2, 140-150	14.45	52	7.81	20.57	34.00	550	14.6	455	48.2	11.2	8.2	785	1206	52.7	0.83	5.85
3H-5, 140-150	18.95	55	7.76	20.98	34.00	549	13.3	452	47.4	12.2	8.2	762	1235	46.5	0.82	5.81
4H-2, 140-150	23.95	55	7.71	20.18	34.50	551	13.2	455	47.2	12.3	8.0	772	1336	39.4	0.83	5.93
4H-5, 140-150	28.45	55	7.81	20.24	34.00	551	13.7	455	47.2	13.1	7.8	787	1301	34.1	0.83	6.05
5H-4, 140-150	36.45	55	7.69	18.76	34.00	551	14.0	458	46.7	11.7	8.0	774	1281	26.9	0.83	5.85
6H-4, 140-150	45.93	55	7.63	17.31	34.00	549	14.3	457	45.7	12.4	8.6	787	1274	20.8	0.83	5.34
7H-4, 140-150	55.45	55	7.62	16.19	34.00	549	14.6	457	45.2	12.7	9.0	843	1171	17.2	0.83	5.01
8H-4, 140-150	64.95	55	7.78	15.27	34.50	549	15.5	458	45.1	12.3	9.9	851	1046	17.4	0.83	4.56
9H-4, 140-150	74.45	55	7.66	14.14	34.00	552	16.3	466	43.2	12.5	10.1	794	991	17.4	0.84	4.27
10H-4, 140-150	83.95	55	7.67	13.34	34.00	546	17.3	459	43.4	12.1	11.6	832	911	14.8	0.84	3.74
11H-5, 140-150	94.95	45	7.64	12.27	34.00	545	18.0	457	43.2	12.4	12.4	843	798	12.7	0.84	3.48
12X-3, 135-150	101.43	48	7.68	11.45	34.00	546	19.3	461	42.8	12.4	12.8	830	759	6.8	0.84	3.34
13X-6, 135-150	112.43	53	7.68	9.45	34.00	546	20.1	463	41.9	13.2	13.1	845	721	4.6	0.85	3.19
14X-3, 135-150	117.53	46	7.76	8.58	34.00	545	20.7	462	42.5	13.0	13.4	823	703	2.2	0.85	3.18
15X-6, 135-150	131.63	42	7.86	6.69	34.00	549	22.6	467	43.1	13.1	14.1	683	595	1.8	0.85	3.07
16X-3, 135-150	136.63	50	7.83	6.58	34.00	550	22.3	468	43.1	12.6	14.1	623	578	1.4	0.85	3.06
17X-4, 135-150	147.73	55	7.68	4.91	34.00	554	22.6	471	43.8	12.5	14.2	838	556	1.8	0.85	3.09
18X-4, 135-150	157.33	48	7.59	3.73	34.50	555	23.6	472	44.1	12.9	14.3	913	550	1.2	0.85	3.08
19X-5, 135-150	168.53	50	7.40	3.07	34.50	554	23.8	471	44.3	12.4	14.6	911	481	1.2	0.85	3.04
20X-5, 135-150	178.03	55	7.58	3.37	35.00	554	23.6	469	44.3	12.2	15.9	885	469	1.2	0.85	2.79
21X-5, 135-150	187.63	45	7.43	2.91	34.50	555	23.3	469	44.4	12.7	15.6	926	410	1.4	0.84	2.84
22X-5, 135-150	197.23	55	7.24	2.66	35.00	555	24.1	471	44.1	11.0	16.5	975	388	1.0	0.85	2.68
23X-5, 135-150	206.93	55	7.29	2.60	35.00	554	25.2	471	44.2	11.1	16.9	1001	346	1.2	0.85	2.62
24X-5, 135-150	216.53	35	7.42	2.67	35.00	554	25.0	470	44.4	11.3	16.9	1011	318	1.0	0.85	2.63
25X-5, 135-150	226.13	50	7.43	2.32	35.00	556	25.0	471	44.5	11.5	17.2	1086	291	1.0	0.85	2.58
26X-4, 135-150	232.83	35	7.44	2.28	35.00	559	25.4	476	43.7	11.0	17.7	1031	273	1.0	0.85	2.47
27X-5, 135-150	245.43	50	7.27	2.36	35.00	563	25.6	479	43.9	11.1	18.1	982	241	1.2	0.85	2.43
28X-3, 135-150	252.13	50	7.43	2.15	35.00	554	25.8	469	45.0	10.1	18.1	1016	227	1.4	0.85	2.49
29X-3, 135-150	261.83	48	7.55	2.13	35.00	554	26.5	470	44.8	10.8	18.2	1091	218	1.2	0.85	2.46
30X-2, 135-150	270.03	35	7.56	2.10	35.00	556	27.2	472	45.2	10.9	18.6	1135	185	1.4	0.85	2.44
31X-2, 130-150	279.60	22	7.57	1.90	35.00	558	27.4	477	44.2	11.0	18.2	1195	181	1.2	0.85	2.43
32X-2, 130-150	289.30	50	7.27	1.76	35.50	557	26.8	474	44.8	11.8	17.7	1148	179	1.2	0.85	2.54
33X-3, 130-150	300.40	50	7.61	1.62	36.00	556	26.4	470	45.2	11.5	18.2	1095	162	1.2	0.85	2.48
34X-3, 130-150	309.90	20	7.59	1.79	34.00	557	26.1	472	45.6	11.1	17.5	1082	141	1.2	0.85	2.61
35X-3, 130-150	319.60	35	7.60	1.80	35.00	558	26.0	474	45.8	9.9	17.3	1116	121	1.4	0.85	2.65
36X-5, 130-150	332.20	30	7.68	1.78	35.00	557	26.8	474	46.1	10.8	17.0	1135	108	1.4	0.85	2.72
37X-5, 130-150	341.80	50	7.53	1.74	35.00	559	26.3	475	46.5	11.5	16.2	1088	92	1.4	0.85	2.87
38X-3, 130-150	348.40	40	7.45	1.83	35.50	562	26.6	477	47.3	11.5	15.8	1054	115	1.4	0.85	2.99
39X-5, 130-150	361.00	50	7.72	1.62	35.50	562	27.1	482	46.9	11.2	14.7	1061	60	1.4	0.86	3.19
40X-6, 130-150	372.10	50	7.83	1.66	35.00	557	26.4	477	47.2	11.0	13.7	1020	34	1.2	0.86	3.44
41X-1, 130-150	374.20	42	8.17	1.63	35.00	554	27.4	474	47.8	11.0	13.9	702	28	1.4	0.86	3.44
170-1039C-																
WSTP		10.50	ND	ND	35.0	556	28.2	473	53.8	10.5	10.5	125	19	0.5	0.85	5.12
1R-2, 125-150	365.30	55	7.77	1.992	35.0	557	27.5	474	47.1	11.7	16.0	966	74	1.2	0.85	2.95
2R-1, 65-100	373.53	62	7.64	1.793	35.0	560	28.3	480	47.1	11.4	15.7	992	72	1.4	0.86	3.00
3R-2, 132-150	385.21	52	7.83	1.711	35.5	552	27.6	473	46.4	12.2	14.8	975	60	1.2	0.86	3.14
4R-1, 132-150	393.31	52	7.96	1.483	35.0	554	27.0	474	47.1	12.0	13.7	945	50	1.0	0.86	3.44
5R-1, 0-6	401.53	25	7.77	1.621	35.0	556	27.4	476	47.7	12.1	13.9	883	40	1.0	0.86	3.43
6R-4, 128-142	417.00	52	7.97	1.511	35.0	557	26.5	476	47.6	11.6	13.6	629	23	1.0	0.85	3.50
7R-1, 85-100	421.73	53	7.80	1.857	35.0	559	27.8	482	47.0	10.2	14.0	574	29	1.0	0.86	3.36

Note: ND = not determined.

duit, where diatoms are absent or rare, overall Si concentrations increase with depth, and at ~300 mbsf reach saturation with respect to opal-A. Below this depth, silica values decrease steeply with depth despite the fact that diatoms are still abundant in the basal sediment section (see "Biostratigraphy and Magnetostratigraphy" section, this chapter). Either diffusive communication with a low-Si fluid (most likely seawater) or a Si sink exists at greater depths. It is not surprising that dissolved Si values are high throughout most of this reference section, which is rich in diatoms.

Sediment and Igneous Rock Results

Inorganic Carbon, Organic Carbon, and Total Sulfur

The distribution of inorganic and organic carbon, calcium carbonate, and sulfur in the sediments from Holes 1039A, 1039B, and 1039C are reported in Table 12.

The carbonate content varies from 0.5 to 87.8 wt%, assuming that all the carbonates are present as pure calcite, and its distribution with depth shows three distinct patterns (Fig. 26A). In the upper part of the sediment column (Units U1 and U2, except lowermost part of Subunit U2B), concentrations are characterized by small-scale variations (0.3–4.6 wt%). Between 120 and 160 mbsf (lowermost Subunit U2B and Subunit U3A), alternating high- and low-carbonate contents were measured. The range of carbonate contents reflects the varying amounts of noncarbonate hemipelagic sediments. Below this zone, $CaCO_3$ concentration increases considerably up to 87.8 wt% and remains high throughout the whole sedimentary Subunit U3B, except for lower carbonate concentrations (between about 270 and 280 mbsf) because of admixed volcanic ash and diatom-rich sediments.

Total organic carbon contents range from almost zero to 2.1 wt% (Fig. 26B; Table 12). The highest concentrations occur in the turbiditic sequence (Subunit U1A), suggesting a downward slope transport of sediments enriched in organic compounds. Below that interval, TOC shows a steady decrease from 1.3 wt% at 8.1 mbsf to 0.1 wt% at 161.1 mbsf. The pelagic, carbonate-rich sediments of Unit U3 are characterized by low TOC concentrations ranging from 0.1 to 0.94 wt%.

Total sulfur (TS) concentrations at Site 1039 are generally high in the hemipelagic sediments (lithologic Unit U1 and Subunit U2A). TS contents vary in this section from 0.1 to 2.2 wt% (Fig. 26C; Table 12). These high-sulfur concentrations mostly represent the abundance of pyrite in the core (see "Lithostratigraphy" section, this chap-

Table 12. Inorganic carbon, calcium carbonate, total carbon, total organic carbon, and total sulfur contents in sediments at Site 1039.

Core, section, interval (cm)	Depth (mbsf)	IC (wt%)	$CaCO_3$ (wt%)	TC (wt%)	TOC (wt%)	TS (wt%)
170-1039A-						
1H-1, 132-133	1.33	0.41	3.4	2.30	1.89	0.36
1H-3, 128-129	4.29	0.16	1.3	2.24	2.08	0.26
1H-6, 78-79	8.29	0.05	0.5	1.39	1.34	0.72
2H-1, 146-147	10.47	0.14	1.1	1.95	1.81	0.85
2H-2, 147-148	11.98	0.40	3.3	ND	ND	ND
2H-5, 146-147	16.47	0.28	2.3	1.84	1.56	0.59
3H-1, 148-149	19.99	0.22	1.9	1.45	1.23	0.26
3H-4, 147-148	24.48	0.27	2.3	1.59	1.32	0.6
170-1039B-						
4H-2, 37-38	22.88	0.11	0.9	1.26	1.16	1.3
4H-4, 37-38	25.88	0.06	0.5	ND	ND	ND
4H-6, 37-38	28.88	0.34	2.8	1.97	1.63	0.25
5H-2, 36-37	32.37	0.26	2.1	ND	ND	ND
5H-4, 31-32	35.32	0.30	2.5	0.78	0.48	0.15
5H-6, 35-36	38.36	0.23	1.9	0.83	0.6	0.24
6H-2, 34-35	41.85	0.20	1.6	ND	ND	ND
6H-4, 34-35	44.85	0.28	2.3	1.20	0.92	0.44
6H-6, 34-35	47.85	0.19	1.5	1.14	0.96	0.07
7H-2, 34-35	51.35	0.09	0.8	ND	ND	ND
7H-4, 34-35	54.35	0.14	1.2	ND	ND	ND
7H-6, 34-35	57.35	0.55	4.6	1.89	1.34	0.22
8H-4, 34-35	63.85	0.23	1.9	ND	ND	ND
8H-6, 34-35	66.85	0.25	2.1	0.93	0.68	0.44
9H-2, 34-35	70.35	0.41	3.4	ND	ND	ND
9H-4, 34-35	73.35	0.08	0.6	0.92	0.84	1.5
9H-6, 34-35	76.35	0.54	4.5	1.33	0.79	0.14
10H-2, 37-38	79.88	0.53	4.4	ND	ND	ND
10H-4, 36-37	82.87	0.21	1.7	ND	ND	ND
11H-2, 35-36	89.36	0.04	0.3	0.48	0.44	2.2
11H-4, 34-35	92.35	0.22	1.8	ND	ND	ND
11H-6, 34-35	95.35	0.03	0.3	0.67	0.64	0.32
12X-1, 30-31	97.31	0.05	0.4	ND	ND	ND
12X-4, 40-41	101.91	0.04	0.3	0.75	0.71	0.19
12X-6, 35-36	104.86	0.05	0.5	ND	ND	ND
13X-2, 34-35	105.35	0.34	2.9	ND	ND	ND
13X-4, 35-36	108.36	0.25	2.1	ND	ND	ND
13X-6, 35-36	111.36	0.26	2.2	0.79	0.53	0.07
14X-2, 34-35	114.36	0.21	1.8	ND	ND	ND
14X-4, 34-35	117.94	0.18	1.5	ND	ND	ND
14X-6, 33-34	120.94	0.50	4.2	1.14	0.64	0
15X-2, 35-36	124.56	0.51	4.2	ND	ND	ND
15X-4, 36-37	127.57	0.84	7.0	ND	ND	ND
15X-6, 35-36	130.56	0.16	1.3	0.62	0.46	0
16X-2, 34-35	134.05	0.39	3.3	ND	ND	ND
16X-4, 34-35	137.05	0.85	7.0	ND	ND	ND
16X-6, 34-35	140.05	1.34	11.2	ND	ND	ND
17X-2, 34-35	143.65	2.86	23.8	ND	ND	ND
17X-4, 34-35	146.65	4.12	34.3	4.49	0.37	0
17X-6, 34-35	149.65	0.51	4.2	ND	ND	ND
18X-2, 34-35	153.25	0.71	5.9	ND	ND	ND
18X-4, 34-35	156.25	5.11	42.6	ND	ND	ND
18X-6, 34-35	159.25	0.75	6.3	ND	ND	ND
19X-2, 34-35	162.95	0.91	7.6	1.03	0.12	0
19X-4, 34-35	165.95	3.56	29.4	ND	ND	ND
19X-6, 34-35	168.95	0.15	1.2	ND	ND	ND
20X-2, 34-35	172.45	0.13	1.1	ND	ND	ND
20X-4, 34-35	175.45	0.14	1.2	ND	ND	ND
20X-6, 34-35	178.45	0.57	4.7	ND	ND	ND
21X-2, 34-35	182.05	5.99	49.9	5.33	0	0
21X-4, 34-35	185.05	7.61	63.4	ND	ND	ND
21X-6, 34-35	188.05	10.13	84.4	ND	ND	ND
22X-2, 24-25	191.05	9.36	78.0	ND	ND	ND
22X-4, 34-35	194.65	9.56	79.7	9.90	0.34	0
22X-6, 34-35	197.65	8.30	69.1	ND	ND	ND
23X-2, 34-35	201.35	8.96	74.6	ND	ND	ND
23X-4, 34-35	204.35	9.73	81.1	ND	ND	ND
24X-4, 34-35	213.95	10.50	87.8	ND	ND	ND
24X-6, 34-35	216.95	9.74	81.1	ND	ND	ND
25X-2, 34-35	220.55	10.19	84.9	ND	ND	ND
25X-4, 34-35	223.55	9.15	76.2	ND	ND	ND
25X-6, 34-35	226.55	9.58	79.8	9.75	0.17	0
26X-4, 34-35	233.25	9.88	82.3	ND	ND	ND
26X-6, 34-35	236.25	9.34	77.8	ND	ND	ND
27X-4, 34-35	242.85	8.31	69.2	ND	ND	ND
27X-6, 34-35	245.85	9.22	76.8	ND	ND	ND
28X-2, 34-35	249.55	8.57	71.4	ND	ND	ND
28X-4, 34-35	252.55	9.23	76.9	ND	ND	ND
28X-6, 34-35	255.55	6.48	54.0	ND	ND	ND
29X-2, 34-35	259.55	9.46	78.8	ND	ND	ND
29X-4, 34-35	262.25	8.10	67.5	8.25	0.15	0
29X-6, 34-35	265.25	8.99	74.9	ND	ND	ND
30X-2, 34-35	269.83	5.80	48.3	ND	ND	ND
30X-4, 32-33	272.83	3.93	32.8	4.27	0.34	0
31X-2, 34-35	278.55	4.35	36.3	ND	ND	ND
31X-4, 34-35	281.55	7.23	60.2	ND	ND	ND
31X-6, 34-35	284.55	7.11	59.2	ND	ND	ND
32X-2, 33-34	288.54	9.09	75.7	ND	ND	ND
32X-4, 35-36	291.26	8.02	66.8	8.00	0	0
32X-6, 34-35	294.25	8.33	69.4	ND	ND	ND
33X-2, 34-35	297.85	8.34	69.4	ND	ND	ND
33X-4, 33-34	300.84	8.40	70.0	ND	ND	ND
33X-6, 38-39	303.89	7.04	58.7	ND	ND	ND
34X-2, 34-35	307.45	9.43	78.6	ND	ND	ND
34X-4, 33-34	310.44	9.23	76.9	ND	ND	ND
34X-6, 34-35	313.45	7.35	61.3	8.29	0.94	0
35X-2, 34-35	317.05	7.35	61.2	ND	ND	ND
35X-4, 34-35	320.05	8.12	67.6	ND	ND	ND
36X-2, 34-35	326.65	7.91	65.9	ND	ND	ND
36X-4, 34-35	329.65	7.65	63.7	ND	ND	ND
36X-6, 34-35	332.65	7.64	63.6	ND	ND	ND
37X-2, 34-35	336.25	7.12	59.3	ND	ND	ND
37X-4, 124-125	340.15	6.29	52.4	6.67	0.38	0
37X-6, 35-36	342.16	7.21	60.1	ND	ND	ND
38X-2, 34-35	345.85	6.06	50.5	ND	ND	ND
38X-4, 34-35	348.85	7.54	62.8	ND	ND	ND
38X-6, 34-35	351.85	4.54	37.9	ND	ND	ND
39X-2, 34-35	355.45	5.77	48.0	ND	ND	ND
39X-4, 34-35	358.45	6.46	53.8	ND	ND	ND
39X-6, 34-35	361.45	7.16	59.6	ND	ND	ND
40X-2, 34-35	365.04	5.15	42.9	ND	ND	ND
40X-4, 34-35	368.05	7.13	59.4	ND	ND	ND
40X-6, 34-35	371.05	5.07	42.3	5.13	0.06	0
41X-2, 34-35	374.55	6.60	55.0	ND	ND	ND
170-1039C-						
1R-2, 116-117	365.77	7.76	64.6	ND	ND	ND
2R-2, 63-64	373.83	7.49	62.4	ND	ND	ND
3R-2, 128-129	385.09	5.51	45.9	ND	ND	ND
6R-2, 114-115	413.17	5.63	46.9	ND	ND	ND
6R-4, 115-116	416.76	5.59	46.6	ND	ND	ND
7R-1, 79-80	420.50	4.12	34.3	ND	ND	ND

Notes: IC = inorganic carbon, $CaCO_3$ = calcium carbonate, TC = total carbon, TOC = total organic carbon, and TS = total sulfur. ND = not determined.

This is a sample of the table that appears on the volume CD-ROM.

ter). Below this sequence, no sulfur was detected throughout lithologic Unit U3.

X-ray Fluorescence Analyses of the Solid Phases

Major and trace element analyses of 31 silicic sediments, volcanic ashes, and gabbros, plus trace element analyses of another 20 calcareous sediments from Site 1039, were conducted shipboard, following standard methods (see the "Explanatory Notes" chapter, this volume). Major element analyses are presented in Table 13, and trace element data are reported in Table 14. Nb contamination (up to ~1–2 ppm) is significant in the siliceous and calcareous oozes, and Ce and Cr values are near detection limits and not reliable in the biogenic sediments. Analyses were made on dried bulk samples that are a mixture of sediment particles and sea salts; CaO, MgO, and Na_2O contents reported in Table 13 have not yet been corrected for porosity and pore-water contribution to the bulk-sediment composition.

The XRF geochemistry of Site 1039, the reference site, is useful in a number of different ways. The data can be used to

1. Track the lithologic and sedimentologic variations within the sedimentary section;
2. Identify features not easily visible in the cores, such as the presence of basal metalliferous carbonate;
3. Constrain the source(s) of the volcanogenic detrital component at Site 1039, with tectonic implications;
4. Evaluate the chemical similarities between the gabbro sills, Galapagos, and East Pacific Rise lavas at similar MgO contents;
5. Evaluate the provenance of the detrital component in the upper 150 m of Site 1039;
6. Determine the average composition of the sediment column for key elements entering the subduction zone to further recycling studies; and

Table 13. Major and minor element (XRF) analyses for siliceous sediments, volcanic ashes, and gabbros.

Core, section, interval (cm)	Depth (mbsf)	Lithology	SiO_2	TiO_2	Al_2O_3	Fe_2O_3*	MnO	MgO	CaO	Na_2O	K_2O	P_2O_5	Total	LOI
170-1039A-														
3H-3, 104-109	22.54	Diatom. ooze w/ minor ash	68.40	0.41	14.48	4.82	0.095	1.16	2.14	3.58	3.308	0.060	98.43	6.23
170-1039B-														
2H-2 ,140-150	4.90	Same	58.96	1.12	17.49	9.90	0.089	3.90	1.80	3.11	2.136	0.151	98.63	16.00
4H-2, 140-150	23.90	Silic. ooze w/minor ash	59.41	1.02	16.90	8.84	0.198	3.81	3.00	3.03	2.048	0.137	98.37	15.79
6H-4, 134-150	45.84	Same	62.65	0.87	16.18	7.84	0.144	3.03	2.94	2.63	2.471	0.114	98.86	11.33
8H-4, 140-150	64.90	Same	59.09	0.99	17.23	9.18	0.225	4.05	2.17	2.82	2.282	0.118	98.14	19.38
10H-1, 33-37	78.33	Ash-rich layer	74.75	0.38	13.73	2.39	0.061	0.60	1.74	3.21	4.005	0.046	100.89	5.50
10H-4, 140-150	83.93	Silic. ooze w/minor ash	60.84	0.96	17.85	8.57	0.103	3.53	2.42	2.44	2.354	0.136	99.18	17.14
11H-1, 42-47	87.92	Ash-rich layer	72.63	0.33	13.80	2.17	0.077	0.74	1.54	2.85	4.653	0.036	98.82	5.48
12X-3, 135-150	101.35	Silty clay with diatoms	60.42	1.09	18.15	9.34	0.071	3.82	1.41	2.03	2.203	0.094	98.61	18.28
14X-3, 135-150	117.45	Silty clay w/ silic. fossils	63.74	0.75	15.70	6.68	0.237	2.96	2.57	2.14	2.738	0.100	97.59	13.14
15X-6, 135-150	131.55	Silty clay w/minor ash	60.99	0.91	17.34	7.70	0.462	3.76	1.92	1.99	2.567	0.141	97.75	14.25
16X-1, 49-55	132.69	Ash-rich layer	60.57	0.89	16.88	7.96	0.188	4.04	1.95	3.50	2.485	0.138	98.58	10.55
16X-1, 63-68	132.83	Same	71.60	0.34	14.10	3.49	0.083	1.08	1.77	2.83	3.693	0.031	99.01	6.80
16X-3, 135-150	136.55	Clay with calc. layers & ash	58.18	1.01	17.85	9.06	0.307	4.36	2.23	2.67	2.148	0.172	97.97	16.65
17X-3, 135-150	146.15	Calcareous clay	41.65	0.63	12.29	6.45	1.044	2.22	28.51	1.79	1.048	0.274	95.88	26.65
19X-3, 10-15	164.20	Ash-rich layer	68.37	0.38	7.60	3.46	0.303	1.71	9.07	2.90	1.555	0.159	95.49	14.02
36X-5, 57-63	331.37	Same	55.01	0.50	9.94	4.95	0.674	1.97	18.79	2.34	1.301	0.216	97.25	10.55
41X-1, 30-50	373.10	Same	61.69	0.44	8.77	4.21	0.488	1.84	13.93	2.62	1.428	0.188	96.37	9.83
41X-2, 102-106	375.32	Biogenic ooze	66.32	0.31	3.11	3.35	0.255	3.07	18.66	1.42	0.484	0.168	97.13	16.91
41X-CC, 3-7	377.67	Gabbro/Hornfels	59.68	0.23	1.74	3.03	0.720	22.29	10.06	0.77	0.089	0.065	98.66	12.20
42X-1, 22-24	381.02	Gabbro	48.74	1.42	15.47	11.79	0.199	7.15	12.43	2.48	0.108	0.139	99.90	0.72
170-1039C-														
7R-2, 43-46	422.23	Same	48.63	2.00	14.49	12.84	0.175	6.89	10.99	2.38	0.574	0.227	99.19	0.30
7R-3, 73-76	423.96	Same	48.59	2.00	14.49	12.61	0.181	6.76	11.61	2.25	0.399	0.222	99.10	0.15
8R-3, 90-93 (Piece 1B)	433.11	Same	48.92	1.97	14.82	12.50	0.182	6.66	11.77	2.50	0.324	0.224	99.86	0.20
8R-5, 63-67 (Piece 2)	435.31	Same	48.97	1.97	14.53	12.45	0.177	6.96	11.37	2.52	0.202	0.222	99.35	0.54
9R-1, 0-4 (Piece 1A)	435.70	Same	48.71	1.90	14.84	12.21	0.167	6.76	11.62	2.47	0.233	0.215	99.12	0.61
9R-2, 45-48 (Piece 1B)	437.56	Same	48.94	1.96	14.38	12.49	0.165	6.85	11.76	2.60	0.219	0.225	99.57	0.51
10R-1, 64-68 (Piece 1D)	440.54	Same	48.38	1.88	14.33	12.94	0.179	6.96	11.51	2.49	0.355	0.223	99.24	0.41
10R-3, 25-29 (Piece 1B)	442.66	Same	48.94	1.88	14.19	12.70	0.178	6.61	11.78	2.50	0.348	0.228	99.34	0.27
11R-1, 58-61 (Piece 5)	443.58	Same	48.47	1.50	15.07	12.64	0.192	6.64	12.01	2.50	0.149	0.152	99.31	0.19
11R-2, 47-50 (Piece 1C)	444.69	Same	48.95	1.55	14.68	13.11	0.198	6.30	11.97	2.47	0.162	0.154	99.53	-0.06

Notes: Fe_2O_3* = total iron as Fe_2O_3. All concentrations are in weight percent.

7. Help constrain estimates of underplating.

Figure 27 shows variations in MnO, P_2O_5, Cu, Ni, and Ba with depth. Although the sample density is somewhat sparse, all profiles show an increase in the concentration of these elements between ~130 and 180 mbsf, within and just above the interval of slow sedimentation rates reported in the "Biostratigraphy and Magnetostratigraphy" section (this chapter). These peaks, particularly in Cu, Ni, and Ba concentrations, may serve as a stratigraphic marker for comparison with the compacted underthrust section at Site 1040. Highest concentrations are often seen in the ash-rich layer at 164 mbsf. The combination of extremely high concentrations of the compatible elements Cu and Ni, together with extremely high concentrations of the incompatible element Ba, however, is generally not seen in siliceous arc volcanic rocks, suggesting that the element enrichment is not a characteristic of the volcanic detritus. Rather, accumulation in the sediment of phases such as Mn nodules, phosphates, sulfides, and barite is seen most clearly where there is little biogenic sediment to dilute their chemical signatures.

Figure 28 plots Cu, Ni, Zn, and V against depth for the calcareous sediments at the base of Site 1039. The transition metal concentrations begin to increase at ~340 mbsf, just above the base of lithologic Subunit U3B (see "Lithostratigraphy" section, this chapter). Concentrations remain high throughout the sometimes brecciated Subunit U3C, reaching levels that are typically about twice those seen in the overlying carbonates, over a depth interval of 80 m in Hole 1039C. Ba shows negligible to slight enrichment. Mn data are not available for the calcareous sediments, and no other measured elements show similar increases. The Leg 138 shipboard party reported 2.5 m of basal metalliferous sediment above basement, identified visually (Mayer, Pisias, Janecek, et al., 1992). Scientists recovered 28.5 m of metalliferous sediment, identified visually, during DSDP Leg 67, Site 495, off Guatemala (Shipboard Scientific Party, 1982). The metal enrichments are thought to derive from incorporation of hydrothermally transported metals near the ridge axis. At Site 1039, sill emplacement also may have played a role in transition metal enrichment.

Ash layers are abundant in Site 1039, and volcanic detritus is nearly ubiquitous at the trace–common level in much of the sediment recovered (see "Lithostratigraphy" section, this chapter). Major and trace element analyses were measured on volcanic ash layers greater than 10 cm thick. Figure 29 shows the significantly elevated concentrations of Zr, Nb, and Ce in the ashes between 330 and 370 mbsf. For these ashes, Nb contamination from the shatterbox will be negligible; for the lower concentration ashes, Zr/Nb values may be lowered by 10%–20% through Nb contamination. Figure 29D shows that the ashes with elevated Zr, Nb, and Ce also have significantly lower Zr/Nb values than do the ashes above 164 mbsf. Zr/Nb is an especially useful petrogenetic discriminator in this setting. The ratio in the bulk sediment is determined by that of the volcanic detritus with little contribution from the siliceous or calcareous components. As such, the ratio should be little affected by mixing of different proportions of biogenic material with the ash. In the upper part, the ashes have high Zr/Nb values that are comparable to those from the Costa Rican volcanoes of Arenal, Irazu, and Turrialba. Below 330 m, the two ashes have Zr/Nb values that are distinct not only from volcanic arcs, but also from normally depleted mid-ocean ridge basalt (N-MORB). The

Table 14. Trace element analyses (XRF) for siliceous and calcareous sediments, volcanic ashes, and gabbros.

Core, section, interval (cm)	Depth (mbsf)	Lithology	Nb	Zr	Y	Sr	Rb	Zn	Cu	Ni	Cr	V	Ce	Ba
170-1039A-														
3H-3, 104-109	22.54	Diatom. ooze w/ minor ash	12.6	154.1	13.5	270.9	75.8	69	42	57	11	53	60	1391
170-1039B-														
2H-2, 140-150	4.90	Same	3.6	109.2	21.7	190.0	39.0	162	131	89	97	205	8	1159
4H-2, 140-150	23.90	Silic. ooze w/minor ash	3.3	107.8	18.3	229.5	38.2	216	132	109	84	186	13	1513
6H-4, 134-150	45.84	Same	4.9	128.2	17.6	298.7	45.4	150	99	83	54	159	30	1342
8H-4, 140-150	64.90	Same	4.6	109.2	18.9	262.2	43.1	225	129	135	72	187	22	1668
10H-1, 33-37	78.33	Ash-rich layer	6.6	205.2	21.0	194.7	73.5	35	21	19	-2	22	43	1457
10H-4, 140-150	83.93	Silic. ooze w/minor ash	4.9	108.4	18.3	295.1	42.9	147	125	78	59	172	30	1314
11H-1, 42-47	87.92	Ash-rich layer	9.8	134.6	10.8	237.9	100.7	43	23	12	0	25	56	1648
12X-3, 140-150	101.35	Silty clay with diatoms	5.1	114.0	19.9	227.4	40.4	165	127	93	78	211	15	1474
14X-3, 135-150	117.45	Silty clay w/ silic. fossils	7.0	117.9	21.6	292.9	52.2	249	161	210	54	139	19	2719
15X-6, 135-150	131.55	Silty clay w/minor ash	7.0	112.6	35.2	341.6	41.9	243	201	236	79	149	18	4062
16X-1, 49-55	132.69	Ash-rich layer	4.0	110.3	30.3	293.3	43.1	177	605	161	72	131	13	3798
16X-1, 63-68	132.83	Same	3.2	103.3	11.7	242.0	65.7	50	64	84	4	37	23	1876
16X-3, 135-150	136.55	Clay with calc. layers & ash	4.5	64.9	32.7	892.8	25.0	127	107	146	49	83	19	3632
19X-3, 10-15	164.20	Ash-rich layer	2.4	90.5	37.1	521.2	30.4	325	525	517	17	79	BDL	6924
19X-5, 135-150	168.45	Clayey biogenic ooze	3.6	63.5	36.0	1080.6	20.4	402	157	477	17	54	BDL	6975
23X-5, 135-150	206.85	Nannofossil ooze w/diatoms	BDL	10.7	10.6	1147.6	1.7	29	44	10	BDL	12	BDL	1954
27X-4, 135-150	243.85	Siliceous nannofossil ooze	0.4	6.2	9.3	1316.3	2.5	17	25	9	BDL	8	BDL	1883
31X-2, 130-150	279.50	Diatom. nanno. ooze w/minor ash	0.5	15.9	9.0	960.1	2.6	20	40	8	2	11	0	1846
35X-3, 130-150	319.50	Silic. nanno. ooze w/minor ash	1.7	17.6	9.0	1040.1	3.2	19	29	10	0	8	6	1663
36X-5, 57-63	331.37	Ash-rich layer	90.6	461.8	34.0	500.6	83.5	243	29	29	21	53	108	1327
37X-5, 130-150	341.70	Siliceous nannofossil ooze	3.3	19.1	10.2	1164.5	5.2	40	49	28	1	19	BDL	2056
38X-3, 130-150	348.30	Same	4.0	28.1	11.5	1145.1	7.0	81	76	52	8	39	5	2129
39X-5, 130-150	360.90	Calc. ooze w/sil. fossils, minor ash	5.5	34.2	11.2	1146.0	7.1	45	51	19	5	34	14	1784
40X-6, 130-150	372.00	Matrix supp. breccia, biogen. ooze	4.3	21.3	11.9	897.7	7.6	28	40	12	2	14	4	2507
41X-1, 30-50	373.10	Ash-rich layer	146.1	829.9	49.9	159.4	66.5	176	9	11	BDL	18	180	750
41X-1, 130-150	374.10	Matrix supp. breccia, calc. ooze	33.2	195.0	20.9	610.3	22.1	76	64	30	33	86	48	1423
41X-2, 102-106	375.32	Biogenic ooze	11.0	64.8	14.2	652.6	8.1	71	96	46	16	56	3	2553
41X-CC, 3-7	377.67	Gabbro/Hornfels	4.3	24.1	34.3	170.7	1.6	63	11	36	11	37	20	203
42X-1, 22-24	381.02	Gabbro	8.7	90.4	22.1	176.6	2.9	60	67	83	206	308	23	29
170-1039C-														
1R-2, 125-150	365.72	Diatomaceous nannofossil ooze	14.4	85.6	13.6	1087.2	15.7	46	50	21	4	23	18	1987
3R-2, 132-150	384.95	Nannofossil ooze w/diatoms	2.4	31.5	10.5	1042.4	6.9	71	70	30	15	66	BDL	2146
5R-1, 0-6	401.50	Same	8.2	64.0	13.4	919.4	12.1	58	80	38	18	56	2	2153
6R-4, 128-142	416.98	Same	7.4	63.2	16.1	775.8	9.0	84	107	53	33	105	6	2240
7R-1, 85-100	421.65	Diatomaceous nannofossil ooze	4.2	42.3	9.9	453.2	4.6	57	72	26	24	69	0	1957
7R-2, 43-46	422.23	Gabbro	16.8	154.1	28.7	219.9	8.3	85	187	84	220	346	46	162
7R-3, 73-76	423.96	Same	17.1	156.0	29.7	222.5	8.1	85	156	85	246	335	38	88
8R-3, 90-93 (Piece 1B)	433.11	Same	16.5	152.7	28.8	227.4	6.8	85	145	87	229	332	41	87
8R-5, 63-67 (Piece 2)	435.31	Same	17.2	152.7	28.1	223.1	2.5	75	85	83	242	338	35	68
9R-1, 0-4 (Piece 1A)	435.70	Same	16.9	147.7	27.5	240.1	4.3	118	120	84	243	323	43	270
9R-2, 45-48 (Piece 1B)	437.56	Same	17.2	153.2	28.7	226.7	3.2	92	157	89	252	332	46	66
10R-1, 64-68 (Piece 1D)	440.54	Same	18.7	156.9	30.3	221.6	4.4	87	135	92	264	338	44	64
10R-3, 25-29 (Piece 1B)	442.66	Same	19.4	155.3	29.1	218.0	6.8	80	172	87	233	331	44	85
11R-1, 58-61 (Piece 5)	443.58	Same	12.1	105.1	25.0	179.0	4.6	82	166	82	150	378	25	54
11R-2, 47-50 (Piece 1C)	444.69	Same	11.1	106.6	27.7	175.0	4.0	78	164	78	139	359	31	36

Notes: BDL = below detection limit. All concentrations are in parts per million.

two basal ashes have ratios typical of plume-enriched mid-ocean ridge basalt (MORB) or ocean-island tholeiites similar to the Galapagos (Wilson, 1989).

The gabbros from Site 1039 have a very restricted range of major and trace element composition. Being nearly holocrystalline, the gabbros probably do not represent original liquid compositions. At equal MgO content, the Site 1039 gabbros have TiO_2, Na_2O, K_2O, and P_2O_5 concentrations similar to both Galapagos and East Pacific Rise gabbros (White et al., 1993). Zr/Nb values for the Site 1039 gabbros fall in the range 8.0–10.4 (Fig. 29D). These values are significantly lower than those found in typical depleted MORB, but are similar to values seen in plume-enriched MORB or ocean-island tholeiites like the Galapagos (Wilson, 1989).

Figure 30 shows the similarity in chemical composition between the diatomaceous oozes with minor ash layers of Unit U1, and the silty clays with diatoms of Unit U2. Unit U1 is characterized by high Fe_2O_3* and TiO_2 (5–9 wt% and 0.4–1 wt%, respectively), arguing for ubiquitous and significant input of detrital material throughout the unit. The uppermost volcanic ashes, thought to derive from the volcanic arc, are rich in silicic glass (70–75 wt% SiO_2) and are equivalently poor in Fe_2O_3* and TiO_2 (<2.5 and <0.5 wt%, respectively). Adding this volcanic detritus to the diatomaceous oozes cannot produce their observed chemistry. The chemical data for the sediment from the accretionary prism (see “Geochemistry” section, “Site 1040” chapter, this volume) shows, however, that the chemical variations in the upper 150 m of Site 1039 can be produced by mixing

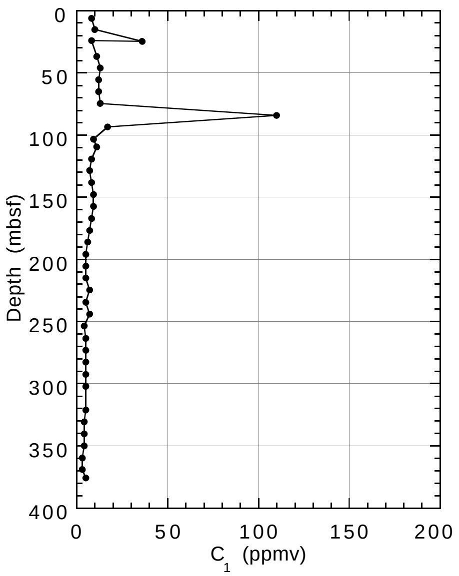

Figure 22. Results of headspace gas analyses for methane (C_1) vs. depth at Site 1039.

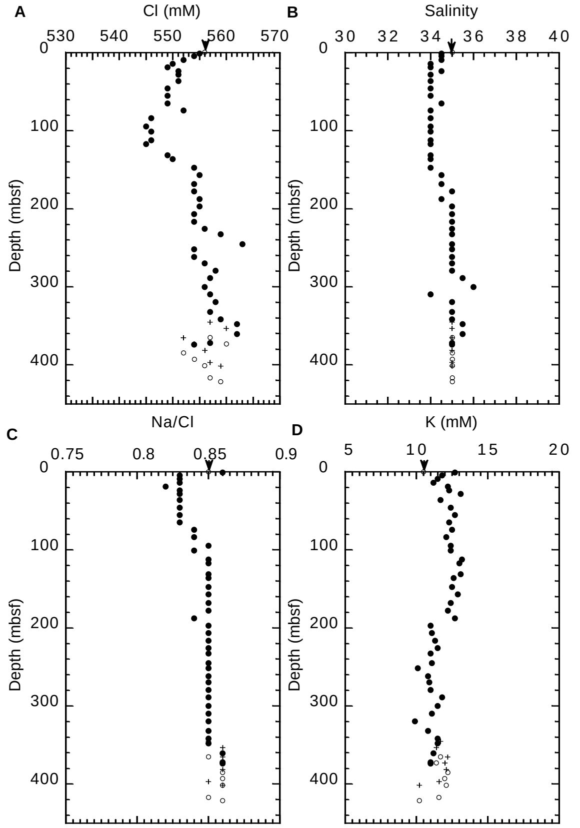

Figure 23. Concentration depth profiles of (**A**) Cl, (**B**) salinity, (**C**) Na/Cl, and (**D**) K. Arrow indicates seawater concentration.

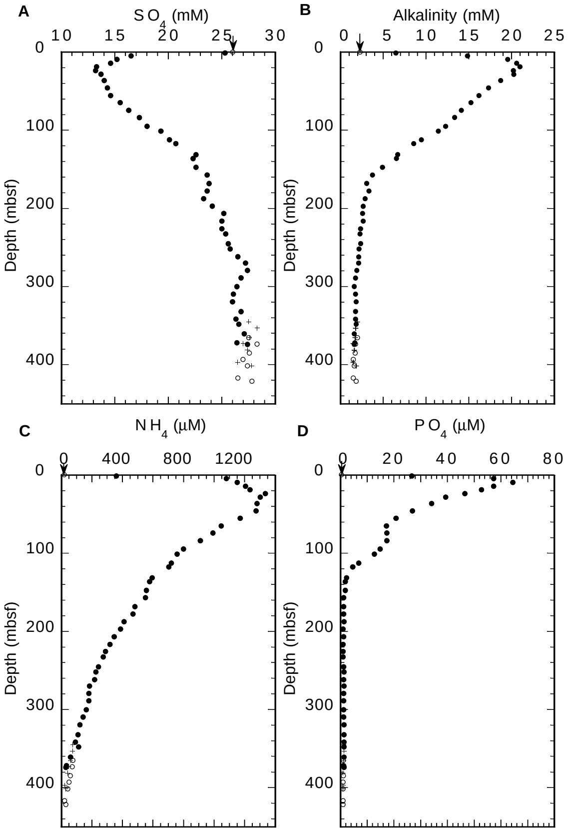

Figure 24. Concentration depth profiles of (**A**) sulfate, (**B**) alkalinity, (**C**) ammonium, and (**D**) phosphate. Arrow indicates seawater concentration.

prism sediment and siliceous ooze, with minor additions of siliceous volcanic ash and minor dilution with carbonate. Ba, Cu, and Ni are enriched at Site 1039 above levels produced by mixing prism sediment with siliceous ooze, probably reflecting the presence of barite and sulfides.

The sedimentary section entering the trench at Costa Rica is broadly similar to that entering the trench off Guatemala in several aspects that tie into the recycling of elements through subduction zones. Table 15 compares the K, Rb, Sr, and Ba in the bulk sediment column at Site 1039 with that at DSDP Site 495 off Guatemala (Plank and Langmuir, 1993). The values for Site 1039 were calculated by placing the gabbro sills at 400 mbsf. The lithologic differences between Site 1039 and DSDP Site 495 are reflected in the chemistry shown in Table 15. The hemipelagic sediments in Units U1 and U2 at Site 1039 (150 m) total 38% of the sediment column; equivalent sediments at DSDP Site 495 (97.4 m) constitute 22% of the incoming sediment column off Guatemala. K and Rb contents of the bulk sediment column are slightly higher at Site 1039 than at DSDP Site 495, reflecting the increased hemipelagic contribution to the budget. The Sr concentration at Site 1039 is commensurately lower than at DSDP Site 495. Ba in the sediment section at Site 1039 is lower than at DSDP Site 495, perhaps reflecting the generally higher sedimentation rates and greater dilution of the marine barite contribution at Site 1039 than at Site 495 (Shipboard Scientific Party, 1982).

PHYSICAL PROPERTIES

Density and Porosity

Laboratory Measurements

High core recovery and excellent core quality throughout the APC-cored Unit U1 (0–83 mbsf) enabled discrete measurements of moisture content and density to be made at a relatively high sampling rate (two samples per section) and collection of gamma-ray attenuation (GRA) density data in 2-cm sampling intervals (Fig. 1; Tables 16, 17). Within the diatomaceous ooze and sand layers of Subunit U1A (0–5.5 mbsf), wet bulk density is high relative to the underlying Subunit U1B, but bulk density rapidly decreases to a value of 1.3 g/cm^3 just above the Subunit U1A/U1B boundary. Within the diatomaceous oozes of Subunit U1B, a modest grain density increase occurs that contributes to the progressive downsection increase in wet bulk density.

In Units U2 and U3, density and porosity values show larger variability than in Unit U1. This circumstance seems to be caused primarily by the change at 97 mbsf from APC to XCB core recovery, marked by an increase in porosity and decrease in bulk density, particularly noticeable in the GRA data. These shifts in the baseline should not be considered reliable, although relative changes within the XCB section are valid. Recovered sediment is highly disturbed and sheared in the XCB cores, accompanied by a large amount of “biscuit” formation. The incursion of drill slurry between biscuits probably produces a bias toward higher moisture content and lower density measurements. In Units U2 and U3, the large effect of XCB coring on GRA densities is also evident by their poorer agreement with bulk densities measured on core specimens. In comparison, good agreement is characteristic of APC-cored Unit U1.

In Unit U2 (84–152 mbsf), specimen bulk density and porosity do not show systematic change with depth, averaging 1.5 g/cm^3 and 75%, respectively. However, within the calcareous ooze and clay of Subunit U3A (152–180 mbsf), wet bulk density decreases slightly toward the base of the layer, a trend associated with a prominent decrease in grain density from ~2.55 to 2.35 g/cm^3 (Fig. 1). This decrease can be explained by an increase in the relative proportion of biogenic silica (density = 2.1–2.2 g/cm^3) in the sediment.

Porosity and density data show a dramatic change at the top of Subunit U3B (180 mbsf). The nannofossil ooze of this unit has a fair-

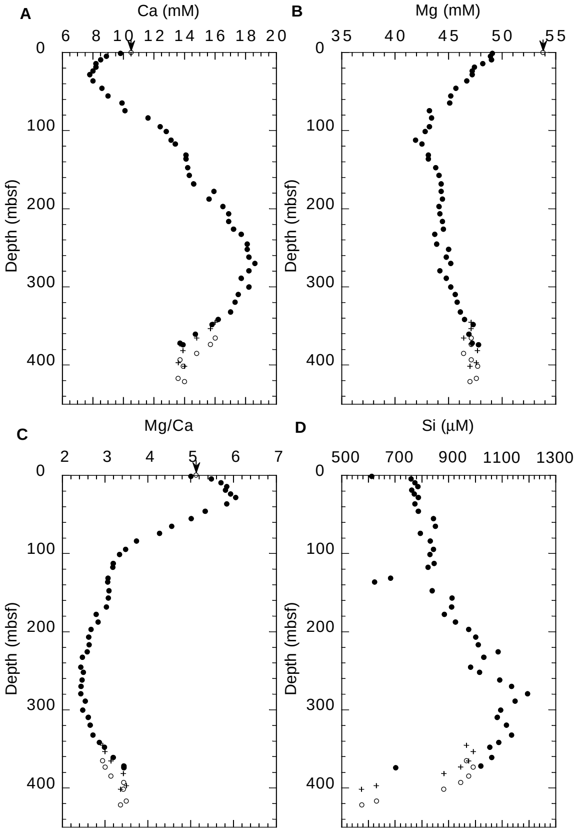

Figure 25. Concentration depth profiles of (**A**) Ca, (**B**) Mg, (**C**) Mg/Ca, and (**D**) silica. Arrow indicates seawater concentration.

ly uniform porosity of 65%–70%, contrasting sharply with the clay unit above, where the porosity is as high as 80%. At the Subunit U3A–U3B boundary, bulk density changes abruptly from 1.3 to nearly 1.6 g/cm^3, and grain density increases from less than 2.5 to more than 2.6 g/cm^3. This corresponds with a marked increase in carbonate content of the sediment and is consistent with X-ray diffraction (XRD) data, which suggest that the mineralogy in Unit U3 is dominated by calcite (density = 2.7 g/cm^3; see “Geochemistry” section, this chapter).

Within Subunit U3B at ~265–285 mbsf, anomalously low bulk density and grain density are recorded, whereas porosity shows an increase. Density reduction is consistent with a change in carbonate content, which is reduced by about half in this zone. From pore-fluid geochemistry data, a local increase in chlorinity occurs at 280 mbsf, with an even larger peak at 245 mbsf. A prominent seismic reflector is also recorded at about this depth on multichannel seismic lines that cross the area. However, no marked visible change in the lithostratigraphic section correlates with these anomalous values of physical properties. Perhaps they reflect an increase in the content of biogenic silica, which would produce a more open pore structure (allowing the storage or passage of fluids) and a lower grain density (see also resistivity and colorimetry discussions).

Toward the base of Subunit U3B and throughout underlying Subunit U3C (280–378 mbsf), grain density trends to lower values in Hole 1039B. At the base of Subunit U3C, a gabbroic intrusion was intersected. In Hole 1039C where the RCB corer was used, the intrusion was reached at a recorded depth of 422 mbsf, or 43 m deeper than at Hole 1039B. However, the grain density data in both Holes 1039B and 1039C show a trend of decreasing values with depth (also present in colorimetry data), and the two data sets match if the Hole 1039C data are shifted upward by 43 m. Therefore, it is likely that the reported depths for the intrusion at Hole 1039C are in error by approximately +40 m.

Downhole Measurements

In situ density and porosity measurements were collected by the CDN as part of the LWD downhole assembly. The results are shown in Figure 31 (see also Table 18). Downhole measurements correlate closely with core measurements (Fig. 1), although downhole densities are a little higher and porosities a little lower than the core-based values, particularly for carbonate-rich Subunit U3B below 200 mbsf. The difference may be caused by core decompaction. The downhole measurements provide a more continuous record of density and porosity variations than do the core measurements, because the in situ values are not dependent on the quality of the recovered core; for example, continuity is maintained at 97 mbsf, where the GRA densities decrease sharply downward because of the change from APC to XCB coring. Major features on the downhole profiles occur at slightly greater depths than on the core-based profiles, and the difference increases at greater depths. This effect is consistent with a deviation in the LWD drill hole (Hole 1039D) of about 8°–12° relative to Hole 1039B.

Bulk density values in the uppermost 3 m are relatively high (1.4–1.6 g/cm^3). A gradual increase from 1.3 to 1.5 g/cm^3 occurs in the interval 3–115 mbsf. Between 115 and 188 mbsf, bulk density decreases from 1.5 to 1.3 g/cm^3. An abrupt increase in bulk density to 1.7 g/cm^3 occurs at 188 mbsf, corresponding to the major lithologic boundary at 180 mbsf in Hole 1039B between Subunits U3A and U3B (see “Lithostratigraphy” section, this chapter). Bulk density fluctuates between 1.35 and 1.75 g/cm^3 over the interval 210–227 mbsf. A large negative excursion, which reaches values as low as 1.35 g/cm^3, occurs in the interval 267–290 mbsf. At 312 mbsf, a smaller negative inversion is terminated by an abrupt increase in density to 1.65 g/cm^3, below which density decreases gradually to 1.5 g/cm^3 at 352 mbsf. Below 395 mbsf, exceptionally high values (up to 2.8 g/cm^3) are explained by the gabbroic body that intrudes into the lower part of the carbonate interval.

Porosities calculated directly from the neutron log fluctuate widely throughout the logged interval. Porosity values greater than 100% were removed, and the data set was smoothed by calculating a nine-point running average. The filtered neutron porosity profile (Fig. 31) correlates well with porosity measurements on core specimens. The large decrease in porosity at 185–195 mbsf corresponds with a marked increase in downhole bulk density at 188 mbsf. Cyclical changes in porosity occur over the interval 195–285 mbsf, with rapid downward decreases between more gradual downward increases.

P-wave Velocity

The *P*-wave logger (PWL) transverse velocity (i.e., normal to the core axis) was taken at 2-cm intervals along the length of the core (Table 19; Fig. 32). These were gathered on undisturbed sediment (APC cores) and where the sediment filled the core liner. In the upper 45 m of the APC cores, longitudinal velocities (i.e., parallel with the core axis) were measured twice per section with the PWS1 probe, and transverse velocities were measured on some sections with the PWS2 probes. These velocities are nearly constant at a value of 1495 m/s, but were considered inaccurate because of poor coupling between the probes and the sediment. We have, therefore, excluded these near-surface data from our analyses. Below 45 mbsf, velocities were obtained using the PWS3 transducers (Table 20).

Velocities from the PWL decrease from 1600 to 1535 m/s in the upper 6 m of subseafloor sediment (Fig. 32A), which corresponds to the ooze and sand layers of Subunit U1A. PWL velocities increase uniformly with depth to a value of 1560 m/s at 97 mbsf. Throughout

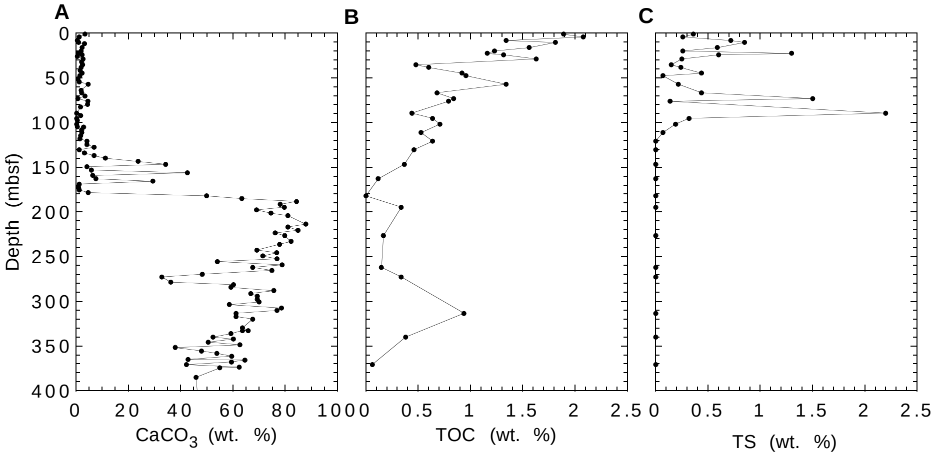

Figure 26. Concentrations of (**A**) carbonate, (**B**) total organic carbon (TOC), and (**C**) total sulfur (TS) vs. depth.

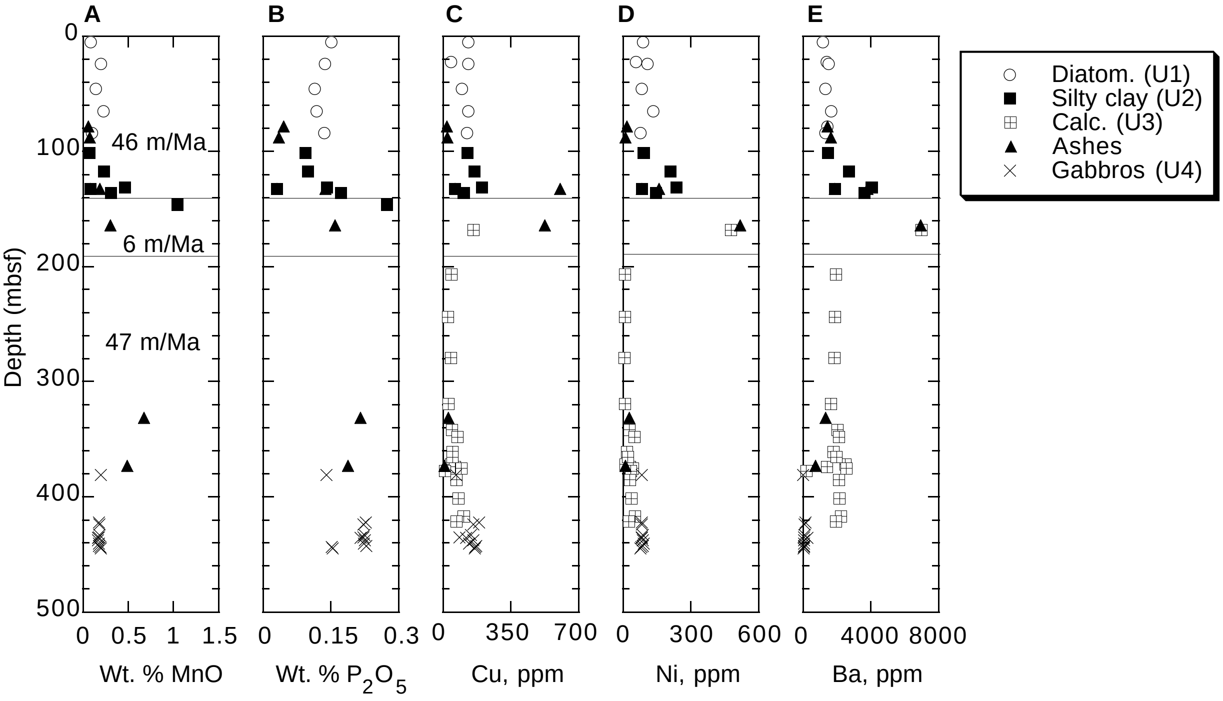

Figure 27. Concentrations of (**A**) MnO, (**B**) P_2O_5, (**C**) Cu, (**D**) Ni, and (**E**) Ba vs. depth.

Subunit U1B, PWL velocities agree fairly well with PWS3 velocities. Drilling changed from APC to XCB coring at 97 mbsf. Core quality below this depth did not permit PWL measurements, except for an interval from 295 to 330 mbsf. PWL velocities over this interval are about 40 m/s slower than the corresponding PWS3 velocities, although they both show similar trends. The lower PWL velocities probably reflect void space and layers of drilling-disturbed sediment between the core and the core liner.

PWS3 velocities increase uniformly to 1600 m/s at a depth of 300 m. No increase in velocity was observed at the top of the carbonate Subunit U3B (180 mbsf), where many other physical properties show a dramatic change (Figs. 1, 31). A slight increase in velocity gradient occurs below about 300 mbsf, which includes the interval containing Subunit U3C immediately above the gabbroic intrusion. However, velocities remain remarkably low, increasing to a value of only 1680 m/s at about 400 m depth mbsf.

Synthetic Seismograms

To integrate the detailed core-derived stratigraphic data with the seismic-reflection data, two synthetic seismograms were created for Site 1039. The first synthetic seismogram was based exclusively on a combination of physical properties data from laboratory samples. The velocity data were compiled from the PWL (0–95 mbsf) and from individual samples that were measured with the PWS3 contact transducers (96–189 mbsf and 240–380 mbsf) as described above (Fig. 32A). A velocity function was linearly interpolated between data points at 190 and 240 mbsf to bridge a data gap. Wet bulk den-

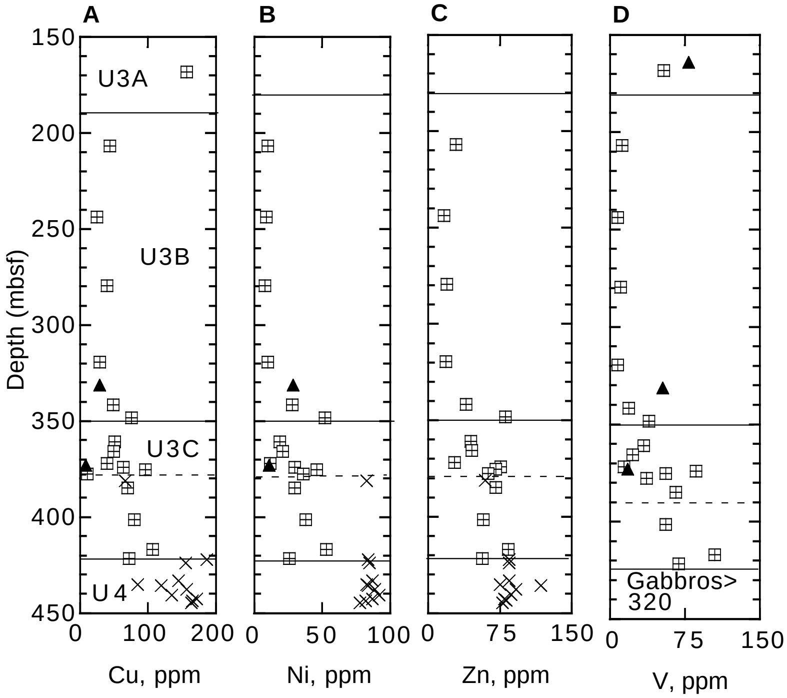

Figure 28. Concentrations of (**A**) Cu, (**B**) Ni, (**C**) Zn, and (**D**) V vs. depth in the calcareous sediments.

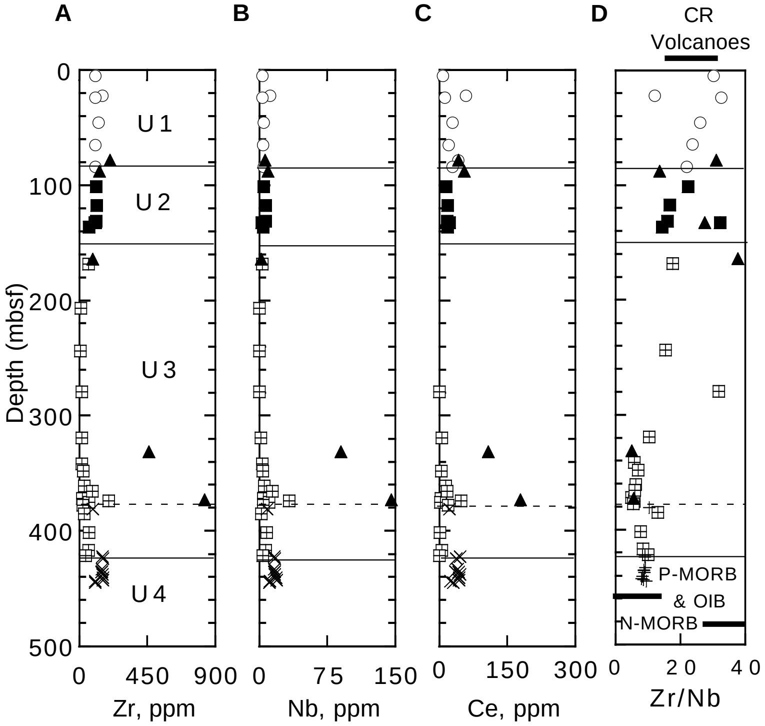

Figure 29. Concentrations of (**A**) Zr, (**B**) Nb, (**C**) Ce, and (**D**) Zr/Nb vs. depth.

sity data for the first synthetic seismogram were taken solely from the moisture and density laboratory measurements (Fig. 1). All velocity and density data were resampled at a 2-m-depth sample interval before computing impedance and reflectivity series. The resulting acoustic impedance function is shown in Figure 32B. A wavelet derived from the seafloor reflection was then convolved with the computed reflectivity series. The resulting synthetic traces match the seismic data from Line CR-20 remarkably well (Fig. 33, left). In particular, a good match is obtained for reflections from the top of calcareous Subunit U3B, and from the top and base of the thin low-density zone (~265–285 mbsf) within Subunit U3B. A few obvious differences occur in amplitude, and the computed traveltime is about 15 ms too great with respect to the top of the gabbro intrusion (Unit U4) recorded on the reflection profile.

The second synthetic seismogram created for Site 1039 uses the same velocity data described above, but uses bulk density data from the LWD data set (Fig. 33, right). These synthetic data match the seismic data somewhat better than the first set of synthetic data, particu-

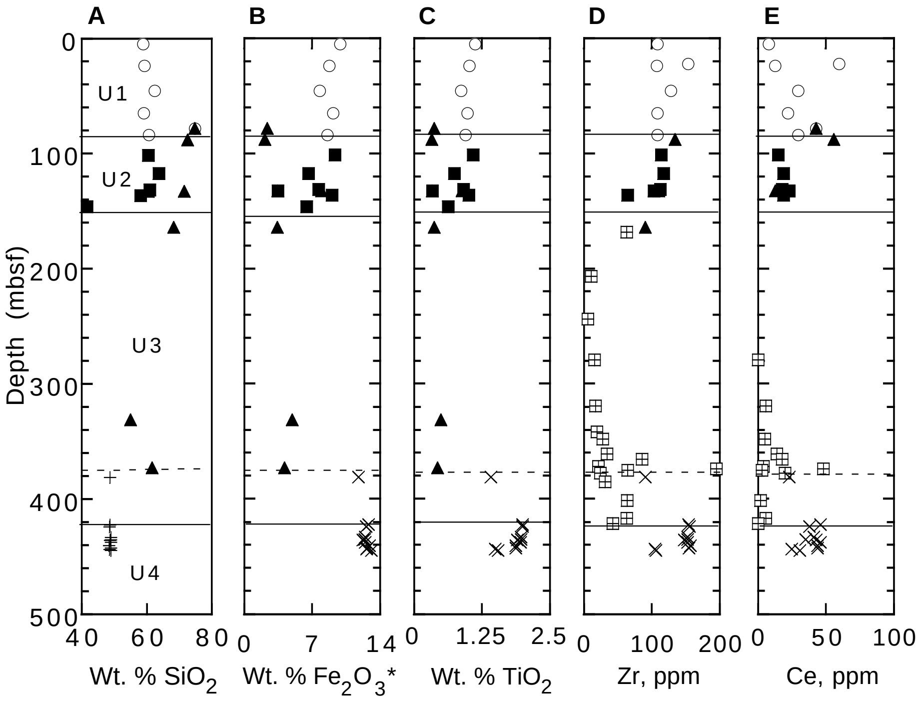

Figure 30. Concentrations of (**A**) SiO_2, (**B**) Fe_2O_3*, (**C**) TiO_2, (**D**) Zr, and (**E**) Ce vs. depth. Fe_2O_3* = total iron as Fe_2O_3.

Table 15. Composition of the bulk sediment column at Site 1039, Costa Rica and DSDP Site 495, Guatemala.

Unit	Thickness (m)	K_2O (wt%)	Ba (ppm)	Sr (ppm)	Rb (ppm)
Guatemala*					
Hemipelagic	97.4	1.84	3941	336	40.8
Carbonate	340.6	0.18	2145	1504	4.3
Total:	437	0.67	3250	1237	21.8
Costa Rica: Site 1039					
Unit U1 (hemipelagic)	84	2.43	1401	369	47.4
Unit U2 (hemipelagic)	66	2.40	2753	276	50
Unit U3 (carbonate)	250	0.18*	2325	999	8.2
Total:	400	1.02	2202	726	23.3

Note: * = from Plank and Langmuir (1993).

larly in the thick Unit U3, where relative amplitude and the seismic character are both reasonably well matched by the synthetic data. This improvement, using a presumably superior density determination, suggests that the acoustic impedance profile here is strongly dependent on bulk density variation, perhaps to a greater extent than on velocity variation.

Based on the depth to time relationship derived during the reflectivity series computation with adjustments indicated by the seismic-synthetic mismatches, the lithostratigraphic boundaries are tied to the seismic-reflection data as indicated in the center of the figure (Fig. 33). The computed traveltime matches well into Unit U3, but becomes significantly overestimated toward the bottom of the hole. The time discrepancy apparent at the top of Unit U4 indicates a velocity underestimate of ~100 m/s if calculated over the interval from 180 to 380 mbsf. This ~6% error is likely attributable to core expansion at surface temperature and pressure, although it is far less than errors reported in studies of other carbonate-rich sediments. For example, the empirical correction of Urmos et al. (1993), a depth-dependent, exponential relation, predicts a core velocity underestimate of ~311 m/s at 300 mbsf based on velocities of pelagic carbonate beds of the Ontong Java Plateau. The relatively low error at Site 1039 likely indicates a minimum of disturbance in the cores caused by drilling or the measurement process.

Magnetic Susceptibility

Magnetic susceptibility values (Fig. 1; Table 21) decrease rapidly in the upper 5.5 mbsf, corresponding to the diatomaceous ooze and sand layers of Subunit U1A. In Subunit U1B, magnetic susceptibility is dominated by large excursions to higher values corresponding to numerous ash layers. These excursions correlate with positive peaks in the GRA bulk density values (Fig. 1). Magnetic susceptibility is uniform within Unit U2, although its baseline value is approximately two-thirds that of Unit U1. Excursions to high readings related to ash layers are also recorded in Unit U2, but the magnitudes of susceptibility reached are much smaller than in Unit U1.

A prominent feature in the magnetic susceptibility readings is the sudden decrease to near-zero values within Subunit U3B, recording the near absence of magnetic material in the calcareous ooze of this layer. However, when displayed at an expanded plotting scale, the data of Subunit U3B show an increase in the number of positive excursions in the depth interval from 265 to 285 mbsf, where anomalies are also recorded in bulk density, grain density, porosity, electrical resistivity, thermal conductivity, and other properties (Fig. 1).

Vane Shear Strength

The automated vane shear strength device was used to determine undrained peak and residual shear strength in the more cohesive, uncemented stratigraphic units. Drilling disturbance precluded shear measurements, except, rarely, in XCB cores. As a consequence, data from lithologic Unit U3 and the lower part of Unit U2 are lacking. RCB cores collected from Hole 1039C are of better quality, and some measurements could be made from near the base of calcareous Unit U3 (Table 22).

Figure 34A shows the relation between shear strength and depth for Holes 1039A and 1039B. The depth interval represents the whole of Unit U1 and the upper part of Unit U2. The shear strength increases linearly with depth from 6 to 44 kPa until ~30 mbsf, below which

Table 16. Gamma-ray attenuation (GRA) bulk density data for Site 1039.

Leg	Site	Hole	Core	Type	Section	Top (cm)	Bottom (cm)	Depth (mbsf)	Density (g/cm^3)	Counts	Actual daq (s)	Core diameter (cm)
170	1039	A	1	H	1	3.7	3.7	0.04	1.329	1.10E+05	5	6.7
170	1039	A	1	H	1	4.7	4.7	0.05	1.346	1.09E+05	5	6.7
170	1039	A	1	H	1	5.7	5.7	0.06	1.25	1.16E+05	5	6.7
170	1039	A	1	H	1	6.7	6.7	0.07	1.332	1.10E+05	5	6.7
170	1039	A	1	H	1	7.7	7.7	0.08	1.36	1.09E+05	5	6.7
170	1039	A	1	H	1	8.7	8.7	0.09	1.362	1.08E+05	5	6.7
170	1039	A	1	H	1	9.7	9.7	0.1	1.33	1.10E+05	5	6.7
170	1039	A	1	H	1	10.7	10.7	0.11	1.315	1.11E+05	5	6.7
170	1039	A	1	H	1	11.7	11.7	0.12	1.309	1.12E+05	5	6.7
170	1039	A	1	H	1	12.7	12.7	0.13	1.309	1.12E+05	5	6.7

Note: daq = data acquisition.

This is a sample of the table that appears on the volume CD-ROM.

Table 17. Moisture and density data, and calculated phase relationships from discrete core specimens, Site 1039.

Leg	Site	Hole	Core	Type	Section	Top (cm)	Bottom (cm)	Depth (mbsf)	Sample no.	Beaker-ID	Wet volume (g/cm^3)	Dry volume (g/cm^3)	Wet mass (g)	Dry mass (g)	Beaker mass (g)	Beaker volume (g/cm^3)
170	1039	A	1	H	1	35	37	0.35	1	299	11.65	6.66	20.79	14.95	8.162	3.677
170	1039	A	1	H	1	36	38	0.36	2	174	6.13	6.409	19.78	14.53	7.976	3.593
170	1039	A	1	H	1	119	121	1.19	0	177	10.55	6.294	18.19	14.19	8.195	3.691
170	1039	A	1	H	1	120	122	1.2	2	298	6.86	7.172	22.09	16.09	8.08	3.64
170	1039	A	1	H	2	35	37	1.85	1	63	10.29	6.158	18.39	13.85	8.014	3.61
170	1039	A	1	H	2	36	38	1.86	2	10	5.99	6.262	18.59	14.09	7.887	3.553
170	1039	A	1	H	2	119	121	2.69	1	195	10.01	5.865	18.45	13.77	7.977	3.593
170	1039	A	1	H	2	120	122	2.7	2	54	6.13	6.409	19.07	14.39	8.294	3.736
170	1039	A	1	H	3	35	37	3.35	1	5	12.13	6.126	20.64	14.27	8.027	3.616
170	1039	A	1	H	3	36	38	3.36	2	72	6.2	6.482	20.32	14.41	8.048	3.625

Table 17 (continued).

Leg	Site	Hole	Core	Type	Section	Top (cm)	Bottom (cm)	Depth (mbsf)	Water content (wet)	Water content (dry)	Wet bulk density (g/cm^3)	Grain density (g/cm^3)	Porosity (%)	Void ratio	Dry bulk density (g/cm^3)
170	1039	A	1	H	1	35	37	0.35	0.479	0.92	1.436	2.28	67.187	2.048	0.754
170	1039	A	1	H	1	36	38	0.36	0.461	0.855	1.468	2.333	66.065	1.947	0.798
170	1039	A	1	H	1	119	121	1.19	0.415	0.708	1.518	2.308	61.48	1.596	0.895
170	1039	A	1	H	1	120	122	1.2	0.444	0.798	1.474	2.271	63.881	1.769	0.826
170	1039	A	1	H	2	35	37	1.85	0.453	0.829	1.469	2.295	65.01	1.858	0.809
170	1039	A	1	H	2	36	38	1.86	0.436	0.772	1.489	2.293	63.344	1.728	0.847
170	1039	A	1	H	2	119	121	2.69	0.463	0.862	1.512	2.564	68.338	2.158	0.818
170	1039	A	1	H	2	120	122	2.7	0.45	0.818	1.47	2.285	64.601	1.825	0.815
170	1039	A	1	H	3	35	37	3.35	0.523	1.097	1.425	2.501	72.829	2.68	0.685
170	1039	A	1	H	3	36	38	3.36	0.499	0.996	1.405	2.23	68.434	2.168	0.709

This is a sample of the table that appears on the volume CD-ROM.

a more gradual increase in shear strength occurs with depth, along with a greater scatter of the measured values. The increase in shear strength correlates with changes in other physical properties (i.e., decrease of porosity and water content and increase of bulk density). The greater scatter of the data below 30 mbsf is probably attributable to lithologic variations.

An estimate of the state of sediment consolidation can be made by comparison of the range of strengths measured to those of a gravimetrically, or "normally" consolidated sedimentary column, expressed as the ratio of measured undrained strength (S_u) and the overburden stress P'_0. The overburden pressure can be estimated from bulk density and overlying sediment thickness, assuming hydrostatic pore-fluid pressures. The S_u/P'_0 values (Fig. 34B) decrease rapidly downhole within the first 20 m from 0.34 to 0.07, after which the ratio remains relatively constant. These ratios are lower than expected for normally consolidated sediments ($S_u/P'_0 = 0.25$). This circumstance may indicate significant underconsolidation (i.e., retarded dewatering of the sediment in response to sediment deposition). Alternatively, these sediments may exhibit anomalously low interparticle friction or cohesion during undrained shear. Such weakness could arise from the high diatom content, creating a framework not capable of sustaining any significant amount of shear stress.

Electrical Resistivity

Laboratory Measurements

Electrical resistivity measurements were collected at a spacing of about one per section in APC cores and less-disturbed XCB cores.

The electrical resistivity was found to be low throughout Site 1039 (Table 23; Fig. 35), corresponding to a formation factor (calculated assuming constant pore-water salinity of 35) in the range 1.25–2.8 (Fig. 35A). The low resistivities can be explained by the uniformly high porosity of the sediment in all three lithologic units (Fig. 1). Unit U1 shows a systematic increase in formation factor with depth, below which a slower increase with depth and a greater scatter in the data occurs. These relations are believed to correspond to minor variations in lithology and porosity within Units U2 and U3, and to greater disturbance in the cores recovered by the XCB. A decrease in resistivity between ~270 and 280 mbsf corresponds with changes in other physical properties (i.e., increase in porosity, decrease in bulk

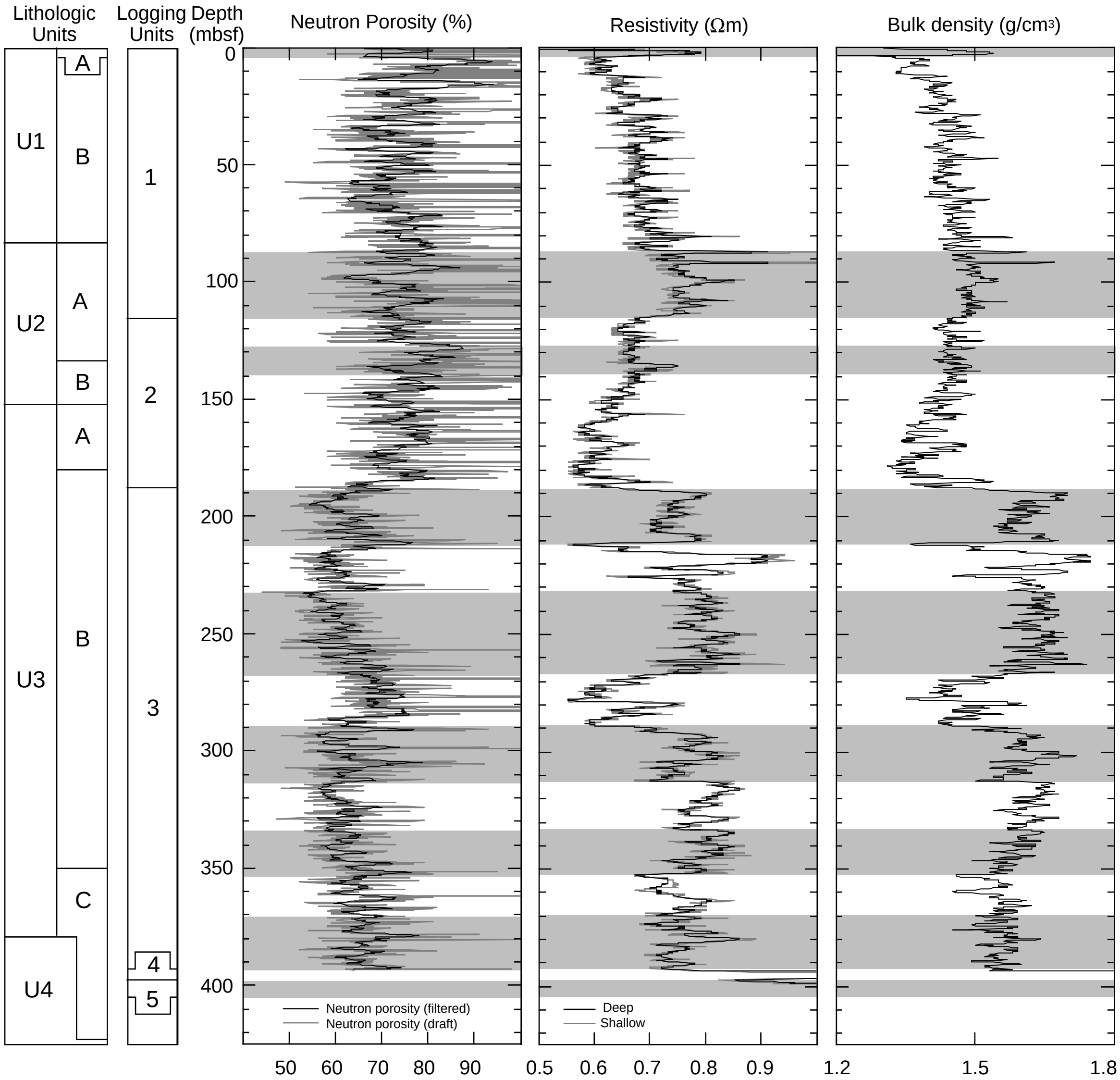

Figure 31. Summary of LWD results showing logging units and lithologic units at Site 1039. SGR = total spectral gamma ray, CGR = computed spectral gamma ray.

density), although the trend may partly be explained by a change in pore-fluid chemistry (see "Geochemistry" section, this chapter).

Downhole Measurements

In situ resistivity measurements were collected using the CDR in Hole 1039D. The deep and shallow resistivity logs shown in Figure 31 show very similar trends and amplitudes, indicating good hole conditions. Computed formation factors based on constant pore-water salinity of 35 are shown in Figure 35B. The computed formation factors range from 1.7 to 3 and show the same trends as the resistivity variations, which are detailed below.

Resistivity values in the uppermost 3 m show relatively high values of 0.7–0.8 Ωm. Mimicking the bulk density log, the values drop off rapidly and then increase gradually from 0.6 to 0.70 Ωm over the interval 3–88 mbsf. Together, these data indicate that the uppermost part of the sedimentary section is lithologically distinct or may be overconsolidated. Between 88 and 115 mbsf, resistivity remains around 0.8 Ωm, and a general downward decrease from 0.65 to 0.55 Ωm occurs in the interval 115–188 mbsf. At this depth, an abrupt change in resistivity occurs, which corresponds to the boundary between lithologic Subunits U3A and U3B (in Hole 1039B this occurs at 180 mbsf; see "Lithostratigraphy and Structures" section, this chapter). The resistivity values in the interval 188–395 mbsf lie mainly between 0.7 and 0.85 Ωm. However, the interval 210–227 mbsf displays wide fluctuations between 0.55 and 0.9 Ωm, and a large negative anomaly down to 0.55 Ωm occurs between 267 and 292 mbsf. The abrupt downward increases in resistivity at 278, 290, 312, and 332 mbsf, produce a "saw-tooth" profile in the log.

The interval 395–398 mbsf, corresponding to the gabbro intrusion, shows exceptionally high resistivities (up to 20 Ωm). Below this highly resistive layer, the values range from 0.9 to 1.2 Ωm, which is significantly higher than in the sediment above.

Thermal Conductivity

Using the full-space needle probe method, thermal conductivity (TC) data were collected on unsplit cores at three or four locations per core (Table 24). Measurements made on cored intervals disturbed by drilling were subsequently discarded.

Thermal conductivity results mirror certain changes in lithology and porosity. Values are close to those for seawater and are an ex-

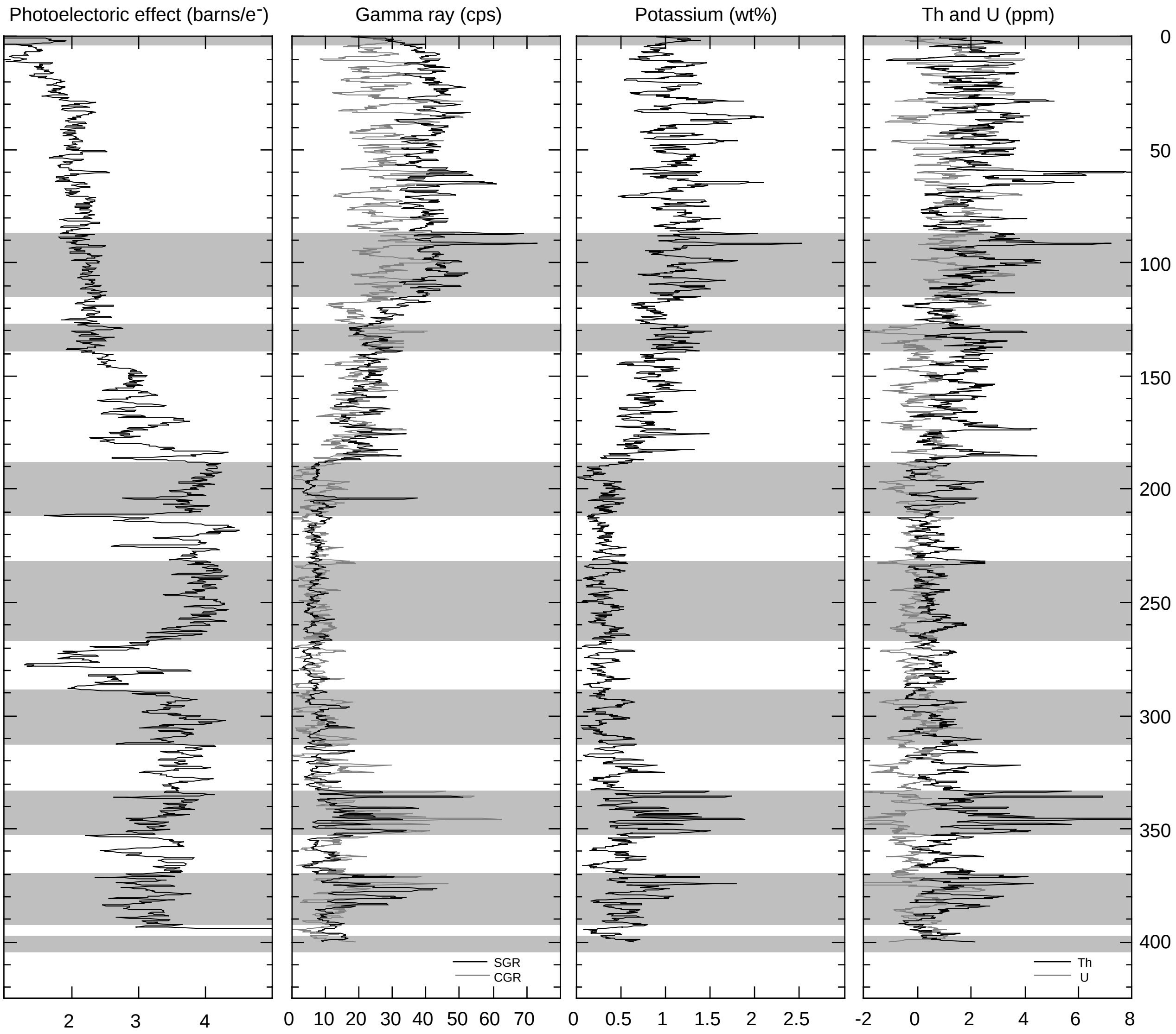

Figure 31 (continued).

pression of the high porosity and low quartz content of the sediment. The diatomaceous ooze and ash-rich silty clay of Units U1 and U2 display the lowest TC. Values range from 0.7 to 0.9 W/(m·K) and change little with depth (Fig. 35). This observation is consistent with the known low thermal conductivity of biogenic opal and volcanic glass. Between 196 and 220 mbsf just below the Subunit U3A/U3B boundary, thermal conductivity increases markedly to 1.2 W/(m·K) in association with the increase in carbonate content. From 220 to 420 mbsf, a gradual decrease in TC occurs to values as low as 0.9 W/(m·K). Between ~255 and 280 mbsf, thermal conductivity drops to between 0.7 and 0.75 W/(m·K). This is a noticeable negative excursion in the downhole trend of decreasing TC, but does not correspond with a major change in the recorded lithostratigraphy (see "Lithostratigraphy and Structures" section, this chapter). This relation is associated with an increase in porosity, decrease in bulk and grain density, reduction in carbonate content, and increase in interstitial pore-water chlorinity.

Heat Flow

Equilibrium temperatures obtained from the APC temperature tool, the WSTP, and the DVTP are shown in Table 25 and Figure 36, and as a function of depth in Figure 37A and Table 25. The average geothermal gradient at Site 1039 is 9.6°C/km. The errors were determined subjectively, based on the stability of the equilibration record and tool performance.

Heat flow is estimated from the in situ equilibrium temperature measurements and the thermal conductivity values measured onboard (Fig. 35C). The slope of the temperature vs. cumulative thermal resistance curve (Fig. 37B) yields a direct measure of heat flow, which averages 8.4 mW/m^2 between 87.5 and 344.0 mbsf. The heat flow does not appear to change with depth and is exceptionally low. Estimated heat flow at Site 1039 is consistent with the lowest value determined by the pre-cruise heat-flow survey conducted at the same location (8 mW/m^2; Langseth and Silver, 1996).

Colorimetry

The lightness component (L*) of the sediment drilled at Site 1039 increases from around 25% at the seafloor to 75% at about 250 mbsf, and then decreases to 48% at the base of Holes 1039B and 1039C (Fig. 1). The increase in lightness is progressive from the seafloor (Subunit U1A) down to 170 m (within Subunit U3A), where a sharp 5% increase, followed immediately by a 10% decrease (all within

Table 18. Shipboard composite logging-while-drilling data from Hole 1039D.

Depth (mbrf)	Depth (mbsf)	ROP5 (m/hr)	ATR (Ωm)	PSR (Ωm)	RTIM (s)	GTIM (s)	GR (GAPI)	Thor (ppm)	Uran (ppm)	Pota (%)
4363.06	0.06	141.06	0.45	0.48	140	500	27.37	0.82	–0.15	0.9
4363.21	0.21	51.81	0.44	0.47	150	510	37.43	0.81	0.12	1.11
4363.36	0.36	51.19	0.52	0.54	150	510	41.35	1.58	–0.09	1.21
4363.52	0.52	47.08	0.67	0.69	150	510	43.31	1.8	–0.05	1.24
4363.67	0.67	45.42	0.55	0.57	190	530	43.57	1.62	–0.02	1.28
4363.82	0.82	43.05	0.75	0.74	200	540	44.87	1.25	0.58	1.17
4363.97	0.97	43.03	0.74	0.76	230	550	42.78	1.17	0.6	1.12
4364.13	1.13	44.51	0.77	0.77	240	560	42.78	1.24	0.49	1.15
4364.28	1.28	42.74	0.76	0.76	250	590	42.26	1.82	0.13	1.18
4364.43	1.43	43.06	0.76	0.71	260	600	43.18	2.23	–0.52	1.39

Note: ROP5 = 5 ft averaged rate of penetration, ATR = attenuation resistivity, PSR = phase shift resistivity, RTIM = resistivity time after bit, GTIM = gamma-ray time after bit, GR = gamma ray, Thor = thorium, Uran = uranium, Pota = potassium, CGR = computed gamma ray (thorium + potassium), SGR = total gamma ray, DTAB = density time after bit, PEF = photoelectric factor, DRHO = bulk density correction, DC_A = differential caliper, ROMT = rotationally processed density, NTAB = neutron time after bit, and TNPH = thermal neutron porosity.

Table 18 (continued).

Depth (mbrf)	Depth (mbsf)	CGR (cps)	SGR (cps)	DTAB (s)	PEF (barnes/e$^-$)	DRHO (g/cm^3)	DC_A (in)	ROMT (g/cm^3)	NTAB (s)	TNPH (v/v)
4363.06	0.06	18.92	17.57	1200	0.95	–0.01	1.62	1.3	1520	0.66
4363.21	0.21	22.53	23.6	1230	1.27	–0.01	1.76	1.35	1540	0.7
4363.36	0.36	26.96	26.2	1240	1.49	–0.01	1.7	1.4	1550	0.72
4363.52	0.52	28.31	27.86	1260	1.6	–0.01	1.65	1.44	1570	0.66
4363.67	0.67	28.44	28.22	1290	1.66	–0.01	1.61	1.44	1590	0.7
4363.82	0.82	25.17	30.28	1300	1.7	–0.01	1.55	1.44	1600	0.7
4363.97	0.97	23.93	29.29	1320	1.69	–0.01	1.45	1.46	1610	0.97
4364.13	1.13	24.75	29.09	1330	1.65	0	1.39	1.48	2190	0.91
4364.28	1.28	27.23	28.41	1360	1.65	0	1.39	1.48	2190	1.34
4364.43	1.43	32.46	27.82	1360	1.75	0	1.41	1.49	2200	0.76

This is a sample of the table that appears on the volume CD-ROM.

Table 19. *P*-wave velocities obtained from the PWL using the MST on unsplit cores from Site 1039.

Leg	Site	Hole	Core	Type	Section	Top (cm)	Bottom (cm)	Depth (mbsf)	Velocity (m/s)	Meas. separation mean (mV)	Meas. separation SD (mV)	Meas. time mean	Meas. time SD	Acoustic level mean	Attempted daqs	Valid daqs	Liner thinkness (mm)
170	1039	B	1	H	1	7.3	7.3	0.07	1562.3	200	0	50.15	0.014	184	25	25	2.54
170	1039	B	1	H	1	9.3	9.3	0.09	1561	199	0	50.12	0.025	203	25	25	2.54
170	1039	B	1	H	1	11.3	11.3	0.11	1572	196	0	49.97	0.025	214	25	25	2.54
170	1039	B	1	H	1	13.3	13.3	0.13	1598.1	196	0	49.67	0.025	20	25	25	2.54
170	1039	B	1	H	1	15.3	15.3	0.15	1565.7	196	0	48.98	0.025	185	25	25	2.54
170	1039	B	1	H	1	17.3	17.3	0.17	1563.5	196	0	49.84	0.016	248	25	25	2.54
170	1039	B	1	H	1	19.3	19.3	0.19	1566.8	195	0	49.84	0.037	239	25	25	2.54
170	1039	B	1	H	1	21.3	21.3	0.21	1558.7	195	0	49.75	0.014	234	25	25	2.54
170	1039	B	1	H	1	23.3	23.3	0.23	1560.9	195	0	49.97	0.025	245	0	25	2.54
170	1039	B	1	H	1	25.3	25.3	0.25	1584.7	195	0	49.91	0.018	27	25	25	2.54

Note: Meas. = measured, SD = standard deviation, and daq = data acquisition.

This is a sample of the table that appears on the volume CD-ROM.

Subunit U3A), precedes an abrupt increase of over 25% (Subunit U3B). Lightness stays relatively constant for about 85 m, with just a relative low at 280 mbsf (within Subunit U3B), and then drops with broad relative highs at 310 mbsf (Subunit U3C) and below 370 mbsf (Subunit U3C). These variations in lightness with depth correlate with the carbonate concentrations above 15% (all of Unit U3; Fig. 1).

Given the steady increase in lightness with depth across Units U1 and U2, it is not possible to differentiate these units based solely on this property. The red/blue (a*/–b*) ratio, however, shows a remarkable difference between these units (Fig. 1), ranging from 0.34 to 0.44 in Unit U1, whereas it is around 0.66 for Unit U2. Unit U3 has red/blue values below 0.22, whereas the intrusive Unit U4 has the highest mean value of 0.85. A comparison of L* and (a*/–b*) values for each unit is given in Figure 38A.

Mean reflectance vs. wavelength for each lithostratigraphic unit shows an increase from Unit U1 to Unit U3, with Subunit U1A being the least reflective at all wavelengths (Fig. 38B). As in the case of lightness, Subunit U3B shows the highest values, and Subunit U3C lies somewhere in between Subunits U3A and U3B. The reflectance of Unit U4 is higher than Subunit U3A, but lower than Subunit U3C. In Figure 38B, Subunits U1B and U2A are almost indistinguishable and emphasize the contribution of the chromaticity ratio (a*/–b*) in the color characterization of these units. Over the wavelength window shown in Figure 38B, Unit U4 stands out with the flattest spectrum, and Subunit U3B has the highest dependence of reflectance with wavelength.

Natural Gamma Ray and Photoelectric Effect

In situ natural gamma-ray measurements were collected by CDR, and the PEF was measured by CDN in Hole 1039D (Figs. 1, 31). Both logs respond to mineralogic composition and therefore indicate

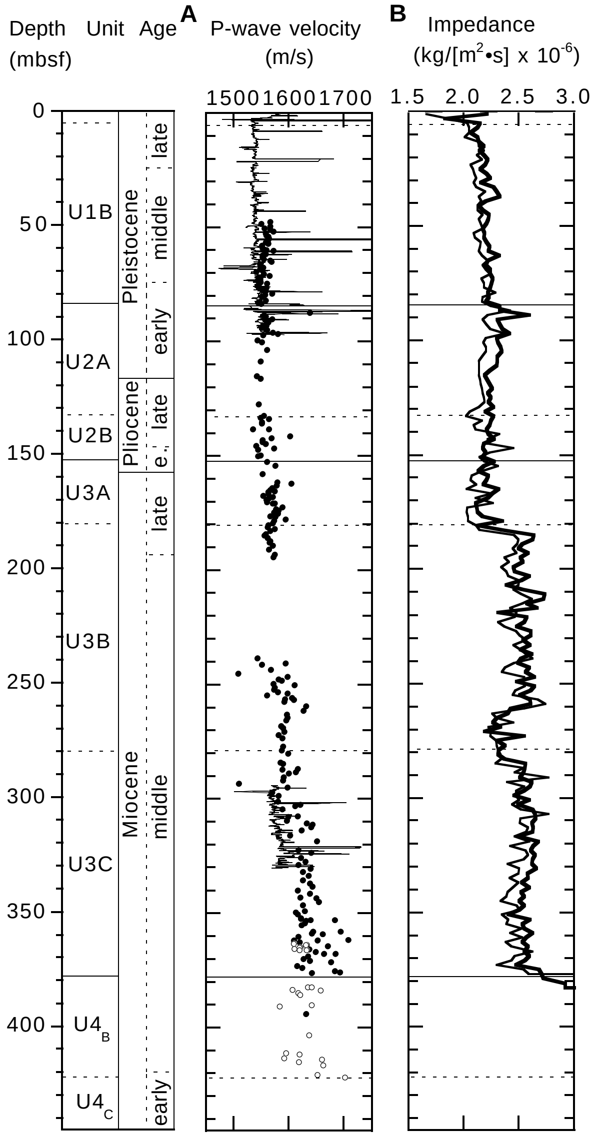

Figure 32. **A.** Acoustic compressional-wave velocity, measured directly on unsplit cores by the PWL on the MST (smooth line) and on split cores by the PWS3 (solid circles = Hole 1039B; open circles = Hole 1039C). **B.** Acoustic impedance, or the product of *P*-wave velocity and bulk density. Velocity (Fig. 31A) and GRA/core-specimen density (Fig. 1) were resampled at an interval of 2 m (continuous line), and LWD derived densities were resampled (broken line) for impedance calculations.

Table 20. *P*-wave velocities obtained from the PWS3 on split cores from Site 1039.

Leg	Site	Hole	Core	Type	Section	Top (cm)	Bottom (cm)	Depth (mbsf)	Velocity (m/s)
170	1039	B	6	H	6	120	120	48.7	1549.7
170	1039	B	6	H	6	35.2	35.2	47.85	1566.6
170	1039	B	7	H	1	120.2	35.2	50.7	1555.9
170	1039	B	7	H	1	35.2	35.2	49.85	1566.7
170	1039	B	7	H	2	102	102	52.02	1571.9
170	1039	B	7	H	2	35	35	51.35	1566.1
170	1039	B	7	H	3	125	125	53.75	1558.6
170	1039	B	7	H	3	44.7	44.7	52.95	1558
170	1039	B	7	H	4	120.1	120.1	55.2	1564.1
170	1039	B	7	H	4	33	33	54.33	1562.3

This is a sample of the table that appears on the volume CD-ROM.

changes in lithology. The profile of the total spectral gamma ray shows a trend similar to the magnetic susceptibility profile throughout the section.

Values of total spectral gamma ray show 30–50 counts per second (cps), 15–30 cps, 5–20 cps, and 5–50 cps in intervals 0–115, 115–188, 188–332, and 332–404 mbsf, respectively. Yields of the uranium spectrometry distinctively decrease at 127 mbsf. Most of the strong peaks of the gamma-ray profile can be correlated to ash layers. The total gamma-ray peak of 70 cps at 87 mbsf coincides with the thick ash layer at the lithologic Unit U1/U2 boundary. The increasing frequency of the gamma-ray peaks below 300 mbsf coincides with the increasing abundance of ash layers (see "Lithostratigraphy and Structures" section, this chapter).

Quartz and opal have PEF's of 1.8, whereas calcite has a PEF of 5.1, and most rock-forming minerals and clays have intermediate values. Significant changes in the PEF, indicative of a change in lithology, occur over the intervals 138–188, 210–231, and 267–288 mbsf. The PEF profile shows a similar trend to that of the carbonate profile (see "Geochemistry" section, this chapter) and the colorimetry (this section). In the interval 138–188 mbsf, PEF increases from 2 to 4, which coincides with the increasing content of carbonate in lithologic Subunit U3A. In the intervals 210–227 and 267–292 mbsf, PEF decreases to values as low as 1.5, which is best explained by an increased abundance of biogenic opal (see "Lithostratigraphy and Structures" section, this chapter).

Logging Units and Correlation with Lithostratigraphy

LWD logs at Hole 1039D show responses to several geologic features. Bulk density and resistivity logs are particularly sensitive to changes in porosity and thus compaction state, whereas gamma-ray and PEF logs tend to be more responsive to changes in lithology. The logged records in Hole 1039D are divided into five logging units on the basis of obvious changes in the log responses (Fig. 31).

Logging Unit 1 (0–115 mbsf) is characterized by relatively high total spectral gamma ray. The base of logging Unit 1 at 115 mbsf is clearly recognized by changes in bulk density, resistivity, and total spectral gamma ray (Fig. 31). However, this depth does not correspond to an identified lithologic boundary. Within this unit, the interval 0–3 mbsf is characterized by relatively high resistivity and bulk density, and coincides with lithologic Subunit U1A ("turbidite" zone). The interval 3–88 mbsf is characterized by gradual increase of resistivity and bulk density with depth, which coincides with lithologic Subunit U1B (diatomaceous ooze). Strong peaks in gamma-ray, resistivity, and bulk density logs occur at the base of the interval (88 mbsf) and correspond to the thick ash layer at the boundary between lithologic Units U1/U2 at 88 mbsf.

Logging Unit 2 (115–188 mbsf) is delineated by an abrupt change in resistivity at 115 mbsf and by marked changes in every log at 188 mbsf. This unit includes two minor internal changes in log response; a decrease in uranium content at 127 mbsf, and an increase in PEF at 138 mbsf, which can be correlated to the lithologic Subunit U2A/U2B boundary (base of silty clay). The interval 138–188 mbsf is characterized by intermediate values of total spectral gamma ray, gradual decreases in resistivity and bulk density, and an increase in PEF that is consistent with the increasing calcium carbonate (see "Geochemistry" section, this chapter).

Logging Unit 3 (188–395 mbsf) is characterized by low background values in spectral gamma ray, which corresponds with pelagic sediments. Logging Unit 3 is correlated with lithologic Subunits U3B and U3C. The interval 188–332 mbsf is characterized by low and constant values of total spectral gamma ray. However, resistivity, bulk density, and PEF values show strong fluctuations in the interval 210–227 mbsf, a negative excursion in the interval 267–288 mbsf, and an abrupt increase at 312 mbsf. The low values reflect a decrease in carbonate and an increase in biogenic silica (see "Geochem-

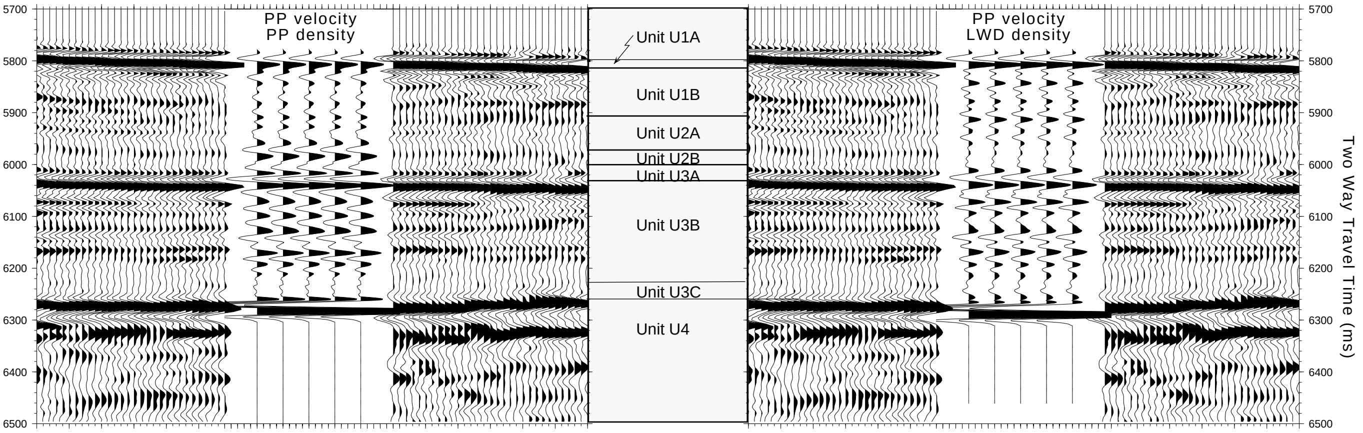

Figure 33. Portion of seismic Line CR-20 with synthetic traces inserted at the location of Site 1039. The left-side synthetic trace is derived exclusively from the laboratory-measured physical properties data. The lithostratigraphic relation to the seismic data provided by the synthetic traces is also indicated. Additional synthetic data created using the LWD bulk density and the same velocity data are shown on the right side of the figure. Real and synthetic data are displayed in two way traveltime (ms).

Table 21. Magnetic susceptibility values obtained on unsplit cores using the MST, Site 1039.

Leg	Site	Hole	Core	Type	Section	Top (cm)	Bottom (cm)	Depth (mbsf)	Relative, drift corr. sus.	Mean relative mag. sus.	Actual daq period (s)	Core diameter (cm)	Elapsed time (s)	Drift correction
170	1039	A	1	H	1	3	3	0.03	337	337	5	6.7	8,002	0
170	1039	A	1	H	1	5	5	0.05	358	358	5	6.7	11,406	0
170	1039	A	1	H	1	7	7	0.07	355.9	355.8	5	6.7	14,805	–0.1
170	1039	A	1	H	1	9	9	0.09	307.3	307.2	5	6.7	18,197	–0.1
170	1039	A	1	H	1	11	11	0.11	252.7	252.6	5	6.7	21,598	–0.1
170	1039	A	1	H	1	13	13	0.13	209.9	209.8	5	6.7	24,996	–0.1
170	1039	A	1	H	1	15	15	0.15	188.5	188.4	5	6.7	28,398	–0.1
170	1039	A	1	H	1	17	17	0.17	182.7	182.6	5	6.7	31,805	–0.1
170	1039	A	1	H	1	19	19	0.19	210.1	210	5	6.7	35,199	–0.1
170	1039	A	1	H	1	21	21	0.21	290.7	290.6	5	6.7	38,587	–0.1

Note: Corr. = corrected, sus. = susceptibility, mag. = magnetic, and daq = data acquisition.

This is a sample of the table that appears on the volume CD-ROM.

Table 22. Vane shear strength data for Holes 1039A and 1039B.

Leg	Site	Hole	Core	Type	Section	Top (cm)	Bottom (cm)	Depth (mbsf)	Peak undrained shear strength (kPa)	Undrained residual strength (kPa)	Test duration (s)
170	1039	A	1	H	1	90.0	90.0	0.90	7.9	4.5	37.08
170	1039	A	1	H	2	90.0	90.0	2.40	8.2	6.0	38.34
170	1039	A	1	H	2	90.2	90.2	2.40	10.3	7.3	48.60
170	1039	A	1	H	4	90.2	90.2	5.40	13.6	7.7	64.17
170	1039	A	1	H	5	90.2	90.2	6.90	15.4	8.9	72.45
170	1039	A	1	H	6	88.8	88.8	8.39	17.9	9.6	84.42
170	1039	A	2	H	1	90.0	90.0	9.90	21.8	12.2	102.78
170	1039	A	2	H	1	126.1	126.1	10.26	19.9	10.3	93.42
170	1039	A	2	H	3	118.7	118.7	13.19	23.2	12.2	109.26
170	1039	A	2	H	4	128.4	128.4	14.78	31.1	13.4	146.07

This is a sample of the table that appears on the volume CD-ROM.

istry” section, this chapter). Two major intervals characterized by high frequency oscillation of the gamma-ray peaks are identified at 332−352 and 370−395 mbsf. These can be correlated with ash-rich zones (see “Lithostratigraphy and Structures” section, this chapter).

Logging Unit 4 (395−398 mbsf) shows very high resistivity up to 20 Ωm, bulk density up to 2.8 g/cm^3, and PEF up to 5.2. This interval corresponds to a gabbro intrusion recovered in Holes 1039B and 1039C.

Logging Unit 5 (398−404 mbsf) is characterized by relatively high resistivity between 0.9 and 1.2 Ωm and may correspond to sediments below the gabbro intrusion. The other logs did not record this deep in the hole.

REFERENCES

Berggren, W.A., Hilgen, F.J., Langereis, C.G., Kent, D.V., Obradovich, J.D., Raffi, I., Raymo, M.E., and Shackleton, N.J., 1995a. Late Neogene chronology: new perspectives in high-resolution stratigraphy. *Geol. Soc. Am. Bull.,* 107:1272−1287.

Hey, R., 1977. Tectonic evolution of the Cocos-Nazca spreading center. *Geol. Soc. Am. Bull.,* 88:1404−1420.

Kemp, A.E.S., Baldauf, J.G., and Pearce, R.B., 1995. Origins and paleoceanographic significance of laminated diatom ooze from the eastern equatorial Pacific Ocean. *In* Pisias, N.G., Mayer, L.A., Janecek, T.R., Palmer-Julson, A., and van Andel, T.H. (Eds.), *Proc. ODP, Sci. Results,* 138: College Station, TX (Ocean Drilling Program), 641−645.

Langseth, M.G., and Silver, E.A., 1996. The Nicoya convergent margin-a region of exceptionally low heat flow. *Geophys. Res. Lett.,* 23:891–894.

Li, Y.-H., and Gregory, S., 1974. Diffusion of ions in seawater and deep sea sediments. *Geochim. Cosmochim. Acta,* 38:703–714.

Lonsdale, P., and Klitgord, K.D., 1978. Structure and tectonic history of the eastern Panama Basin. *Geol. Soc. Am. Bull.,* 89:981–999.

Mayer, L., Pisias, N., Janecek, T., et al., 1992. *Proc. ODP, Init. Repts.,* 138: College Station, TX (Ocean Drilling Program).

Plank, T., and Langmuir, C.H., 1993. Tracing trace elements from sediment input to volcanic output at subduction zones. *Nature,* 362:739–743.

Shipboard Scientific Party, 1982. Site 495: Cocos Plate—Middle America Trench outer slope. *In* Aubouin, J., von Huene, R., et al., *Init. Repts. DSDP,* 67: Washington (U.S. Govt. Printing Office), 79–141.

Urmos, J., Wilkens, R.H., Bassinot, F., Lyle, M., Marsters, J.C., Mayer, L.A., and Mosher, D.C., 1993. Laboratory and well-log velocity and density measurements from the Ontong Java Plateau: new in-situ corrections to laboratory data for pelagic carbonates. *In* Berger, W.H., Kroenke, L.W., Mayer, L.A., et al., *Proc. ODP, Sci. Results,* 130: College Station, TX (Ocean Drilling Program), 607–622.

White, W.M., McBirney, A.R., and Duncan, R.A., 1993. Petrology and geochemistry of the Galápagos Islands: portrait of a pathological mantle plume. *J. Geophys. Res.,* 98:19533–19563.

Wilson, D.S., 1996. Fastest known spreading on the Miocene Cocos-Pacific plate boundary. *Geophys. Res. Lett.,* 23:3003-3006.

Wilson, M., 1989. *Igneous Petrogenesis: A Global Tectonic Approach:* London (Unwin Hyman).

Ms 170IR-103

NOTE: Core-description forms ("barrel sheets") and core photographs can be found in Section 3, beginning on page 251. Smear-slide data, thin-section descriptions, and shore-based processed log data and descriptions can be found on CD-ROM. See Table of Contents for material contained on CD-ROM.

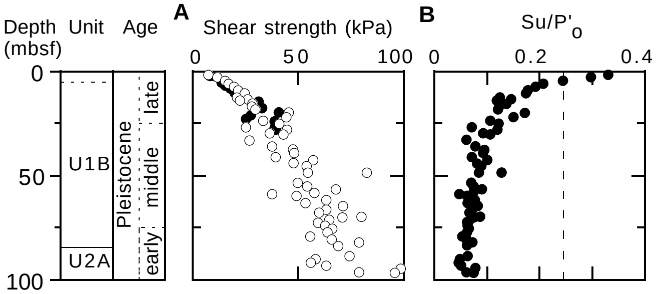

Figure 34. **A.** Undrained shear strength measured with the automated vane shear device plotted vs. depth (solid circles = Hole 1039A; open circles = Hole 1039B). **B.** Effective overburden stress plotted as a function of shear strength vs. depth. Typical normally consolidated soils have a ratio of about 0.25 (vertical dashed line), suggesting that sediment at Site 1039 is underconsolidated.

Table 23. Electrical resistivity measurement data collected from Holes 1039A and 1039B.

Leg	Site	Hole	Core	Type	Section	Top (cm)	Bottom (cm)	Depth (mbsf)	Temperature (°C)	Resistivity (Ωm)	Seawater resistivity (Ωm)	Formation factor, transverse to core
170	1039	A	1	H	6	118	118	8.68	22.4	0.319	0.201	1.586
170	1039	A	2	H	2	131	131	11.81	22.6	0.316	0.201	1.575
170	1039	A	2	H	3	129	129	13.29	23.4	0.308	0.197	1.562
170	1039	A	2	H	3	129	129	13.29	23.4	0.308	0.197	1.557
170	1039	A	2	H	4	134	134	14.84	24.0	0.315	0.195	1.615
170	1039	A	2	H	4	134	134	14.84	24.4	0.314	0.194	1.620
170	1039	A	2	H	5	145	145	16.45	24.1	0.295	0.195	1.513
170	1039	A	2	H	6	140	140	17.90	24.2	0.298	0.195	1.533
170	1039	A	2	H	7	50	50	18.50	23.4	0.308	0.197	1.557
170	1039	A	3	H	1	140	140	19.90	23.5	0.316	0.197	1.605

This is a sample of the table that appears on the volume CD-ROM.

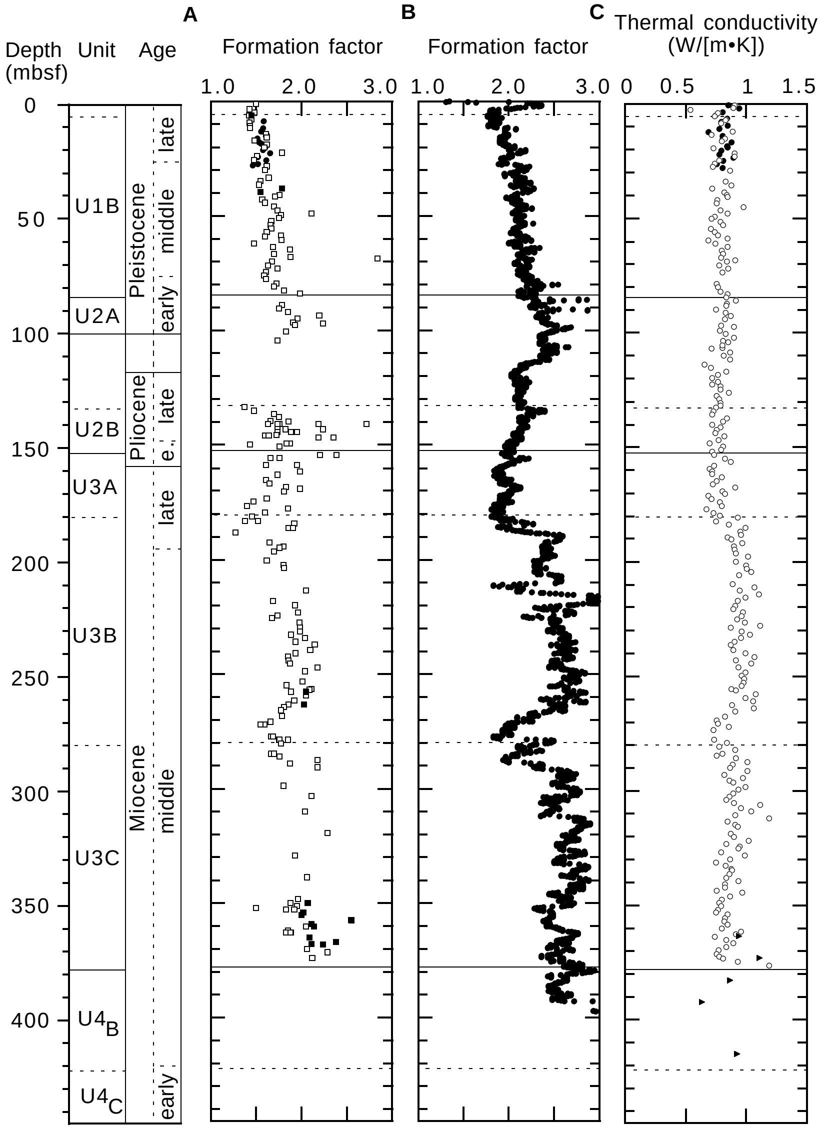

Figure 35. **A.** Formation factor (the ratio of sediment resistivity to pore-fluid resistivity) with depth for Site 1039 (solid circles = Hole 1039A transverse; open squares = Hole 1039B transverse; solid squares = Hole 1039B longitudinal) calculated from laboratory-measured values. Here the pore fluid is assumed to be normal seawater. **B.** Formation factor vs. depth calculated from downhole resistivity measurements. **C.** Thermal conductivity vs. depth for Site 1039.

Table 24. Thermal conductivity data for Site 1039.

Leg	Hole	Core	Type	Section	Top (cm)	Bottom (cm)	Depth (mbsf)	Thermal conductivity (W/[m·K])
1039	A	1	H	1	50	50	0.5	0.854
1039	A	1	H	2	50	50	2	0.943
1039	A	1	H	3	50	50	3.5	0.8039
1039	A	1	H	4	50	50	5	0.749
1039	A	1	H	5	50	50	6.5	0.841
1039	A	1	H	6	50	50	8	0.7953
1039	A	2	H	1	50	50	9.5	0.846
1039	A	2	H	2	50	50	11	0.775
1039	A	2	H	3	50	50	12.5	0.689
1039	A	2	H	4	50	50	14	0.806

This is a sample of the table that appears on the volume CD-ROM.

Table 25. Summary of in situ temperature measurements at Site 1039.

Depth (mbsf)	Hole, core	Tool	Equilibrium temp. (°C)	Comments
10 m above mudline	1039B	Adara	1.81 ± 0.1	
10 m above mudline	1039B	WSTP	1.81 ± 0.1	
10 m above mudline	1039C	WSTP	2.10 ± 0.1	
30.5	1039B-4H	Adara		Bad data
59.0	1039B-7H	Adara		Bad data
87.5	1039B-10H	Adara	3.34 ± 0.1	
132.2	1039B-16X	DVTP	3.97 ± 0.1	
180.2	1039B-21X	DVTP	4.47 ± 0.1	
228.4	1039B-26X	DVTP	4.89 ± 0.1	
276.7	1039B-31X	DVTP		Bad data
296.0	1039B-33X	DVTP	5.37 ± 0.1	
344.0	1039B-38X	DVTP	5.95 ± 0.1	

Note: Adara = APC temperature tool, WSTP = water-sampling temperature tool, DVTP = Davis-Villinger Temperature Probe.

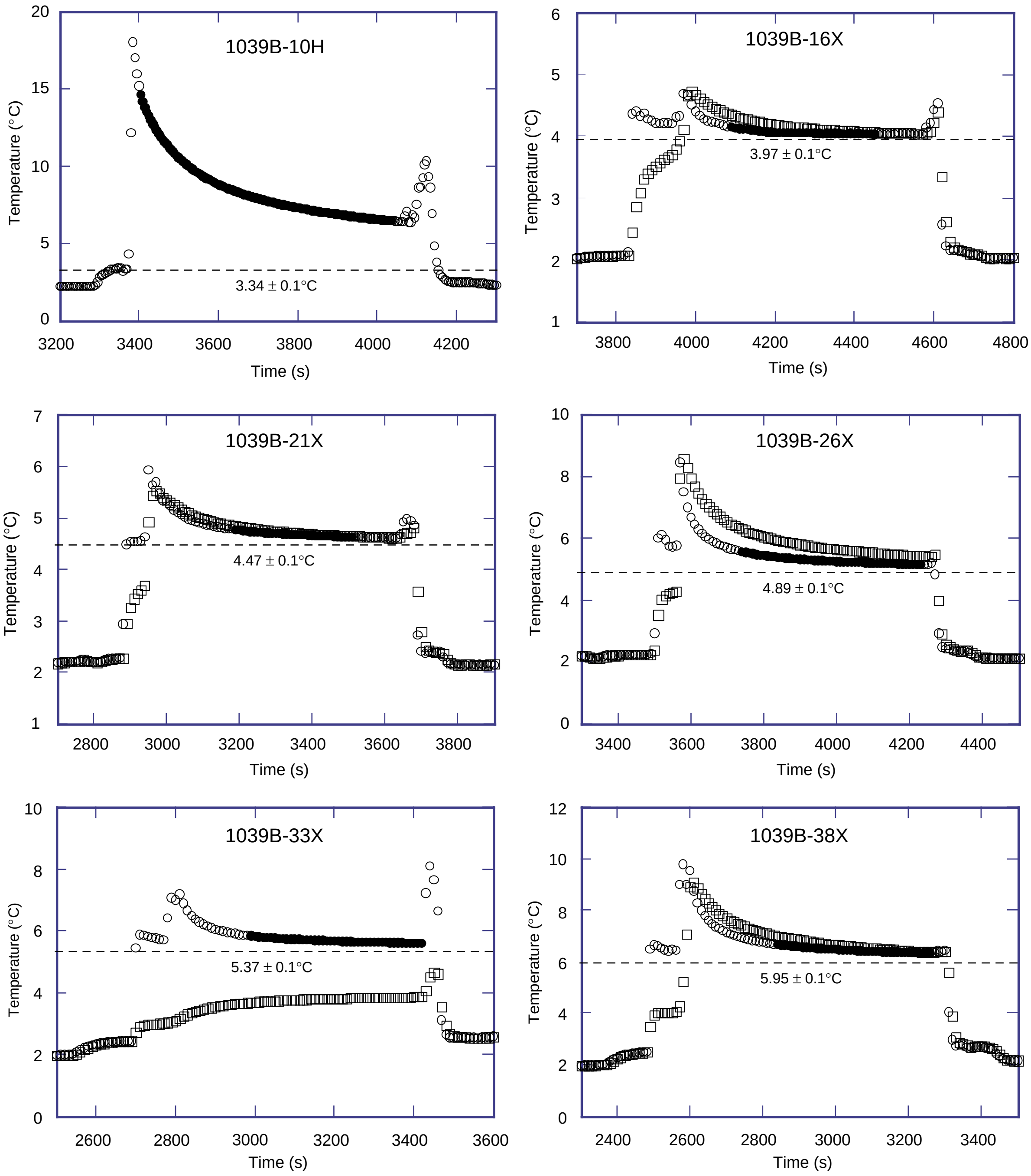

Figure 36. Temperature vs. time data from the APC temperature tool (Core 170-1039B-10H) and the DVTP deployments. The dashed line in each panel indicates the equilibrium temperature determined by fitting synthetic curves to the equilibration record. Circles and squares for the DVTP indicate temperature data from upper and lower thermistor, respectively. The portion of the equilibrium curve used for the curve fitting is indicated with filled circles.

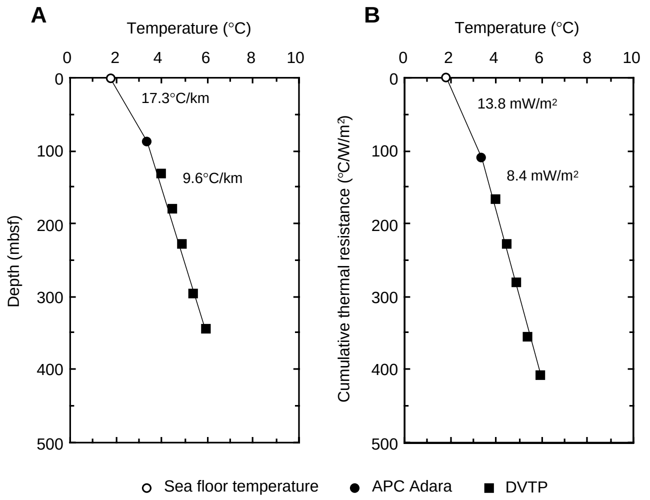

Figure 37. **A.** Temperature vs. depth at Hole 1039B. Thermal gradients are shown. **B.** Temperatures vs. cumulative thermal resistance. Mean heat flow over an interval is shown. Vertical scales are similar because thermal conductivity is near unity.

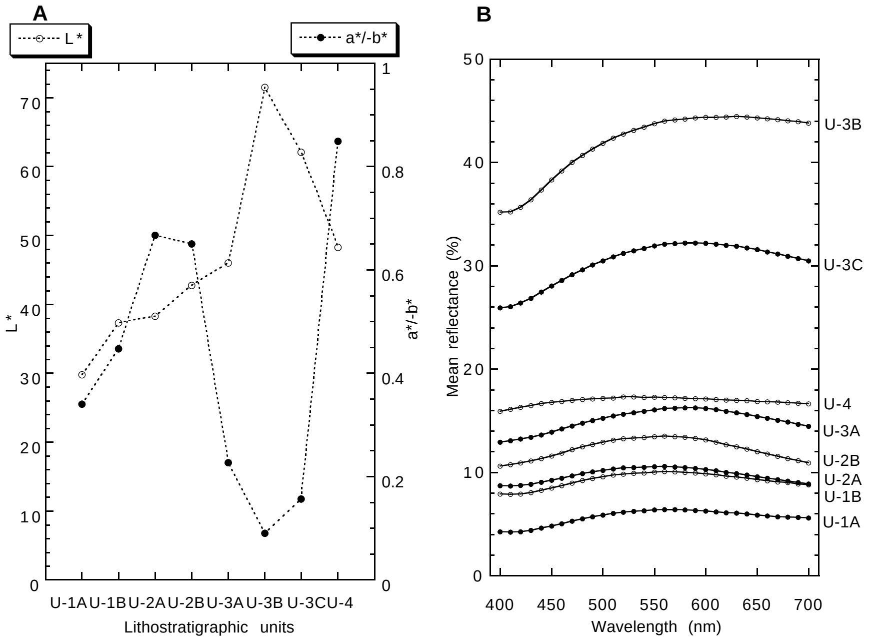

Figure 38. **A.** Mean lightness component (L*; open circles) and chromaticity ratio (a*/-b*; solid circles) for each lithostratigraphic unit drilled at Site 1039. **B.** Mean percentage of reflectance vs. wavelength for each unit cored at Site 1039.

Previous Chapter
Table of Contents
Next Chapter